Atlas of Formability

ALLVAC 718

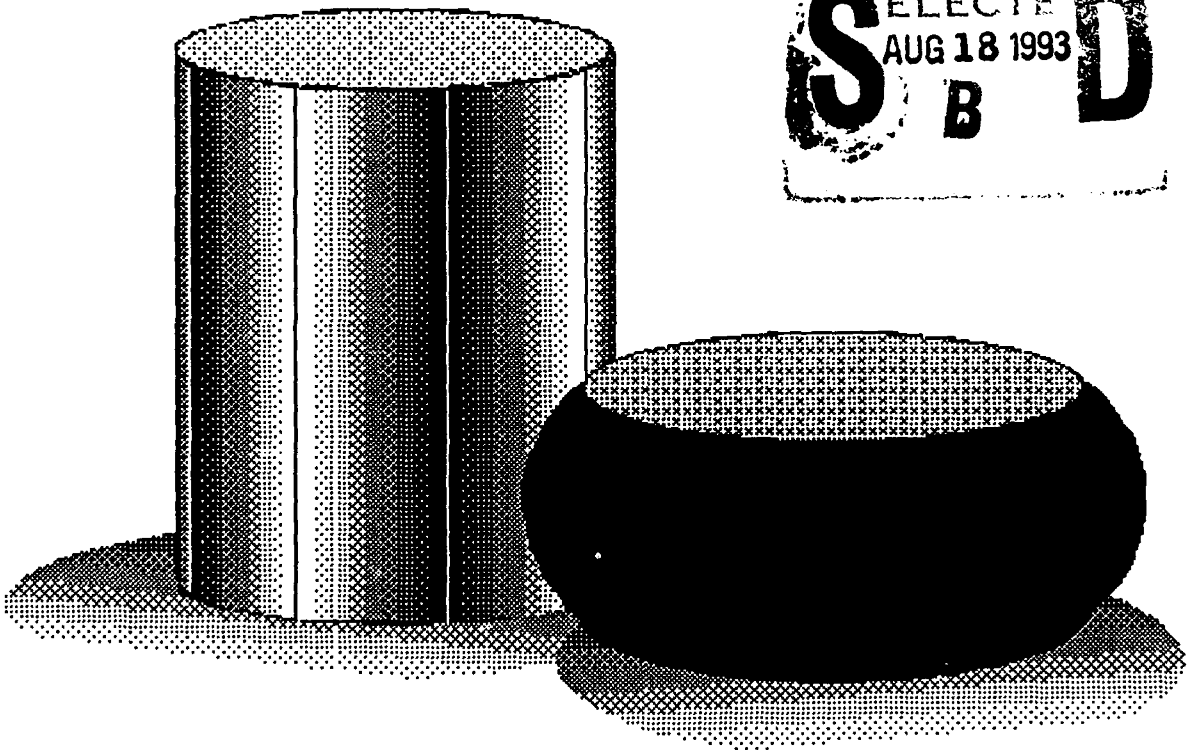

NCEMT

DISCLAIMER NOTICE

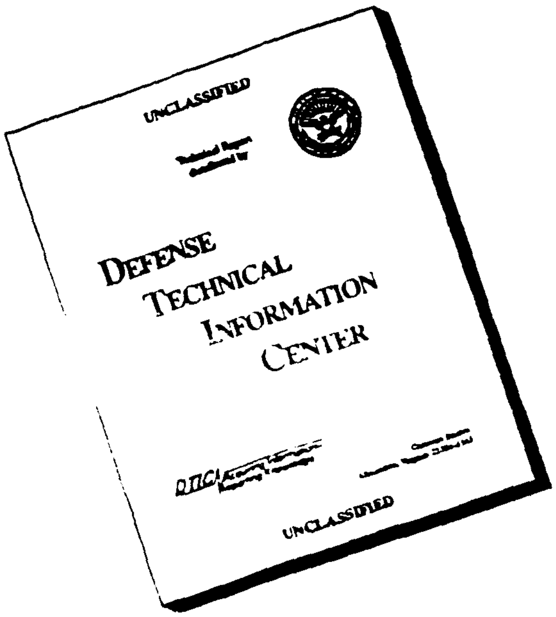

THIS DOCUMENT IS BEST QUALITY AVAILABLE. THE COPY FURNISHED TO DTIC CONTAINED A SIGNIFICANT NUMBER OF PAGES WHICH DO NOT REPRODUCE LEGIBLY.

REPORT DOCUMENTATION PAGE

Form Appr[illegible]
OMB No. 0704-0188

1. AGENCY USE ONLY (Leave blank)	2. REPORT DATE	3. REPORT TYPE AND DATES COVERED
	December 31, 1992	Final, Sept. 30, 1992 - Dec. 31, 1992

4. TITLE AND SUBTITLE
ATLAS OF FORMABILITY
ALLVAC 718

5. FUNDING NUMBERS
C-N00140-88-C-RC21

6. AUTHOR(S)
Prabir K. Chaudhury
Dan Zhao

7. PERFORMING ORGANIZATION NAME(S) AND ADDRESS(ES)
National Center for Excellence in Metalworking Technology (NCEMT)
1450 Scalp Avenue
Johnstown, PA 15904

8. PERFORMING ORGANIZATION REPORT NUMBER

9. SPONSORING/MONITORING AGENCY NAME(S) AND ADDRESS(ES)
Naval Industrial Resources Support Activity
Building 75-2, Naval Base
Philadelphia, PA 19112-5078

10. SPONSORING/MONITORING AGENCY REPORT NUMBER

11. SUPPLEMENTARY NOTES

12a. DISTRIBUTION/AVAILABILITY STATEMENT

12b. DISTRIBUTION CODE

13. ABSTRACT *(Maximum 200 words)*

In this investigation, flow behavior of Allvac 718 alloy was studied by conducting compression tests over a wide range of temperatures (850 - 1150 C) and strain rates (0.001 - 20 s^{-1}). The true stress-true strain flow curves are presented for each test condition. Constitutive relations were determined from the flow behavior, and a dynamic material modeling was performed on this alloy. Thus, the optimum processing condition in terms of temperature and strain rate was identified as 1025 C and 0.001 s^{-1} for this alloy. Microstructural changes during high temperature deformation were also characterized, and selective micrographs are presented together with corresponding flow curves. Dynamic recrystallization and grain growth occurred during high temperature deformation over the range of temperatures tested. The recrystallization is complete at 1000 C and 0.001 s^{-1}. This report supplies ample mechanical property and microstructure data on Allvac 718 alloy for engineers in the field of metalworking process design. The data presented here are also very helpful in finite element analysis of metalworking processes.

14. SUBJECT TERMS
Allvac 718, Deformation Processing, High Temperature Deformation, Processing Map, Metalworking, Microstructure

15. NUMBER OF PAGES
70

16. PRICE CODE

17. SECURITY CLASSIFICATION OF REPORT	18. SECURITY CLASSIFICATION OF THIS PAGE	19. SECURITY CLASSIFICATION OF ABSTRACT	20. LIMITATION OF ABSTRACT
Unclassified	Unclassified	Unclassified	

GENERAL INSTRUCTIONS FOR COMPLETING SF 298

The Report Documentation Page (RDP) is used in announcing and cataloging reports. It is important that this information be consistent with the rest of the report, particularly the cover and title page. Instructions for filling in each block of the form follow. It is important to ***stay within the lines*** to meet ***optical scanning requirements***.

Block 1. Agency Use Only *(Leave blank)*.

Block 2. Report Date. Full publication date including day, month, and year, if available (e.g. 1 Jan 88). Must cite at least the year.

Block 3. Type of Report and Dates Covered. State whether report is interim, final, etc. If applicable, enter inclusive report dates (e.g. 10 Jun 87 - 30 Jun 88).

Block 4. Title and Subtitle. A title is taken from the part of the report that provides the most meaningful and complete information. When a report is prepared in more than one volume, repeat the primary title, add volume number, and include subtitle for the specific volume. On classified documents enter the title classification in parentheses.

Block 5. Funding Numbers. To include contract and grant numbers; may include program element number(s), project number(s), task number(s), and work unit number(s). Use the following labels:

C	- Contract	PR	- Project
G	- Grant	TA	- Task
PE	- Program Element	WU	- Work Unit Accession No.

Block 6. Author(s). Name(s) of person(s) responsible for writing the report, performing the research, or credited with the content of the report. If editor or compiler, this should follow the name(s).

Block 7. Performing Organization Name(s) and Address(es). Self-explanatory.

Block 8. Performing Organization Report Number. Enter the unique alphanumeric report number(s) assigned by the organization performing the report.

Block 9. Sponsoring/Monitoring Agency Name(s) and Address(es). Self-explanatory.

Block 10. Sponsoring/Monitoring Agency Report Number. *(If known)*

Block 11. Supplementary Notes. Enter information not included elsewhere such as: Prepared in cooperation with...; Trans. of...; To be published in.... When a report is revised, include a statement whether the new report supersedes or supplements the older report.

Block 12a. Distribution/Availability Statement. Denotes public availability or limitations. Cite any availability to the public. Enter additional limitations or special markings in all capitals (e.g. NOFORN, REL, ITAR).

- **DOD** - See DoDD 5230.24, "Distribution Statements on Technical Documents."
- **DOE** - See authorities.
- **NASA** - See Handbook NHB 2200.2.
- **NTIS** - Leave blank.

Block 12b. Distribution Code.

- **DOD** - Leave blank.
- **DOE** - Enter DOE distribution categories from the Standard Distribution for Unclassified Scientific and Technical Reports.
- **NASA** - Leave blank.
- **NTIS** - Leave blank.

Block 13. Abstract. Include a brief *(Maximum 200 words)* factual summary of the most significant information contained in the report.

Block 14. Subject Terms. Keywords or phrases identifying major subjects in the report.

Block 15. Number of Pages. Enter the total number of pages.

Block 16. Price Code. Enter appropriate price code *(NTIS only)*.

Blocks 17. - 19. Security Classifications. Self-explanatory. Enter U.S. Security Classification in accordance with U.S. Security Regulations (i.e., UNCLASSIFIED). If form contains classified information, stamp classification on the top and bottom of the page.

Block 20. Limitation of Abstract. This block must be completed to assign a limitation to the abstract. Enter either UL (unlimited) or SAR (same as report). An entry in this block is necessary if the abstract is to be limited. If blank, the abstract is assumed to be unlimited.

ATLAS OF FORMABILITY

ALLVAC 718

by

Prabir K. Chaudhury and Dan Zhao

National Center for Excellence in Metalworking Technology
1450 Scalp Avenue
Johnstown, PA 15904

for

Naval Industrial Resource Support Activity
Building 75-2, Naval Base
Philadelphia, PA 19112-5078

December 31, 1992

TABLE OF CONTENTS

LIST OF TABLE

Allvac 718

Introduction

Allvac 718 is a precipitation-hardenable nickel-chromium alloy. This material has been widely used for aerospace applications due to its excellent creep-rupture strength at temperatures up to 700 C. This alloy also combines a very good corrosion resistance and high strength with an excellent weldability. The understanding of mechanical and microstructural behavior during high temperature deformation is very important for the forming processes of this alloy. In this investigation, flow behavior of Allvac 718 was studied by conducting compression tests at various temperatures and strain rates. Constitutive relations were determined from the flow behavior and then, a dynamic material modeling for this alloy was performed. Thus, the optimum processing condition in terms of temperature and strain rate were determined. Microstructural changes during high temperature deformation were also characterized to aid process design engineers to select processing conditions in terms of resulting microstructure.

Experimental Procedure

The material used in this investigation was commercially available Allvac 718, solution treated at 1024 C for one hour, water quenched, then aged at 788 C for six and half hours and air cooled. The typical microstructure of the as-received materials consists of equiaxed twinned grains with an average size of 54 μm (5.2 ASTM) shown in Figure 1. The chemical composition is as follows (wt%) with Fe as balance:

C	S	Mn	Si	Cr	Mo	Co	Ti	Al	B	Cu	Ni	P	Cb	Ta
.019	.0004	.06	.07	17.65	2.90	.25	.94	.52	.004	.05	51.67	.004	5.07	.01

Cylindrical compression test specimens with a diameter of 12.7 mm and a height of 15.9 mm were machined from the bars. Isothermal compression tests were conducted on an MTS testing machine in a vacuum chamber. The test matrix was as follows:

Temperature, C (F): 850 (1562), 900 (1652), 950 (1742), 1000 (1832), 1050 (1922), 1100 (2012), and 1150 (2102);
Strain rate, s^{-1}: 0.001, 0.01, 0.05, 0.1, 0.5, 1, 5 and 20.

Load and stroke data from the tests were acquired by a computer and later converted to true stress-true strain curves. Immediately after the compression test, the specimens were quenched with forced helium gas in order to retain the deformed microstructure. Longitudinal sections of the specimens were examined by optical microscopy. The photomicrographs presented were taken from the center of the longitudinal section of the specimens.

Results

Table 1 shows a list of the figures, test conditions and the observed microstructures. The true stress-true strain flow curves with selective corresponding deformed microstructure are shown in Figure 2 to Figure 57. True stress versus strain rate was plotted in log-log scale in Figure 58 at a true strain of 0.5. The slope of the plot gives the strain rate sensitivity m, which is not constant over the range of strain rate tested. Log stress vs. 1/T at the same true strain is shown in Figure 59. A processing map at this strain was developed and is shown in Figure 60. The optimum processing condition from the map can be obtained by selecting the temperature and strain rate combination which provides the maximum efficiency in the stable region. This condition is approximately 1025 C and 10^{-3} s^{-1} for this material.

Table 1. List of figures, testing conditions and microstructural observations for Allvac 718-OP

Figure No	Temperature C (F)	Strain Rate s^{-1}	Microstructure Optical Microscopy	Page No
1	As received		Equiaxed twinned grains with a fairly uniform grain size of 54 μm (5.2 ASTM). There is also presence of (less than 1 %) precipitates with size ranging from 1-15 μm.	5
2	850 (1562)	0.001	Elongated grains present in the microstructure show mechanical working of the material.	6
3	850 (1562)	0.01		7
4	850 (1562)	0.05	Elongated grains as above. The deformed grains show slip lines and grain boundary serrations, a precursor to necklacing that is attributed to the onset of DRX.	8
5	850 (1562)	0.1	Elongated grains as above showing an extensive amount of slip lines. The microstructure shows necklacing and some (~5%) very fine recrystallized grains (~0.5μm)	9
6	850 (1562)	0.5		10
7	850 (1562)	1	Elongated grains as above. There is more (~15%) recrystallization at the grain and twin boundaries.	11
8	850 (1562)	5	Excessively deformed grains which show serrations at the grain boundaries and ~15% recrystallization.	12
9	850 (1562)	20	Excessively deformed grains as above. The microstructure has a larger amount (~40%) of recrystallization. Possibly due to high adiabatic heating induced by the higher strain rate.	13
10	900 (1652)	0.001	Elongated grains as in Figure 2. The deformed grains have serrated boundaries and show necklacing (~3-5% recrystallization). The strained grains have a substructure (low angle grain boundaries)..	14
11	900 (1652)	0.01	Same as above with higher amount of recrystallization.	15
12	900 (1652)	0.05		16
13	900 (1652)	0.1	Excessively deformed grains showing some (~15%) recrystallization at the grain boundaries (with very small grains ~0.5μm).	17
14	900 (1652)	0.5		18
15	900 (1652)	1	Excessively deformed grains showing some necklacing (~ 10%) concentrated at slip lines with recrystallized small grains (~ 2 to 5 μm in size).	19
16	900 (1652)	5		20
17	900 (1652)	20	Excessively deformed grains with ~60% recrystallization (small grains are ~0.5-2μm in size).	21
18	950 (1742)	0.001	~5% elongated grains and ~95% recrystallized equiaxed grains.	22
19	950 (1742)	0.01		23
20	950 (1742)	0.05	~30% elongated grains showing twins and substructure. ~70% recrystallized equiaxed grains with a fairly uniform size (~5μm).	24
21	950 (1742)	0.1	~65% recrystallized equiaxed grains with a uniform size (~4 μm).	25
22	950 (1742)	0.5	~40% of the microstructure contains elongated grains. ~60% recrystallized equiaxed grains have an average grain size of 3.5μm.	26

23	950 (1742)	1	~65% elongated grains showing substructure formation. 35% recrystallized grains with a non uniform size grain size (average size ~3μm).	27
24	950 (1742)	5	~40% elongated grains showing slip lines and ~60% recrystallized equiaxed grains with a size of ~3μm.	28
25	950 (1742)	20	~20% elongated grains, a majority of the grains have a substructure. The new recrystallized equiaxed grains (80%) have an average size of 2.5μm.	29
26	1000 (1882)	0.001	100% recrystallized equiaxed grains with non-uniform size (duplex). The larger grains (40-45%) have a grain size of ~13μm and some of them have a substructure. The smaller grains have a size of 4.5μm.	30
27	1000 (1882)	0.01	100% recrystallized equiaxed grains with a non-uniform grain size (average size ~14μm).	31
28	1000 (1882)	0.05		32
29	1000 (1882)	0.1	~90% recrystallized equiaxed grains with a duplex size. The average grain size is ~12μm.(~25% larger grains). The elongated grains (~10%) show a substructure.	33
30	1000 (1882)	0.5		34
31	1000 (1882)	1	~90% recrystallized equiaxed grains with a non-uniform size (average ~8 μm). The larger grains have an average size of 15μm.	35
32	1000 (1882)	5		36
33	1000 (1882)	20	~85% recrystallized equiaxed grains with a non-uniform size (average ~7 μm). The deformed grains have an aspect ratio of 3.2 and some show a substructure.	37
34	1050 (1922)	0.001	100% recrystallized equiaxed grains with a non-uniform size (average ~31μm). There are some (~8%) new deformed grains showing a substructure. Note that this temperature is slightly above the δ solvus.	38
35	1050 (1922)	0.01		39
36	1050 (1922)	0.05	100% recrystallized equiaxed grains with an average size of ~20μm. There are ~3 - 5% new deformed grains.	40
37	1050 (1922)	0.1		41
38	1050 (1922)	0.5	100% recrystallized equiaxed grains with an average grain size of 18 μm. A few (<2%) new deformed grains are present.	42
39	1050 (1922)	1	100% recrystallized grains with an average size of 15 μm. The amount of new deformed grains is less than 1%.	43
40	1050 (1922)	5	100% recrystallized equiaxed grains with an average size of 12μm. New deformed grains were not observed.	44
41	1050 (1922)	20	Same as above, but the grain size is approximately 12 μm.	45
42	1100 (1212)	0.001	100% recrystallized grains with a fairly regular size (~63.8 μm). Approximately 5% of the new equiaxed grains show the presence of a substructure.	46
43	1100 (1212)	0.01	100% recrystallized equiaxed grains with an average grain size of 39.5 μm.	47
44	1100 (1212)	0.05		48
45	1100 (1212)	0.1	100% recrystallized equiaxed grains with a non-uniform size (average of 32 μm).	49
46	1100 (1212)	0.5		50

47	1100 (1212)	1	100% recrystallized equiaxed grains with a non-uniform size (average of 30 μm).	51
48	1100 (1212)	5		52
49	1100 (1212)	20	100% recrystallized equiaxed grains with a non-uniform size (average of 25 μm).	53
50	1150 (2102)	0.001	100% recrystallized equiaxed grains with a non-uniform size (average ~136 μm). The grain size range was 30-350 μm. Some of the new grains (~10%) show the presence of a substructure.	54
51	1150 (2102)	0.01		55
52	1150 (2102)	0.05	100% recrystallized equiaxed grains with a non-uniform size (average ~65 μm).	56
53	1150 (2102)	0.1	Same as above, but the grain size is ~58 μm.	57
54	1150 (2102)	0.5		58
55	1150 (2102)	1	Same as above, but the average grain size is ~50 μm.	59
56	1150 (2102)	5	Same as above, but the average grain size is ~48 μm.	60
57	1150 (2102)	20	Same as above.	61

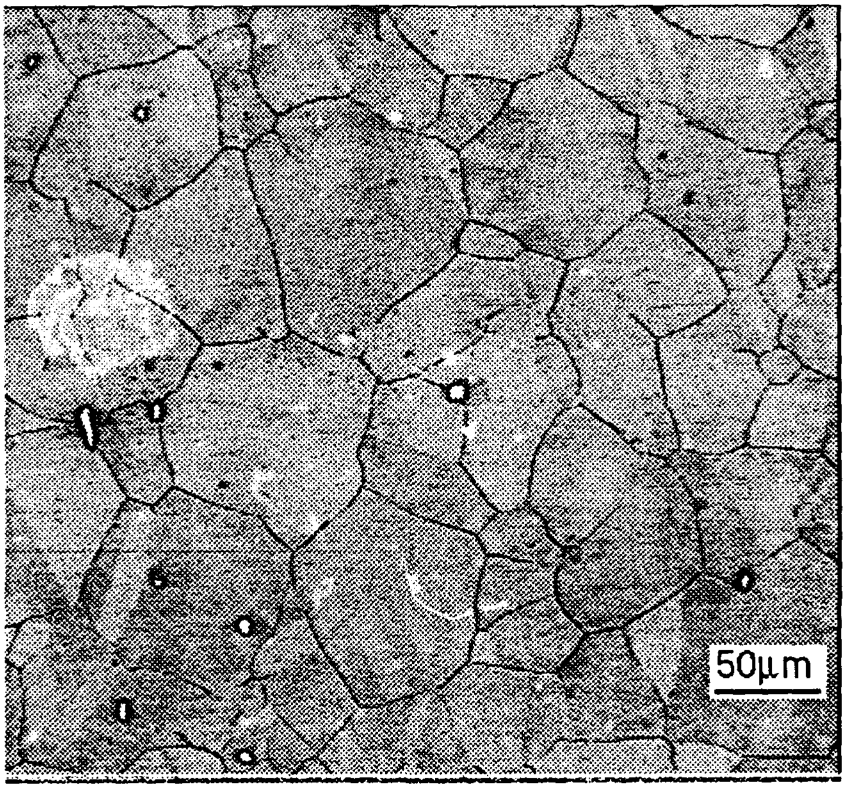

Figure 1. As-received microstructure of Allvac 718-OP.

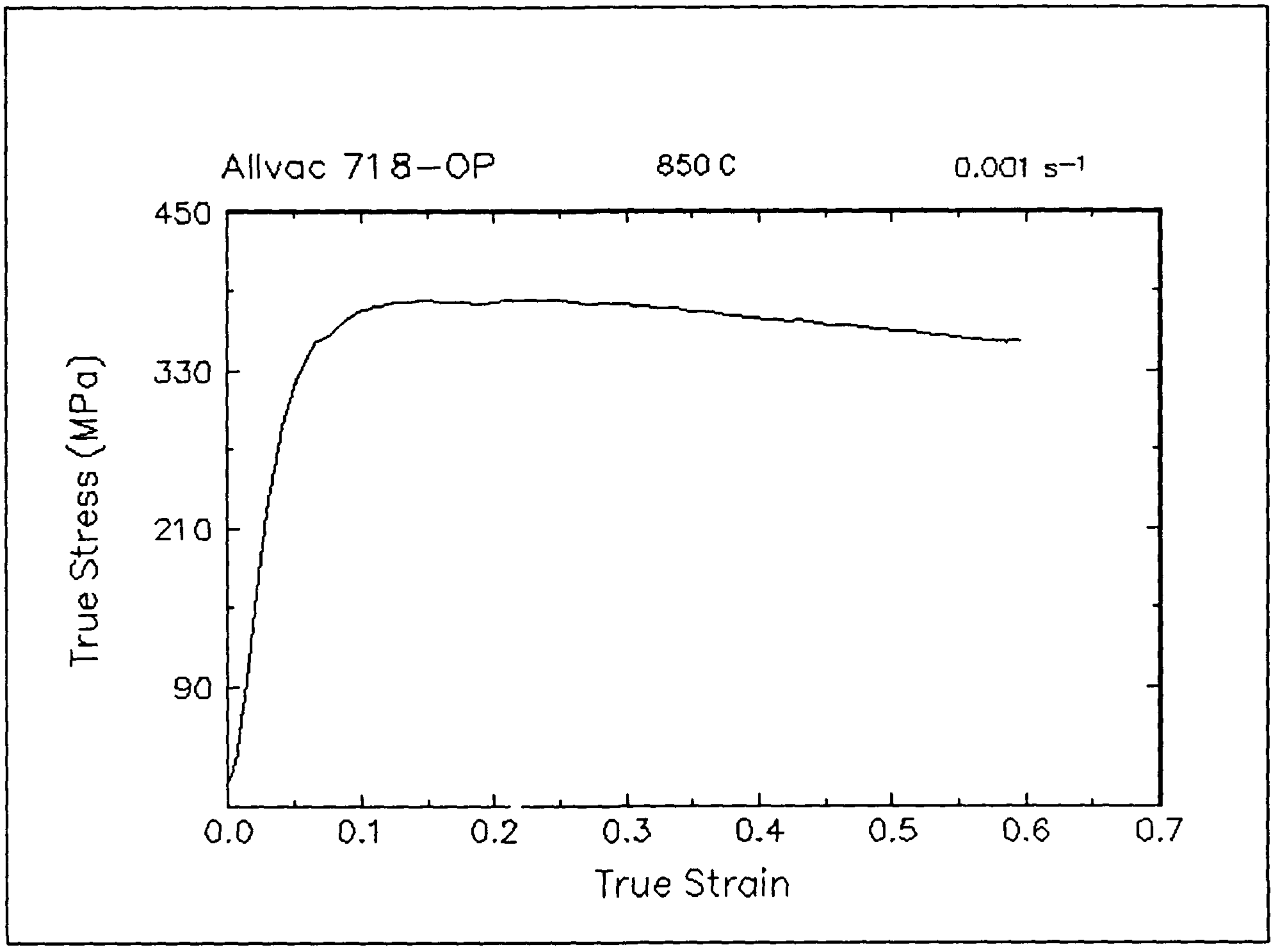

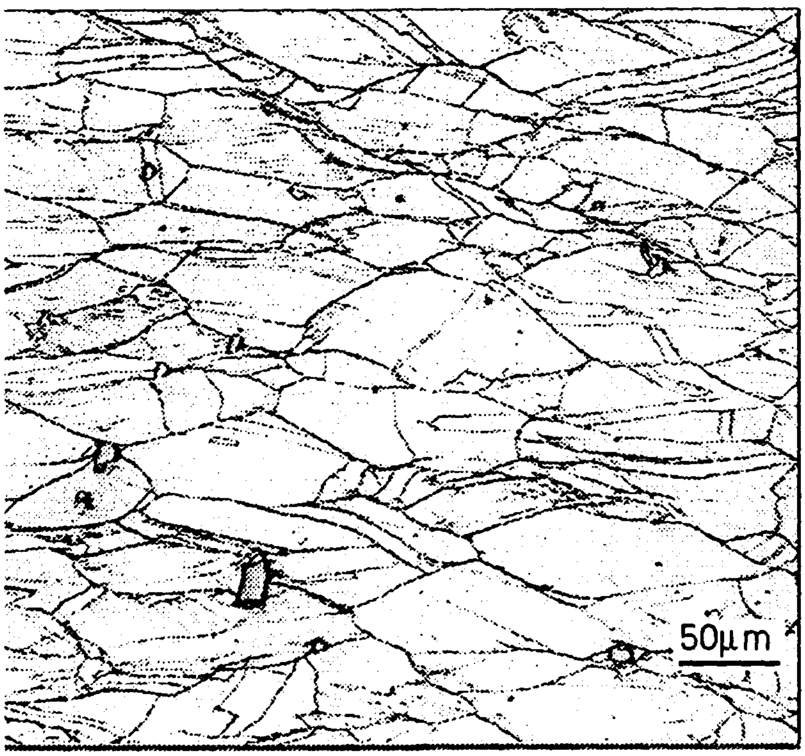

Figure 2. True stress-true strain curve and an optical micrograph from the center of the compressed sample cut through the compression axis, 850 C and 0.001 s^{-1}.

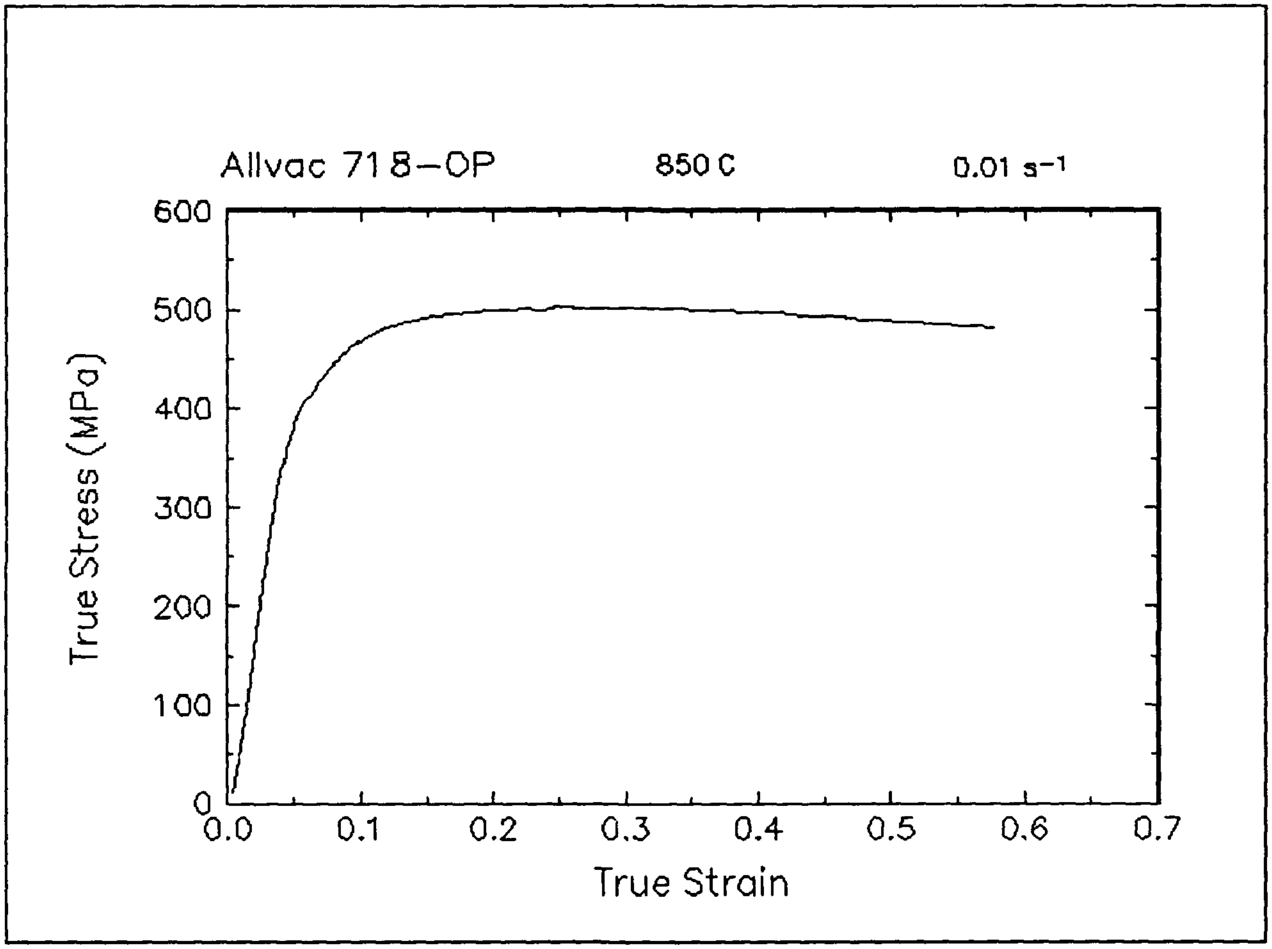

Figure 3. True stress-true strain curve, 850 C and 0.01 s^{-1}.

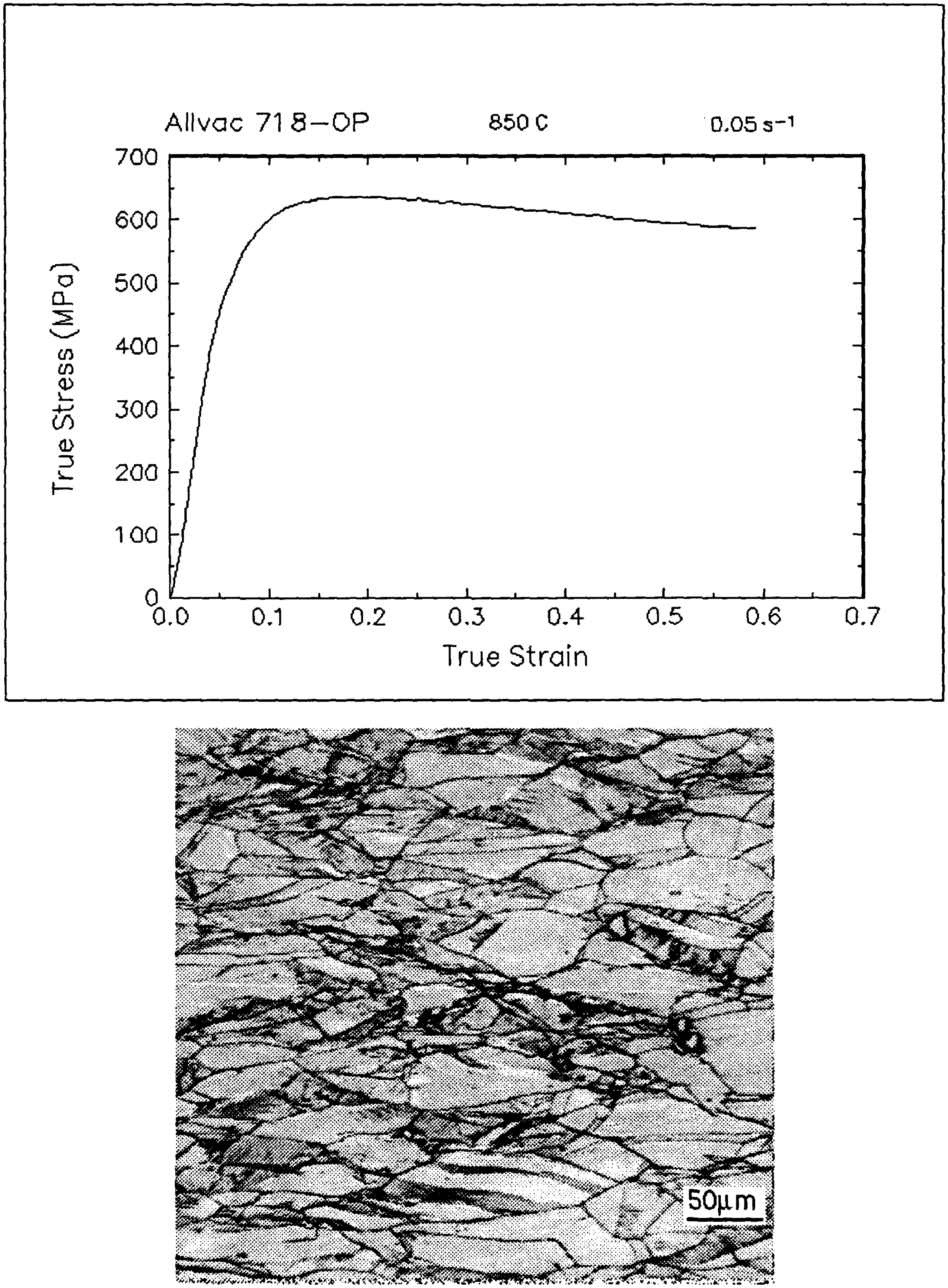

Figure 4. True stress-true strain curve and an optical micrograph from the center of the compressed sample cut through the compression axis, 850 C and 0.05 s^{-1}.

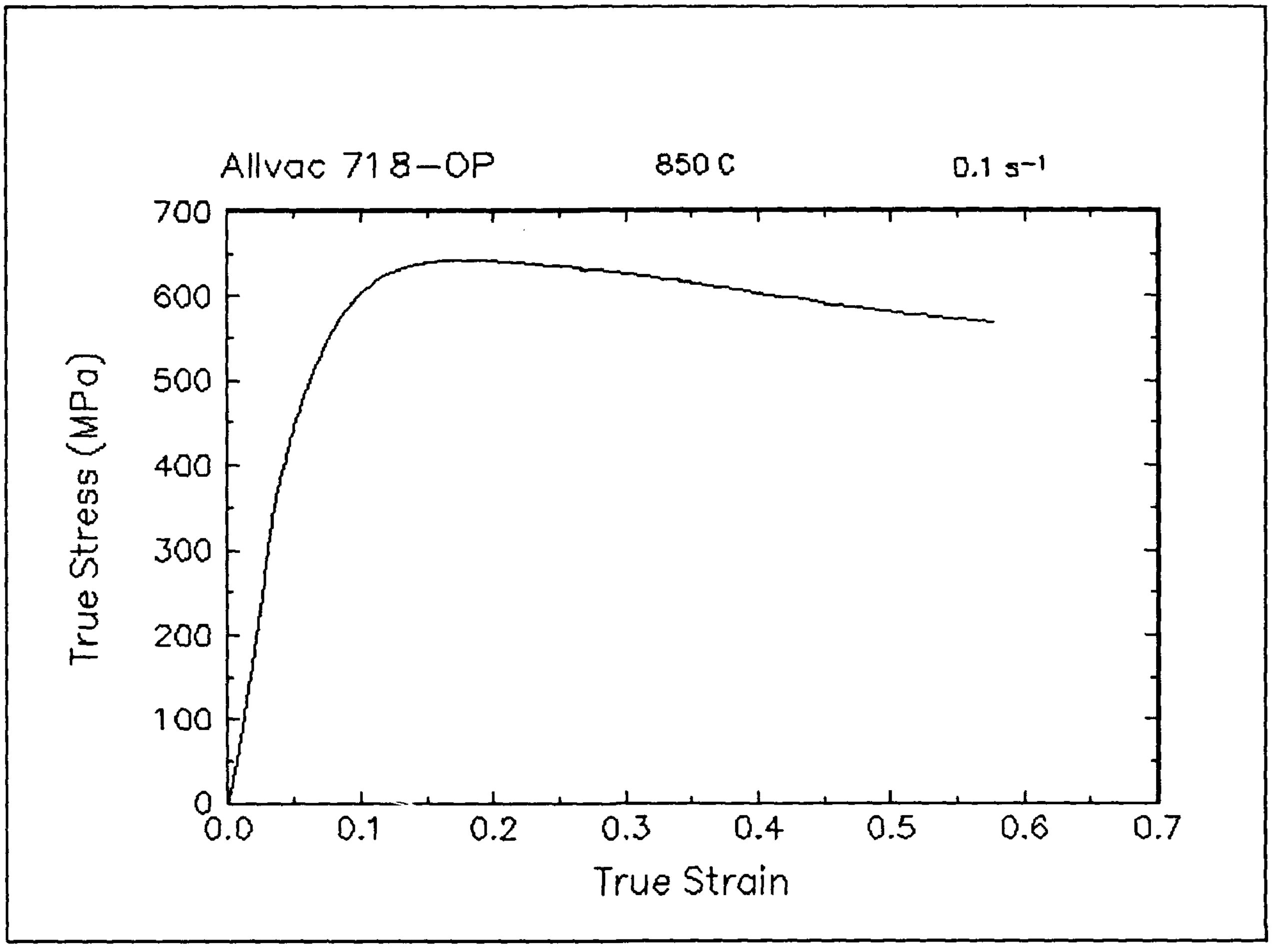

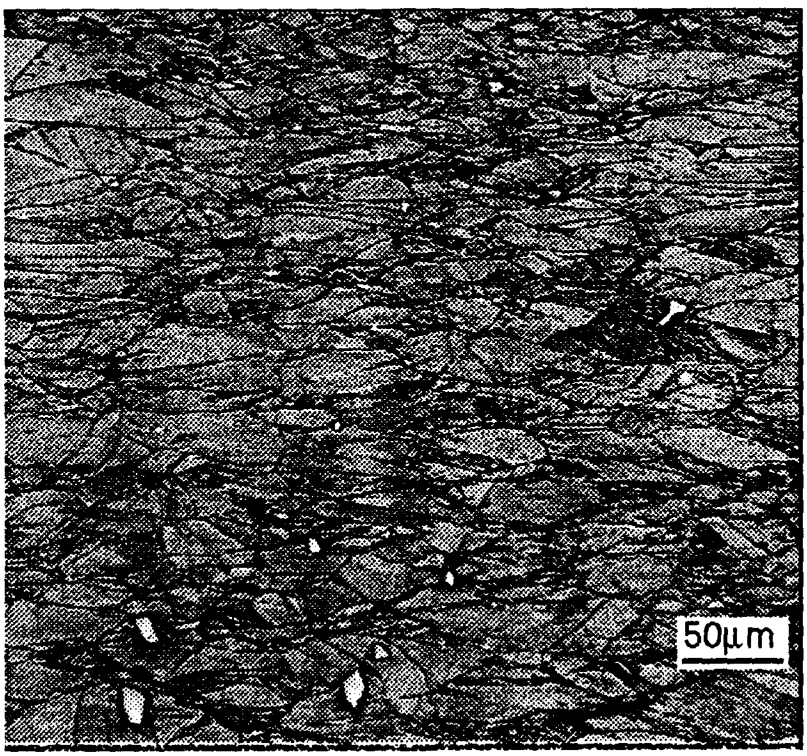

Figure 5. True stress-true strain curve and an optical micrograph from the center of the compressed sample cut through the compression axis, 850 C and 0.1 s^{-1}.

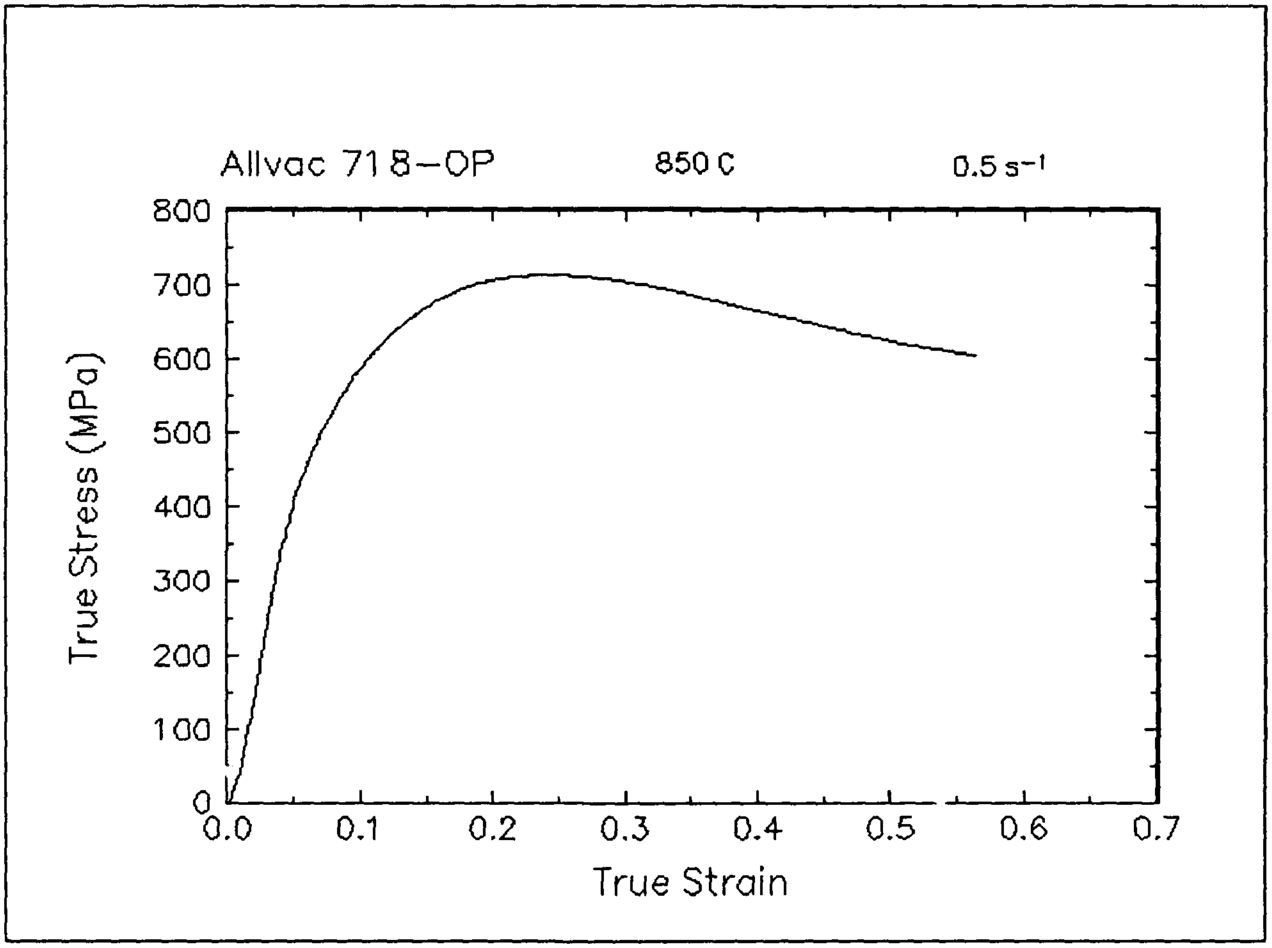

Figure 6. True stress-true strain curve, 850 C and 0.5 s^{-1}.

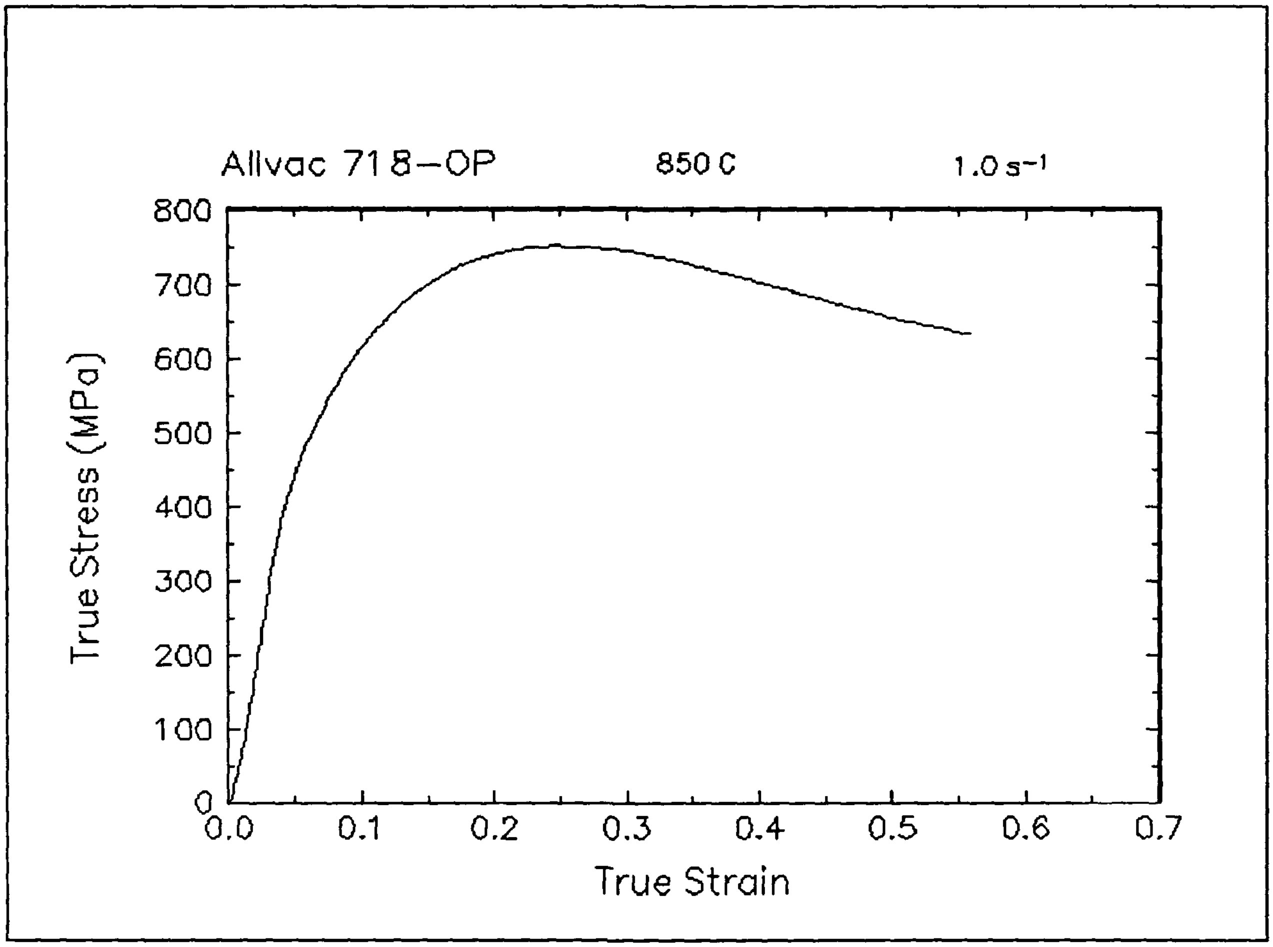

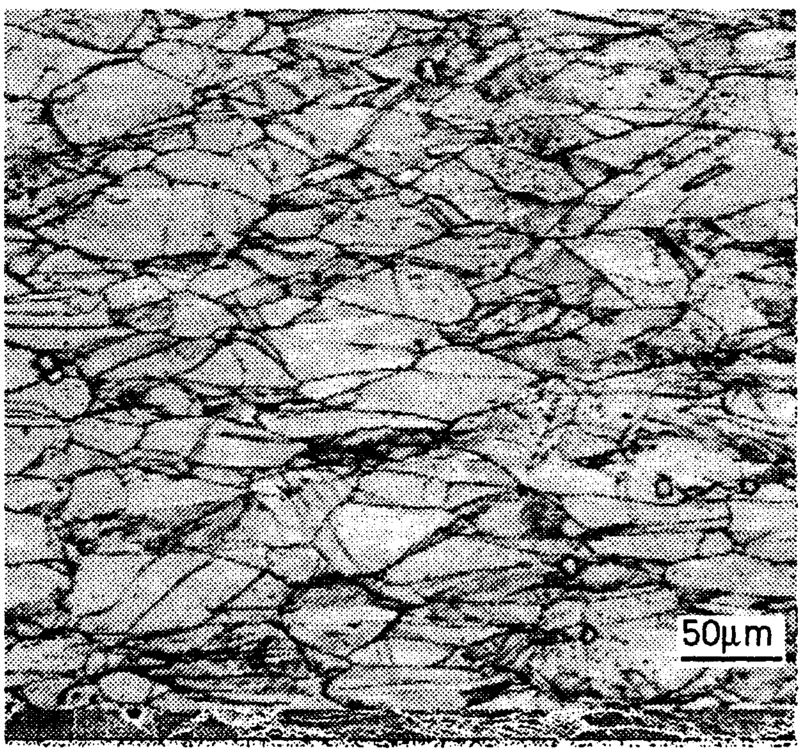

Figure 7. True stress-true strain curve and an optical micrograph from the center of the compressed sample cut through the compression axis, 850 C and 1 s^{-1}.

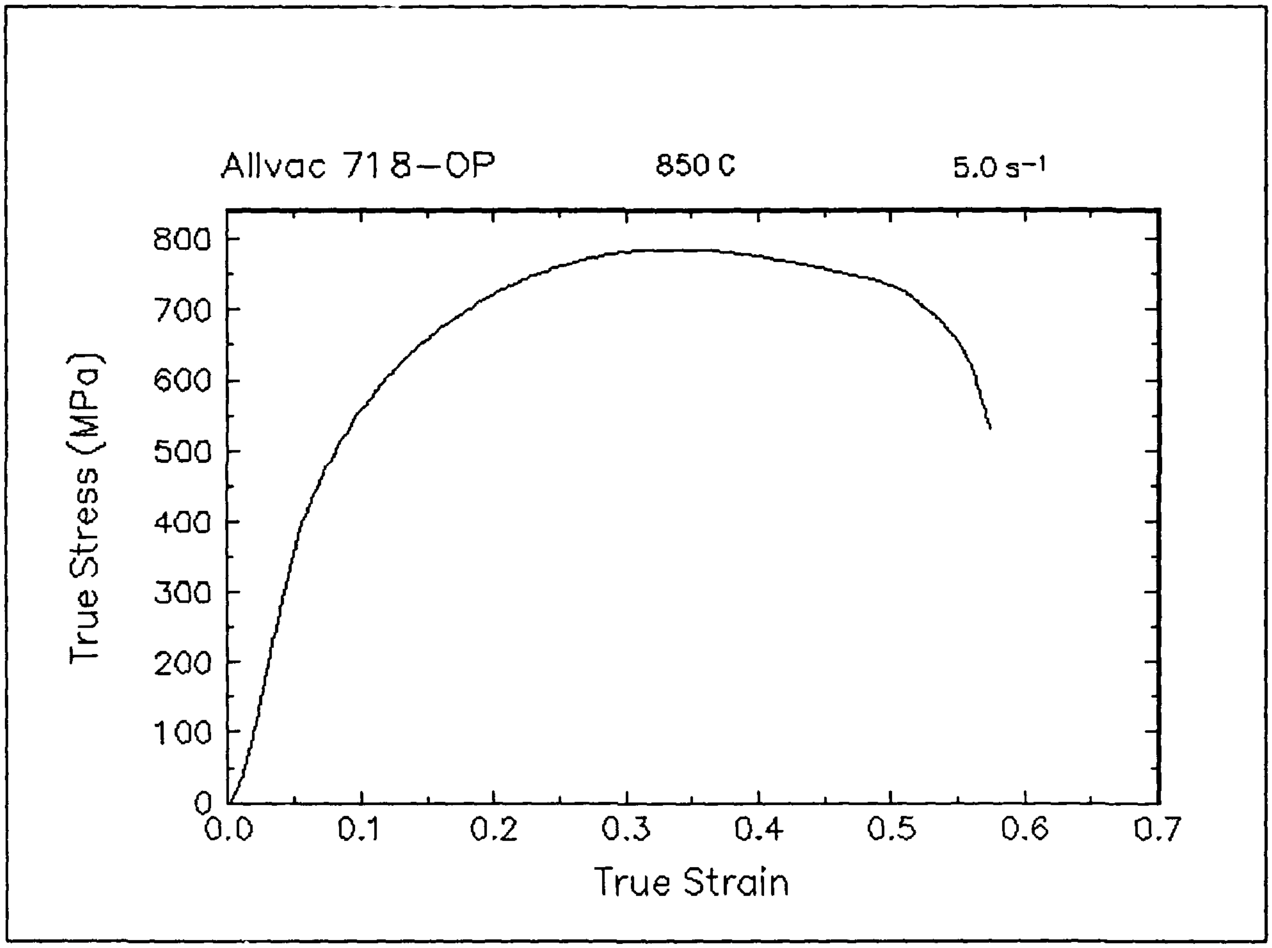

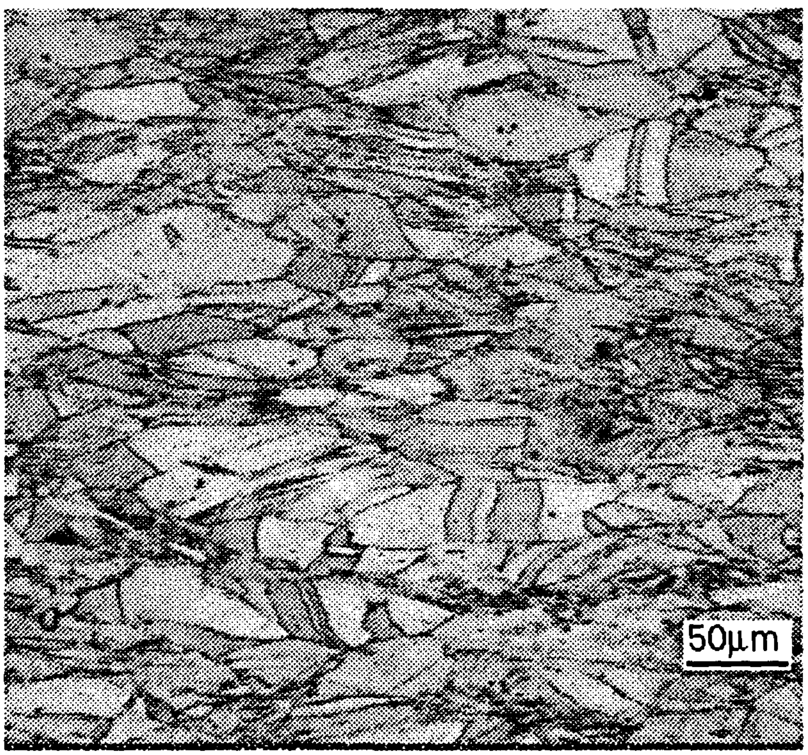

Figure 8. True stress-true strain curve and an optical micrograph from the center of the compressed sample cut through the compression axis, 850 C and 5 s^{-1}.

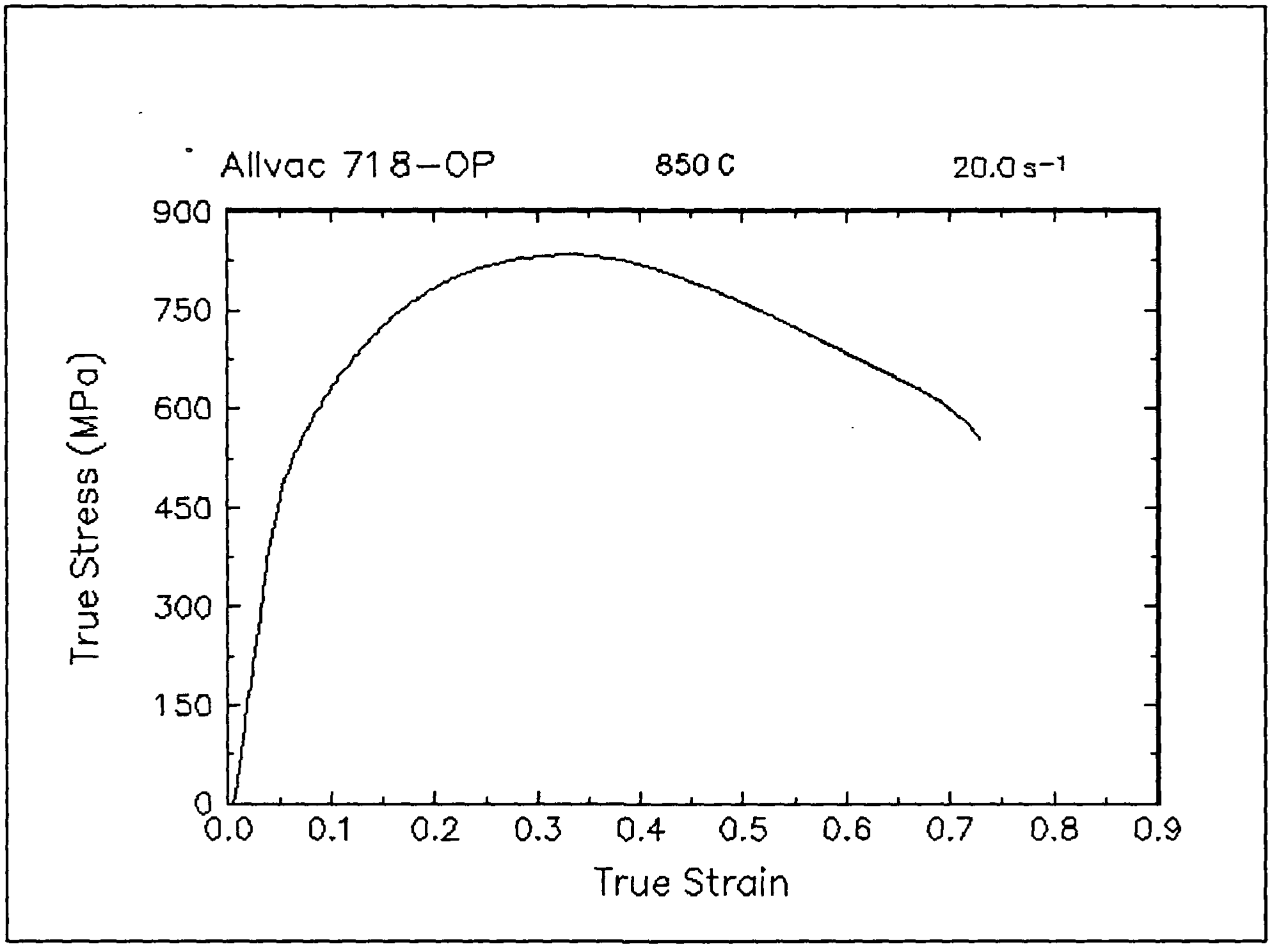

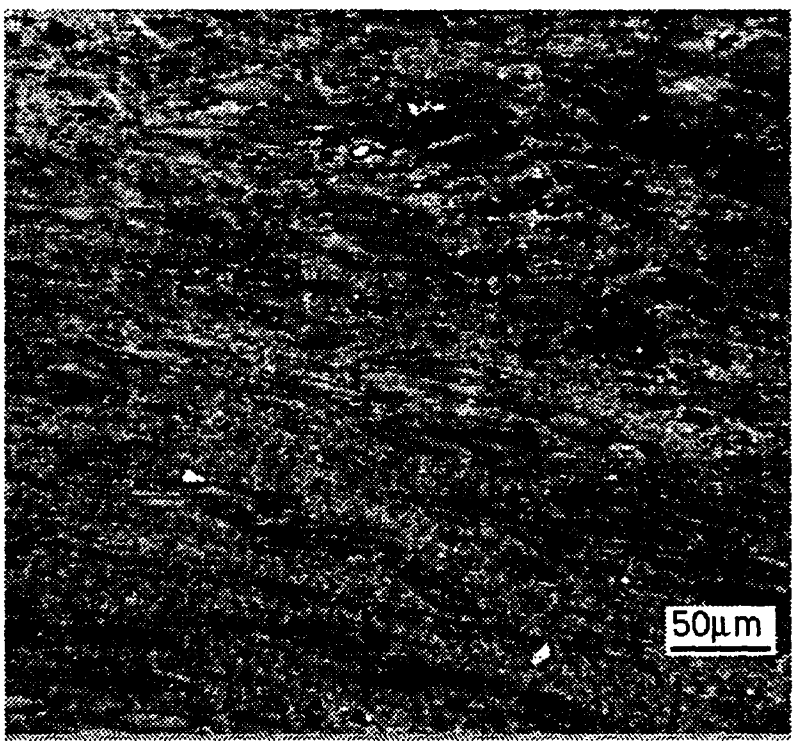

Figure 9. True stress-true strain curve and an optical micrograph from the center of the compressed sample cut through the compression axis, 850 C and 20 s^{-1}.

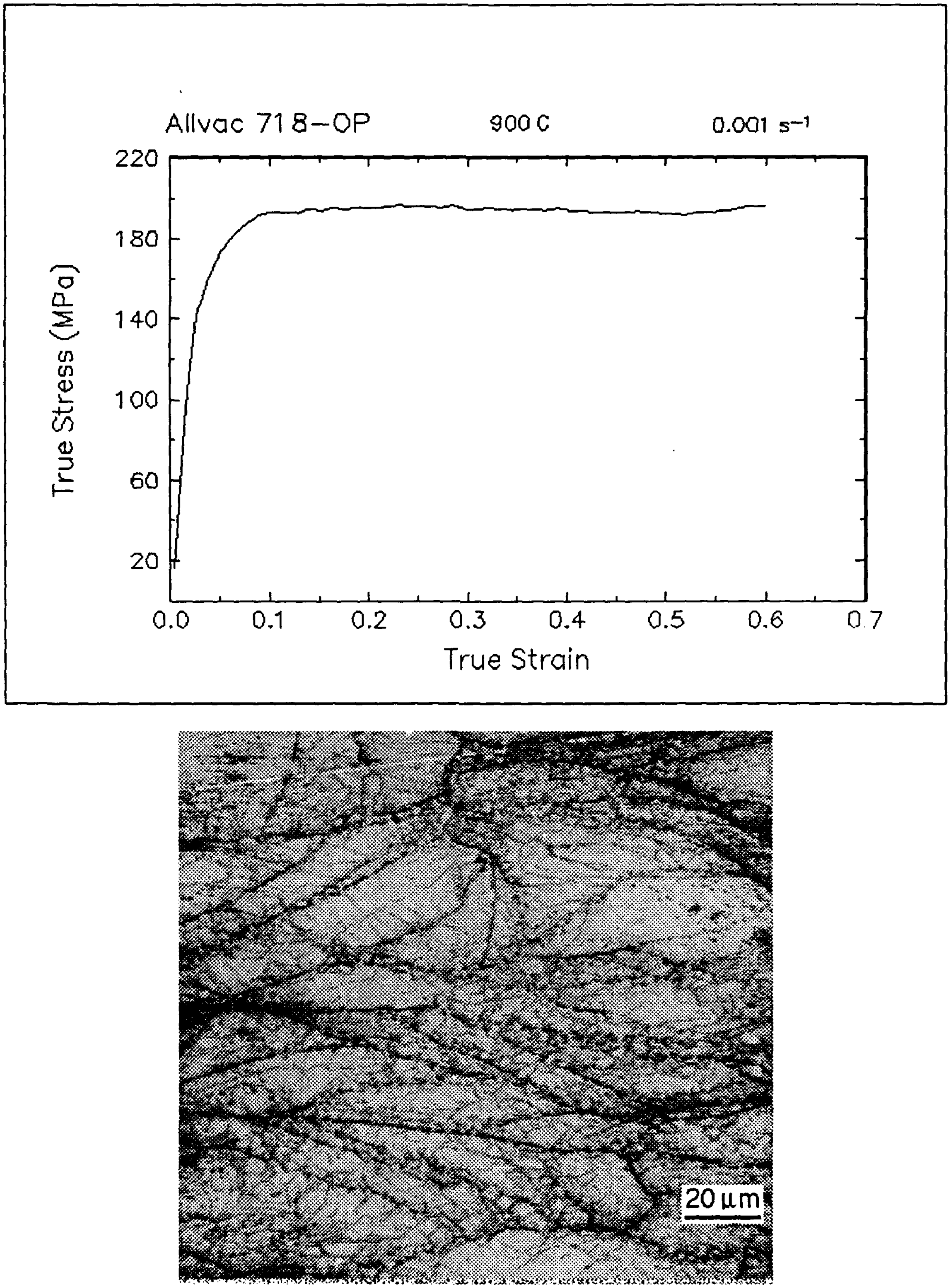

Figure 10. True stress-true strain curve and an optical micrograph from the center of the compressed sample cut through the compression axis, 900 C and 0.001 s^{-1}.

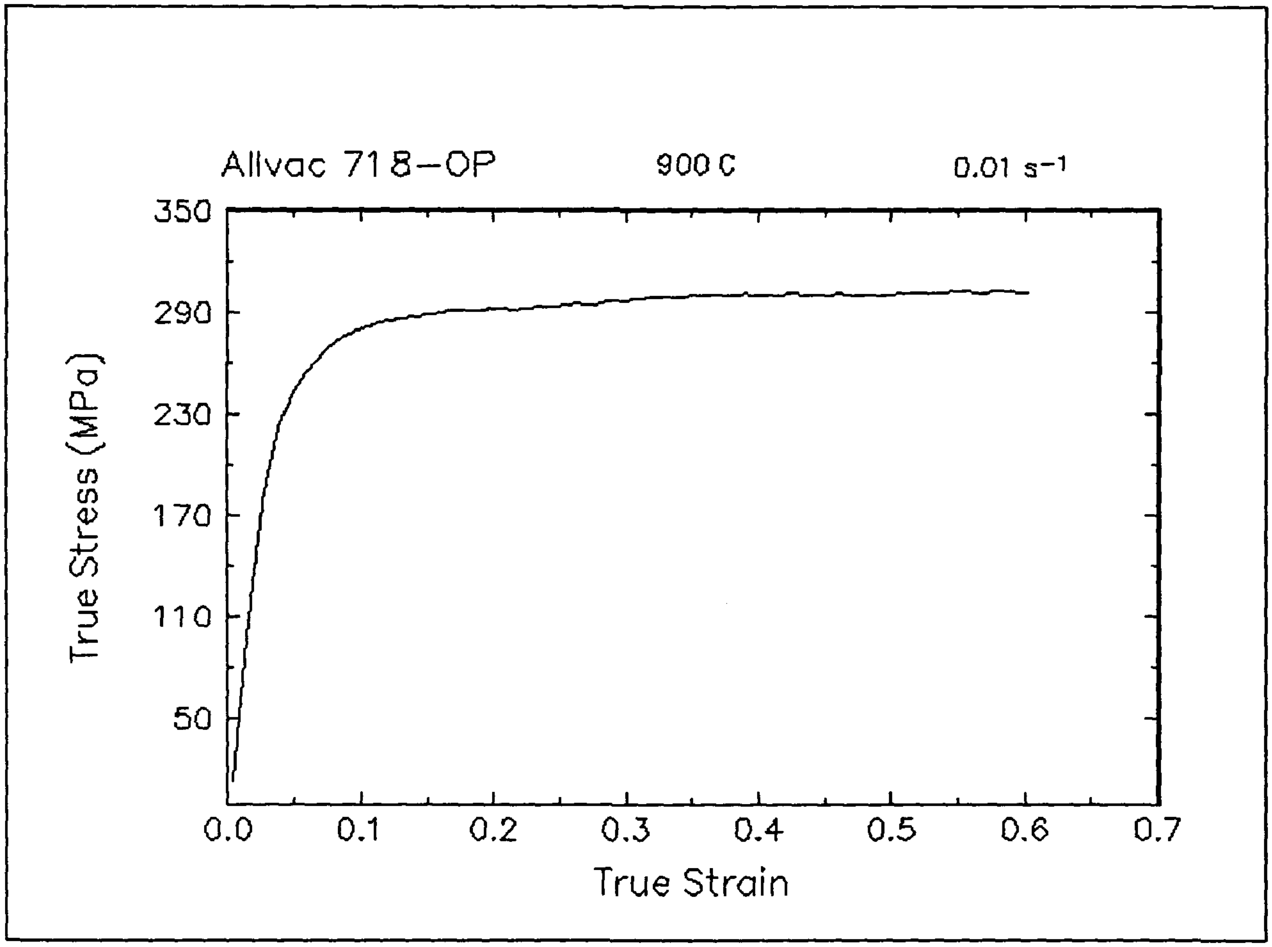

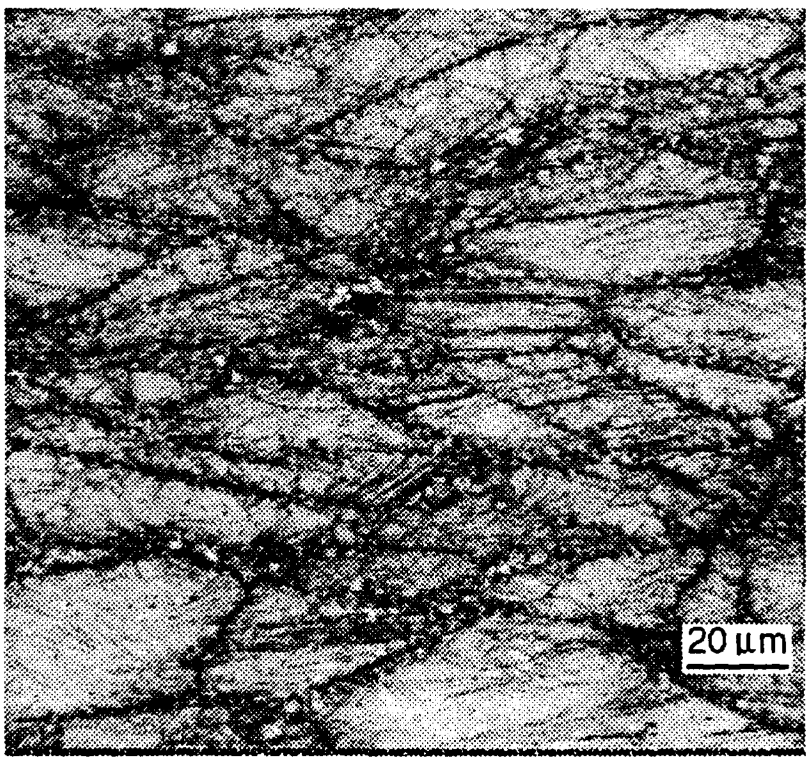

Figure 11. True stress-true strain curve and an optical micrograph from the center of the compressed sample cut through the compression axis, 900 C and 0.01 s^{-1}.

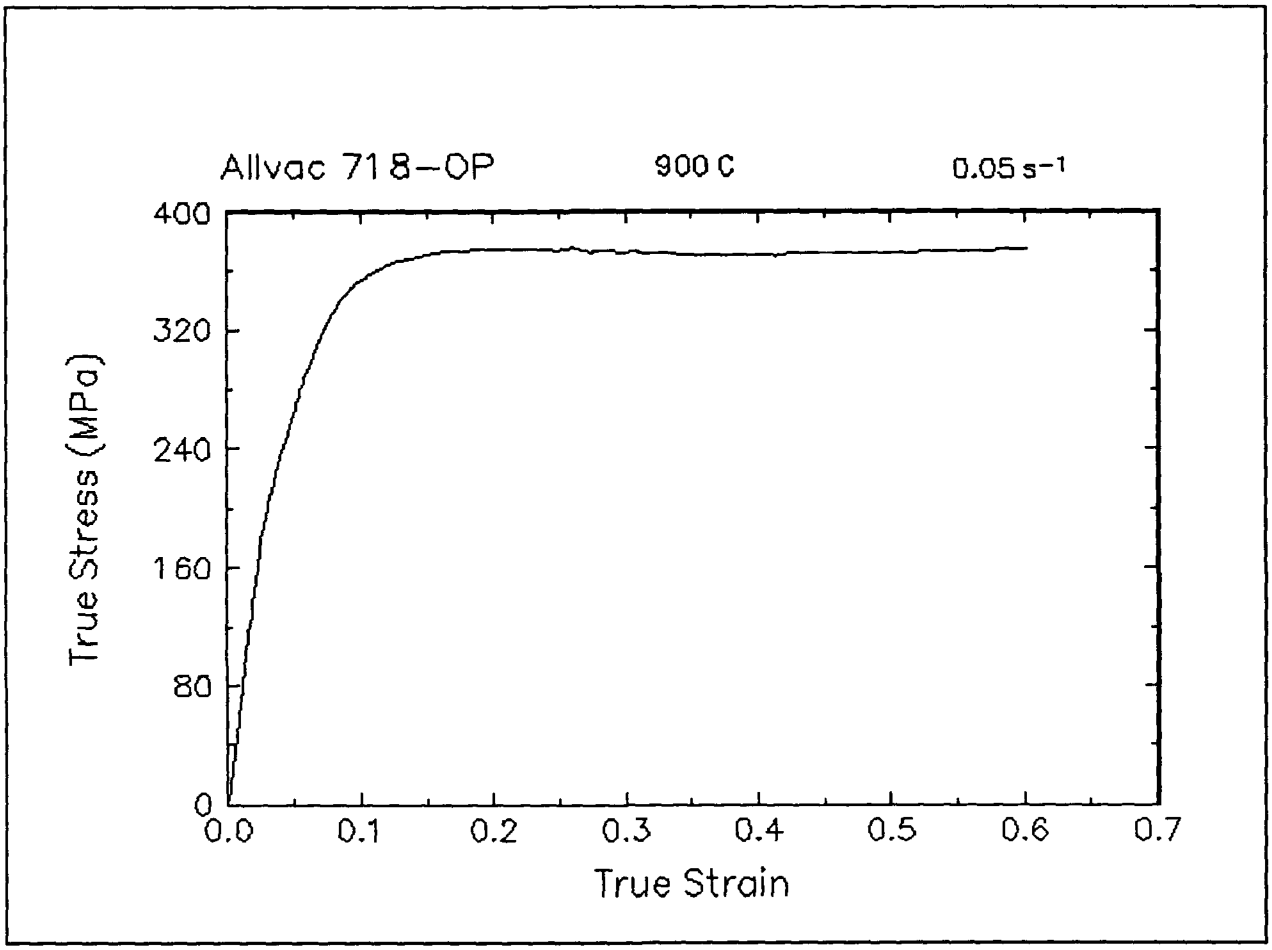

Figure 12. True stress-true strain curve, 900 C and 0.05 s^{-1}.

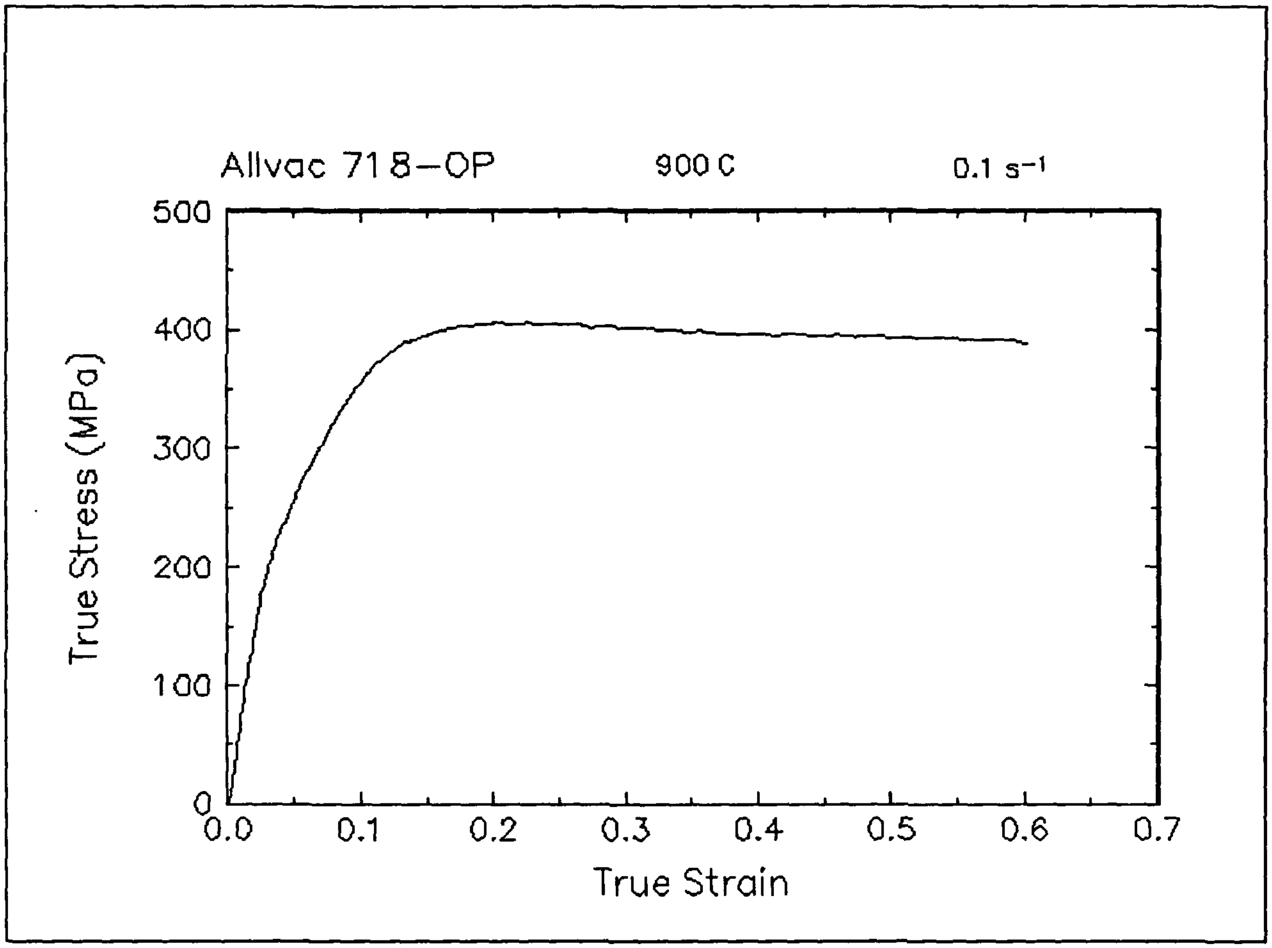

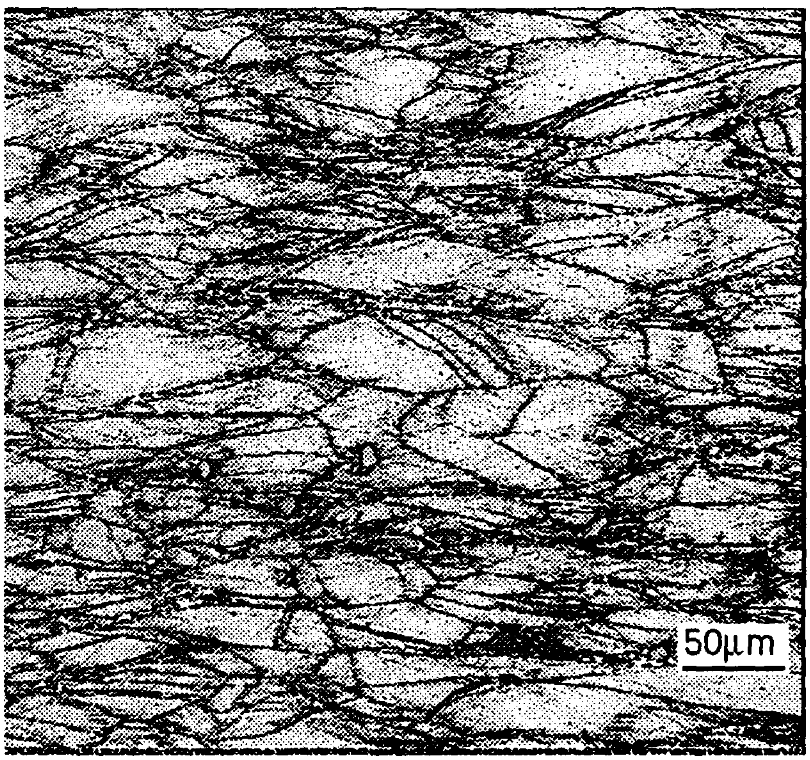

Figure 13. True stress-true strain curve and an optical micrograph from the center of the compressed sample cut through the compression axis, 900 C and 0.1 s^{-1}.

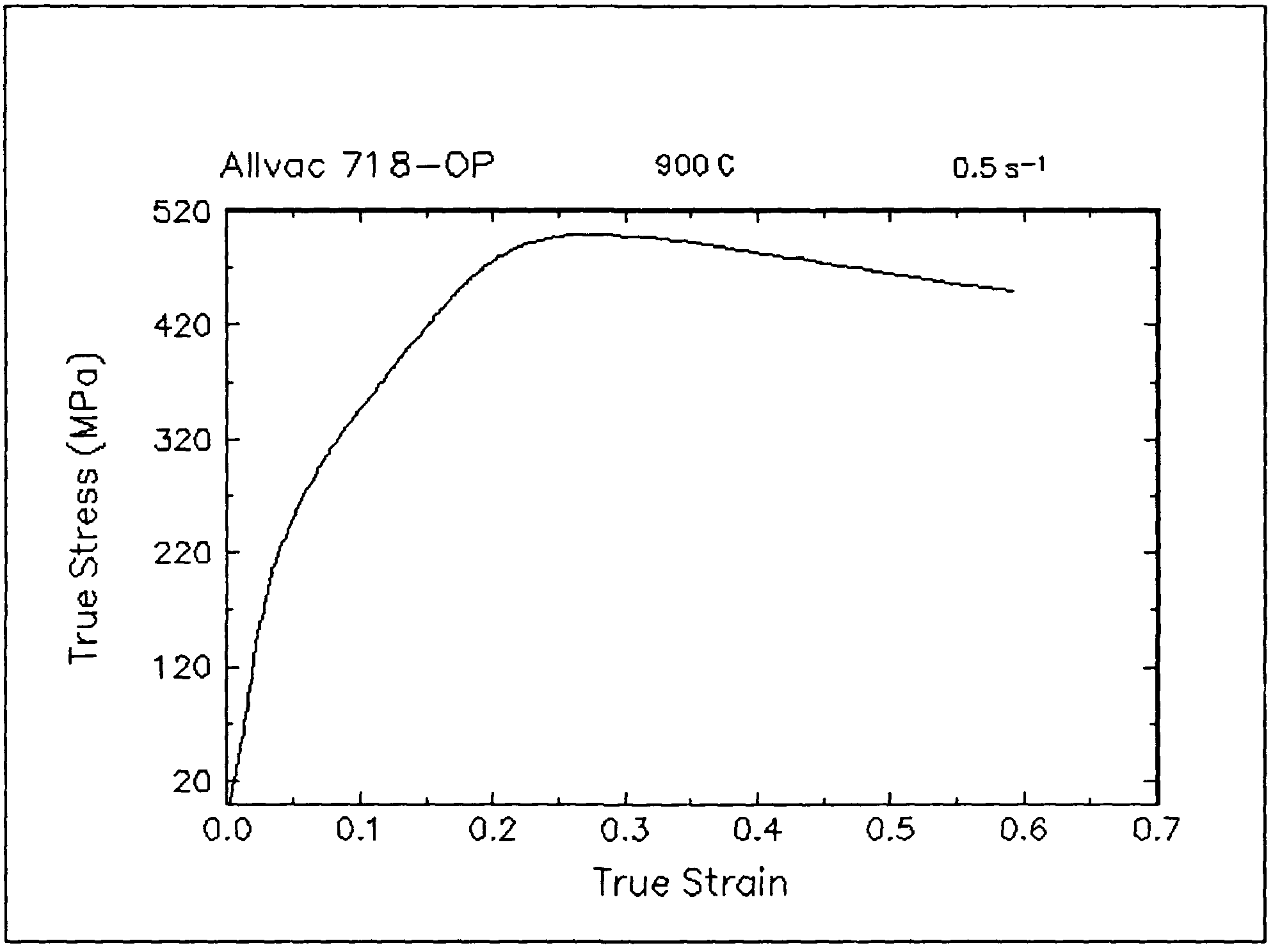

Figure 14. True stress-true strain curve, 900 C and 0.5 s^{-1}.

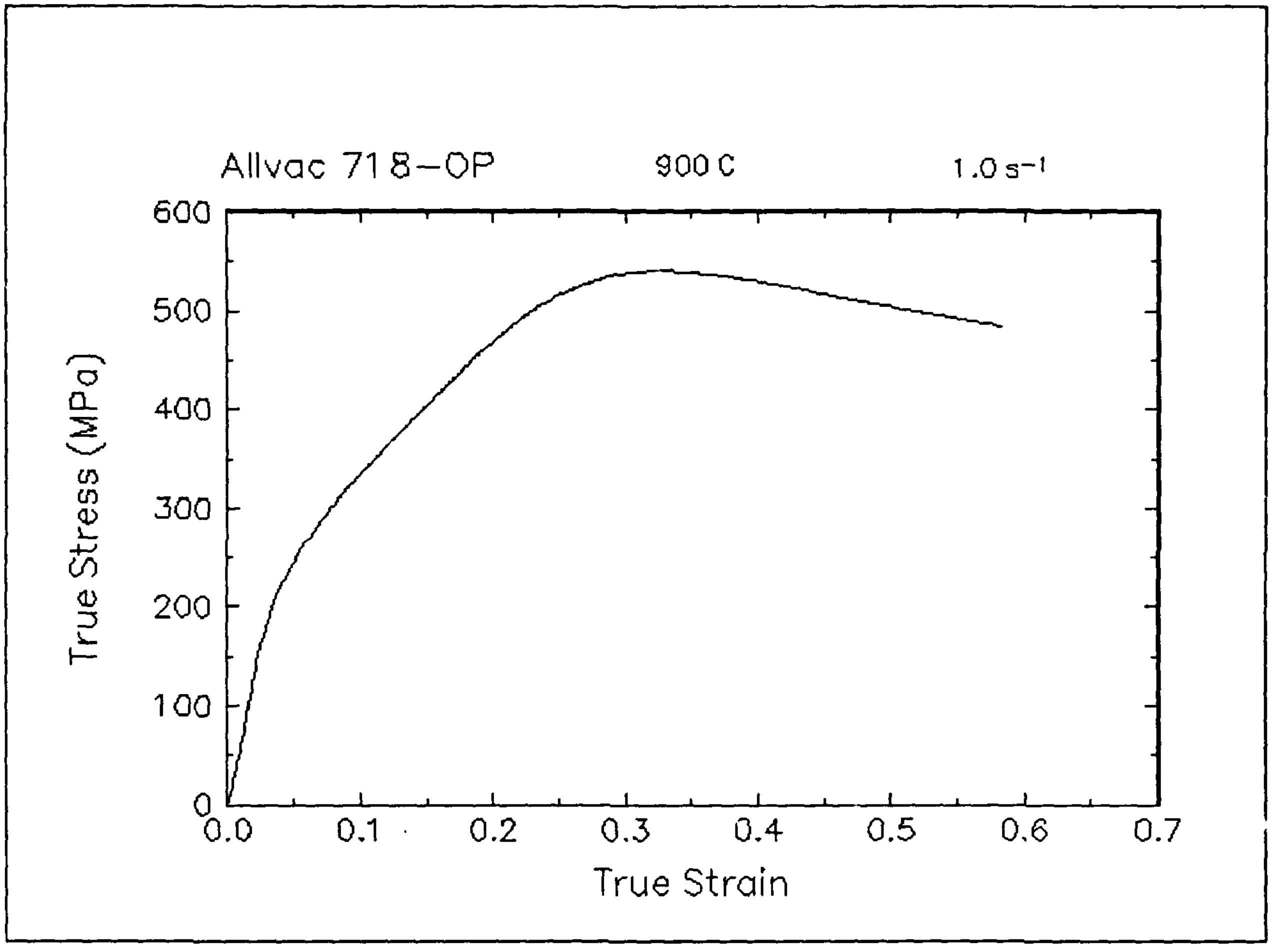

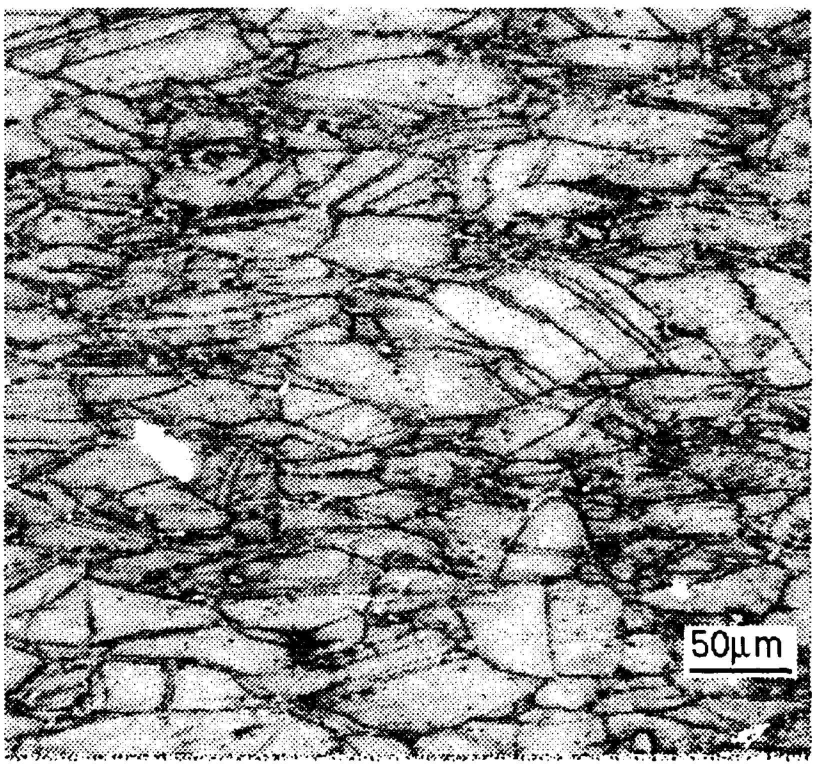

Figure 15. True stress-true strain curve and an optical micrograph from the center of the compressed sample cut through the compression axis, 900 C and 1 s^{-1}.

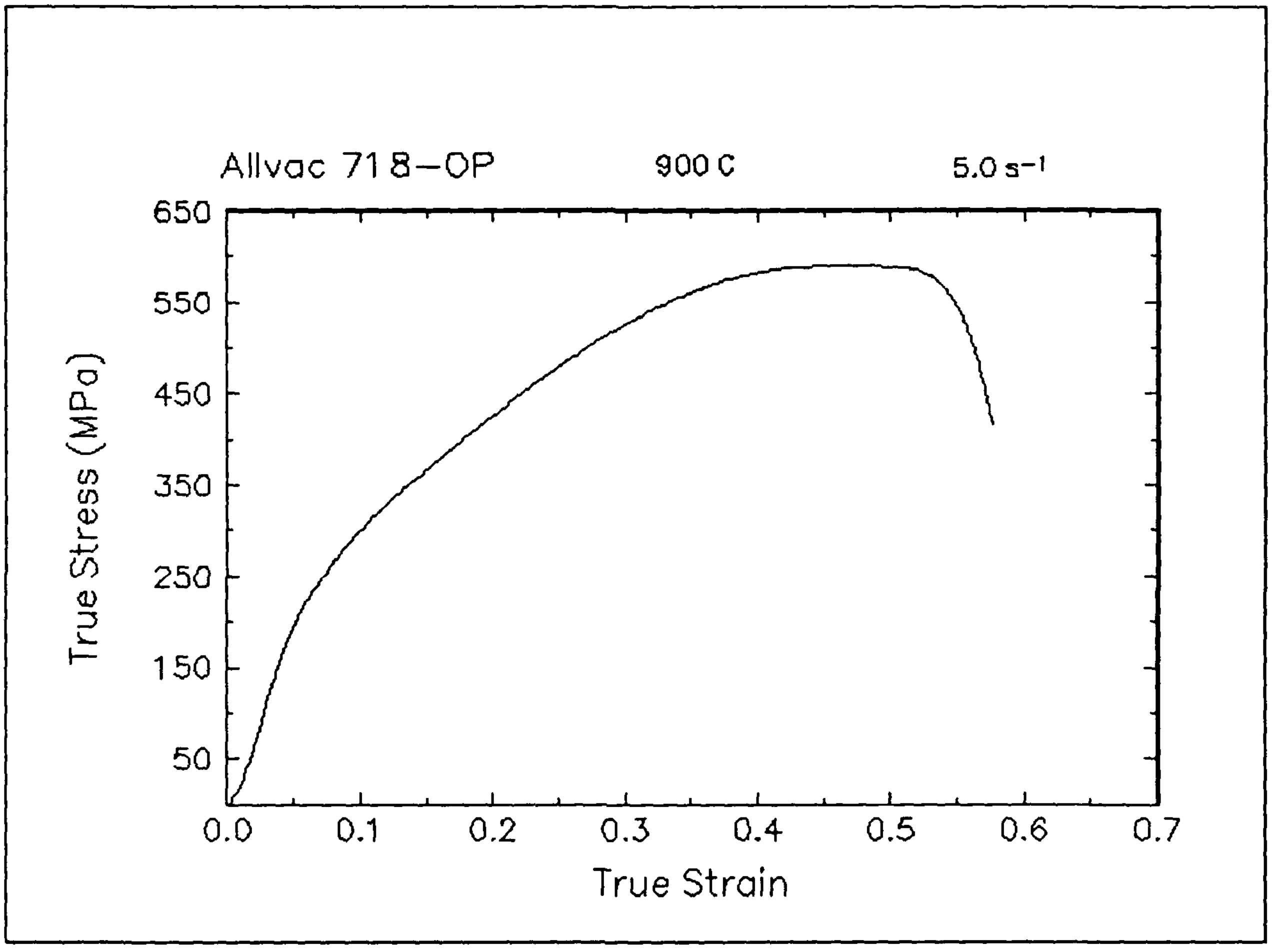

Figure 16. True stress-true strain curve, 900 C and 5 s^{-1}.

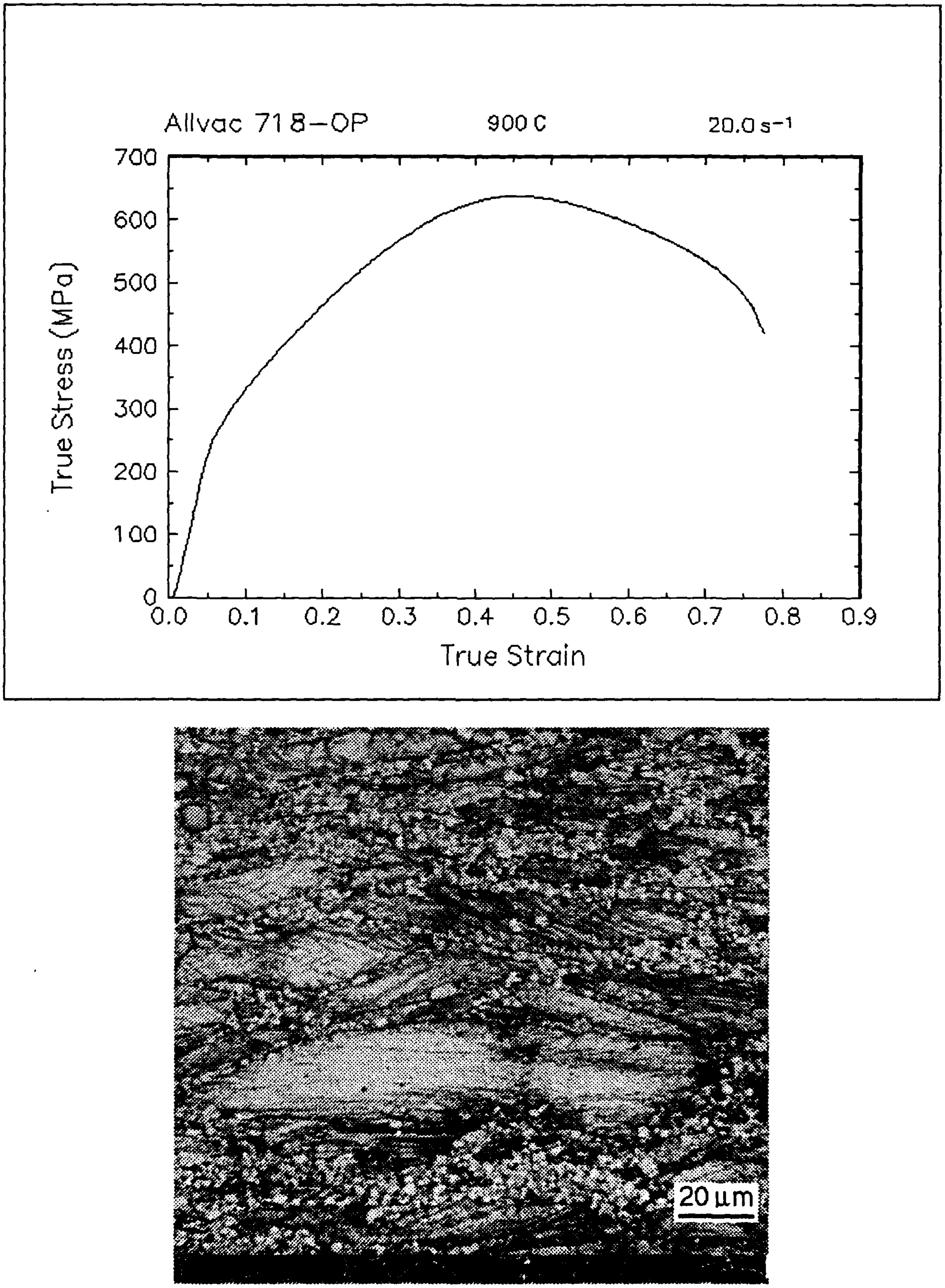

Figure 17. True stress-true strain curve and an optical micrograph from the center of the compressed sample cut through the compression axis, 900 C and 20 s^{-1}.

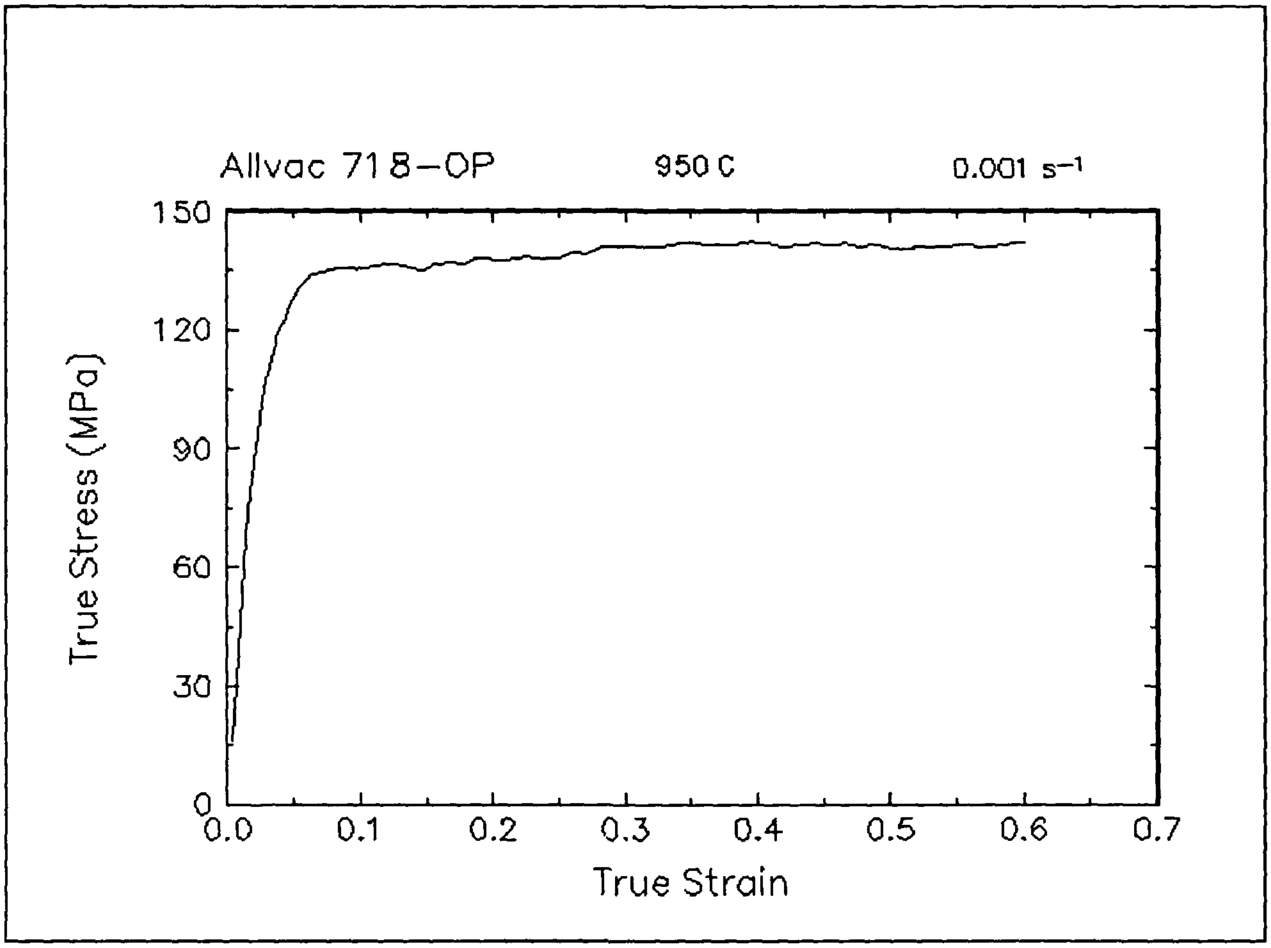

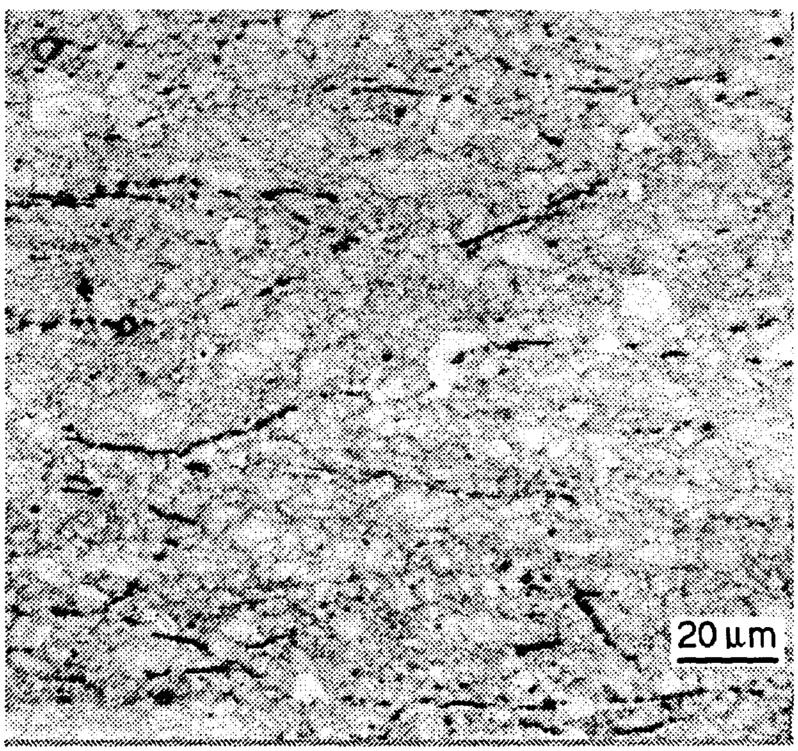

Figure 18. True stress-true strain curve and an optical micrograph from the center of the compressed sample cut through the compression axis, 950 C and 0.001 s^{-1}.

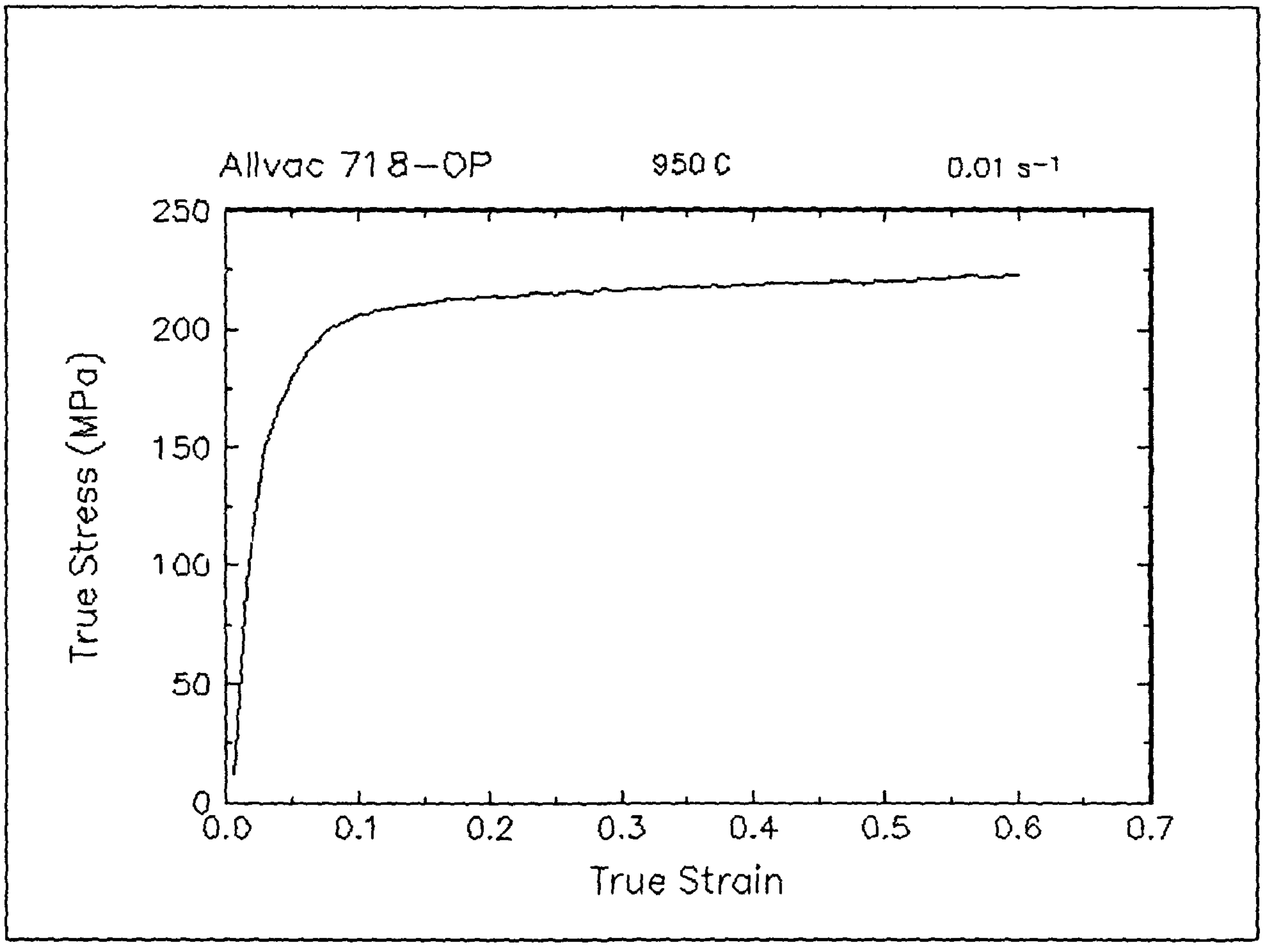

Figure 19. True stress-true strain curve, 950 C and 0.01 s^{-1}.

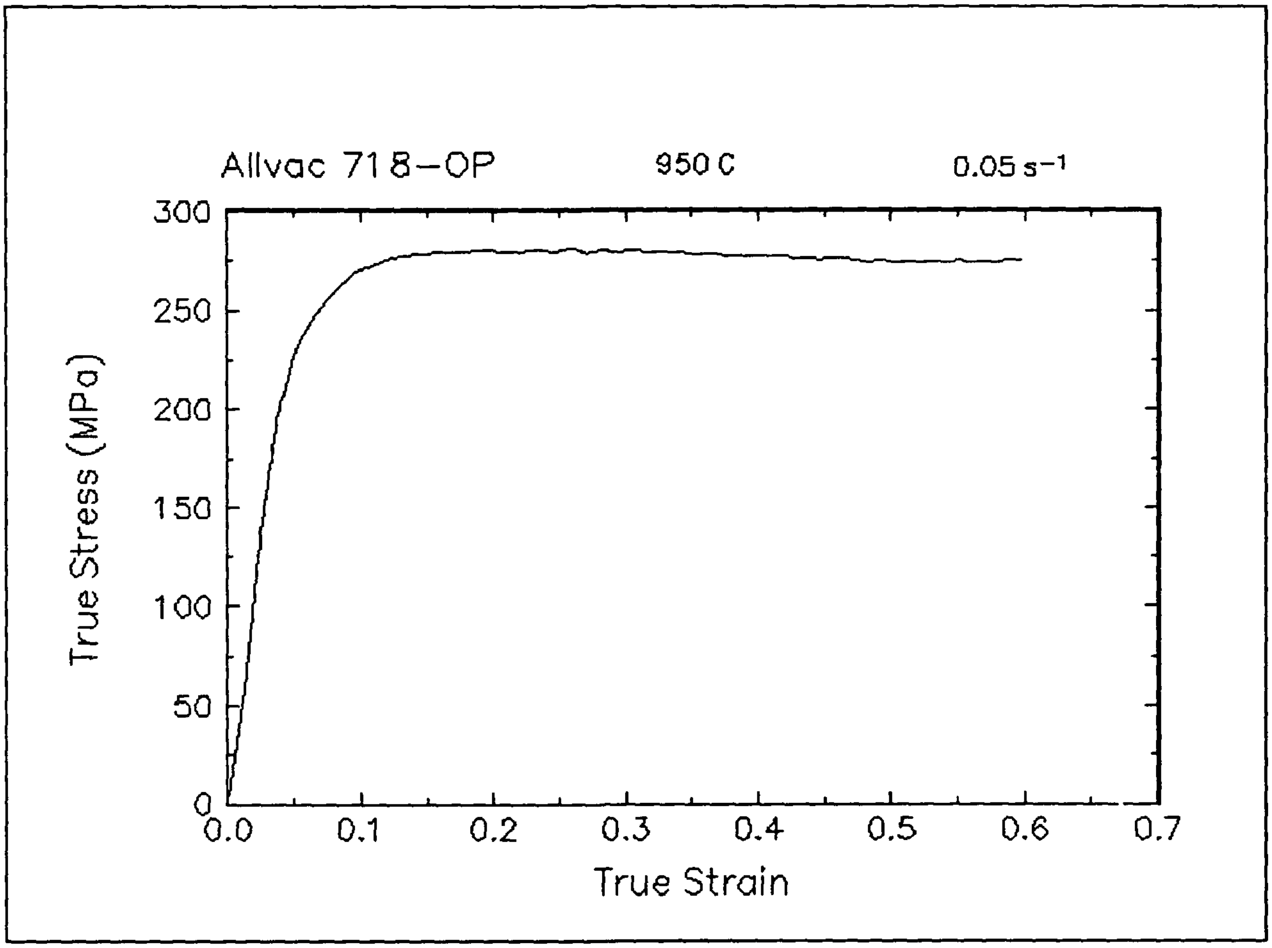

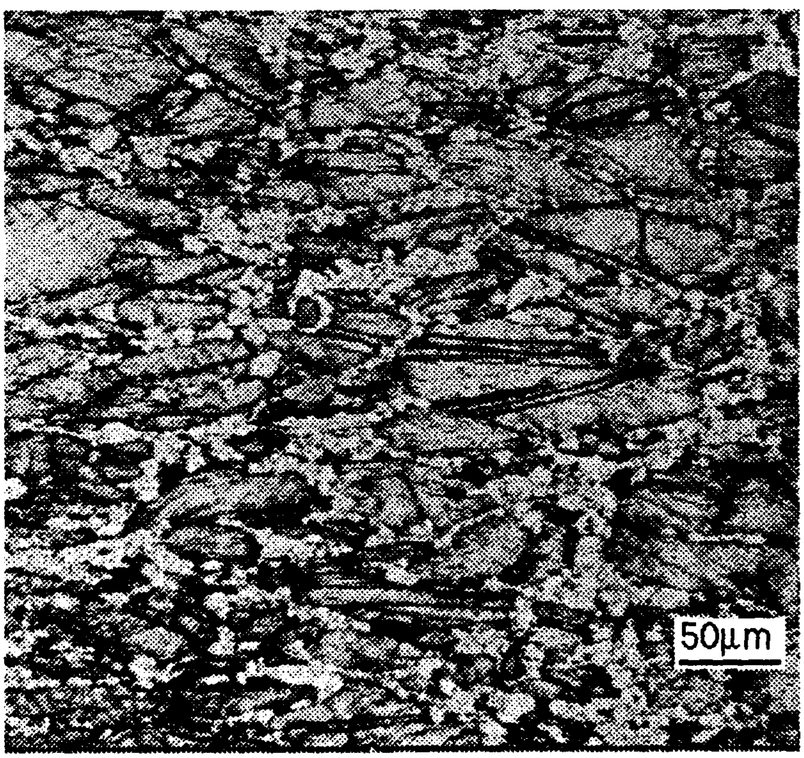

Figure 20. True stress-true strain curve and an optical micrograph from the center of the compressed sample cut through the compression axis, 950 C and 0.05 s^{-1}.

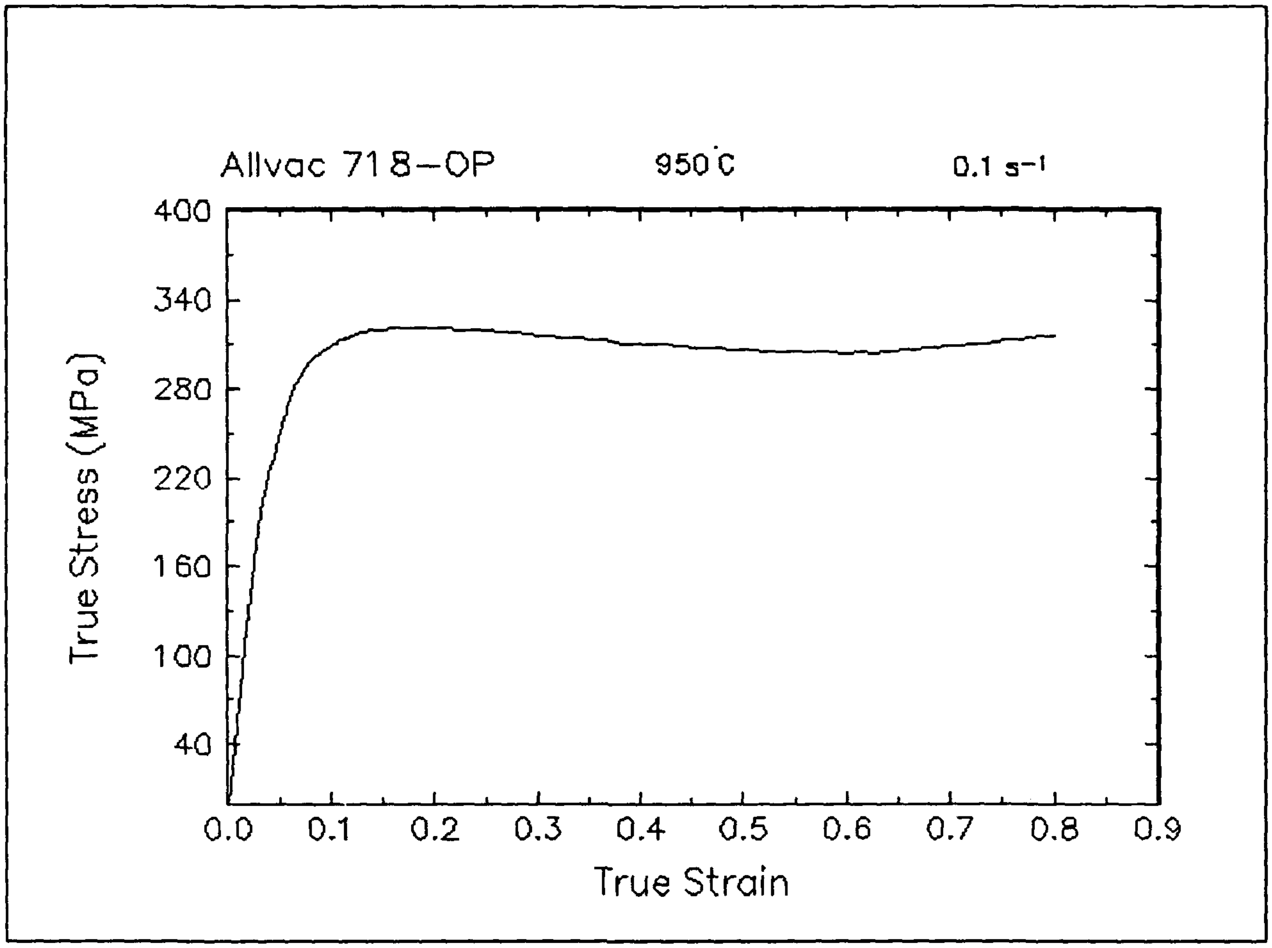

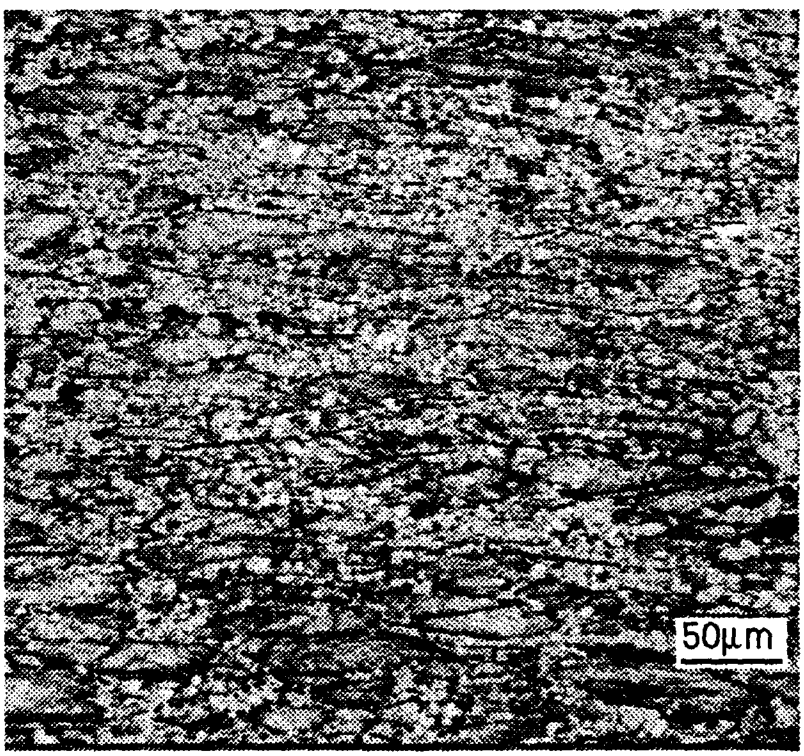

Figure 21. True stress-true strain curve and an optical micrograph from the center of the compressed sample cut through the compression axis, 950 C and 0.1 s^{-1}.

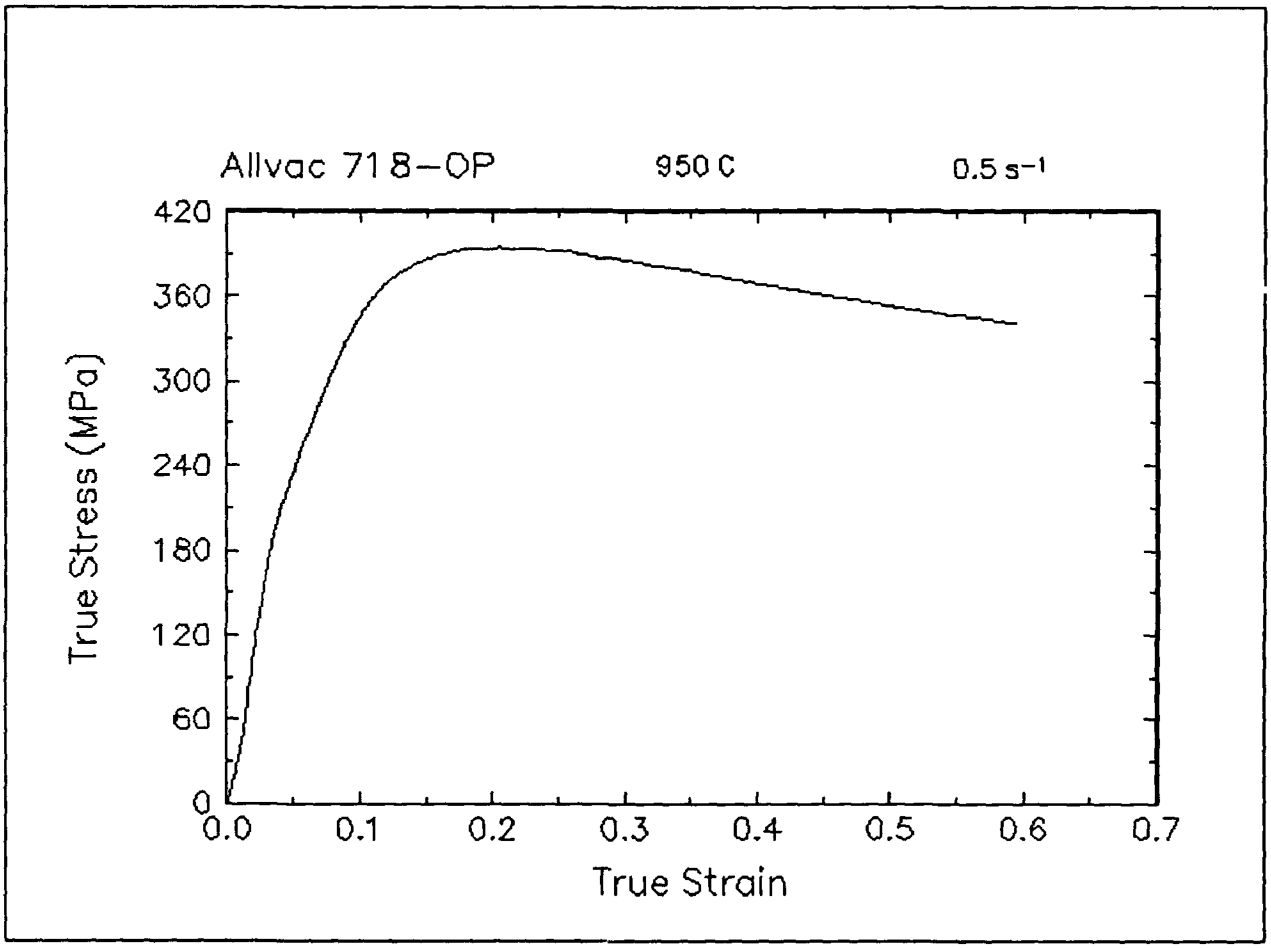

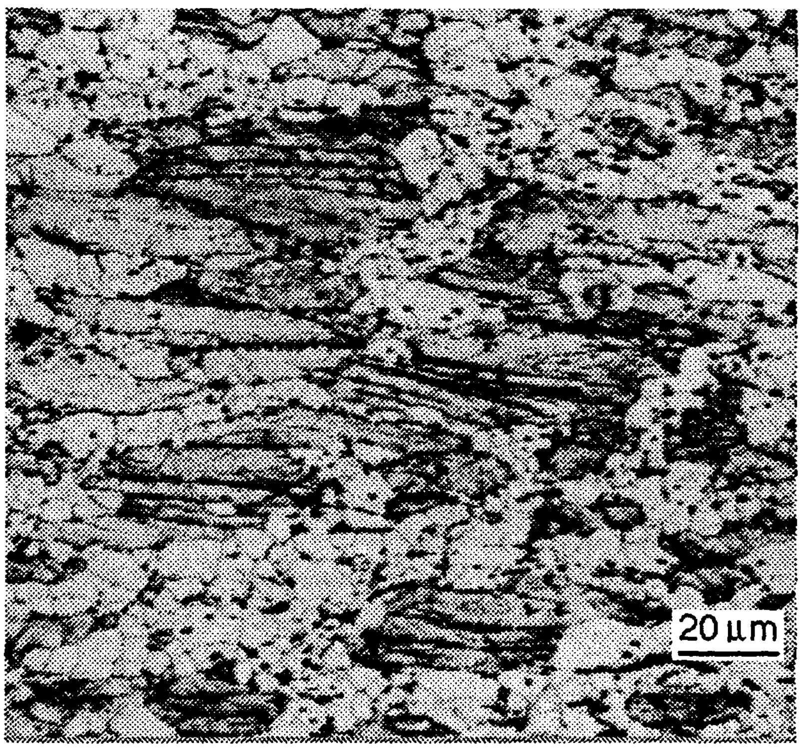

Figure 22. True stress-true strain curve and an optical micrograph from the center of the compressed sample cut through the compression axis, 950 C and 0.5 s^{-1}.

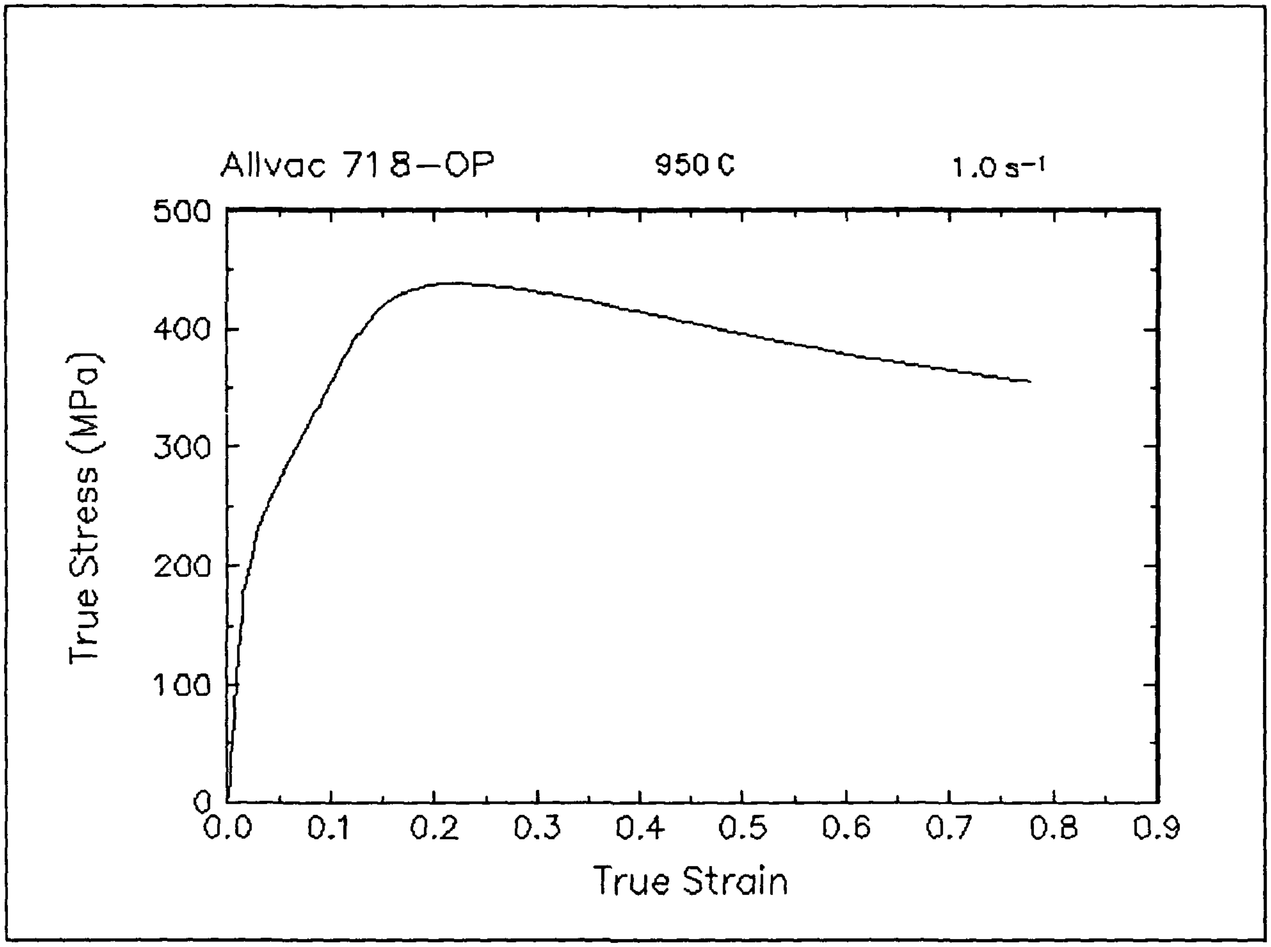

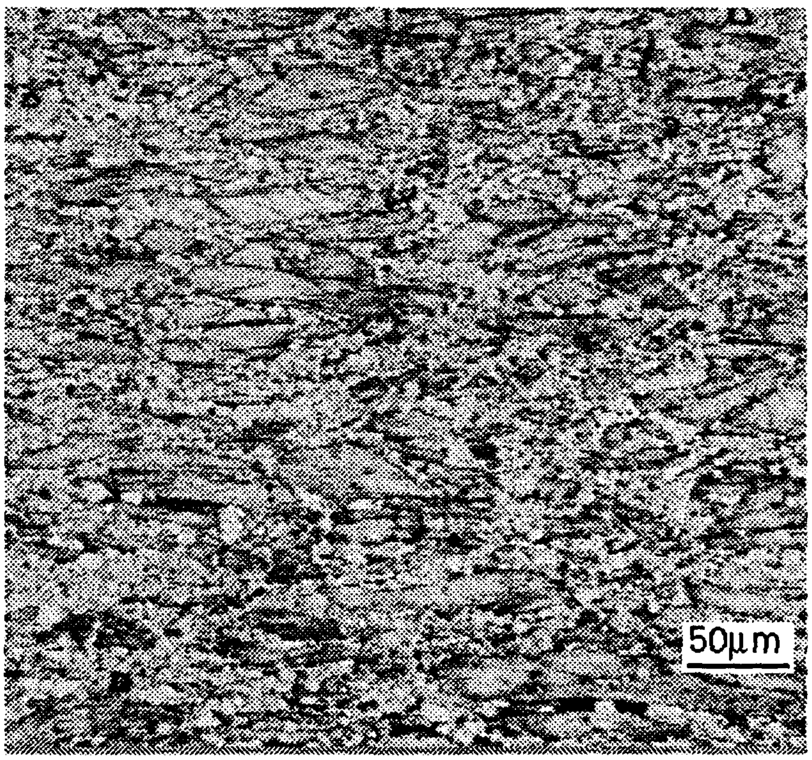

Figure 23. True stress-true strain curve and an optical micrograph from the center of the compressed sample cut through the compression axis, 950 C and 1 s^{-1}.

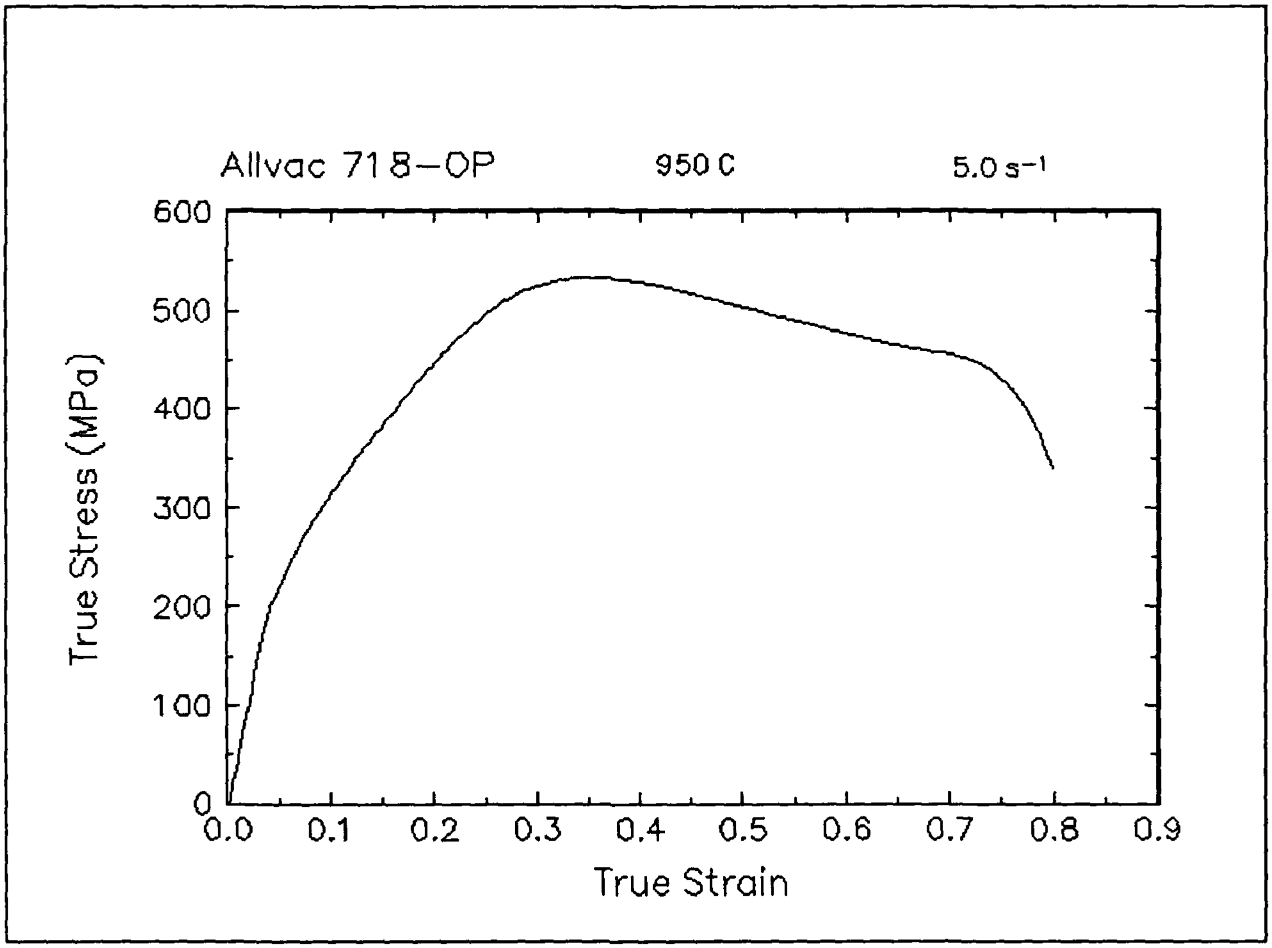

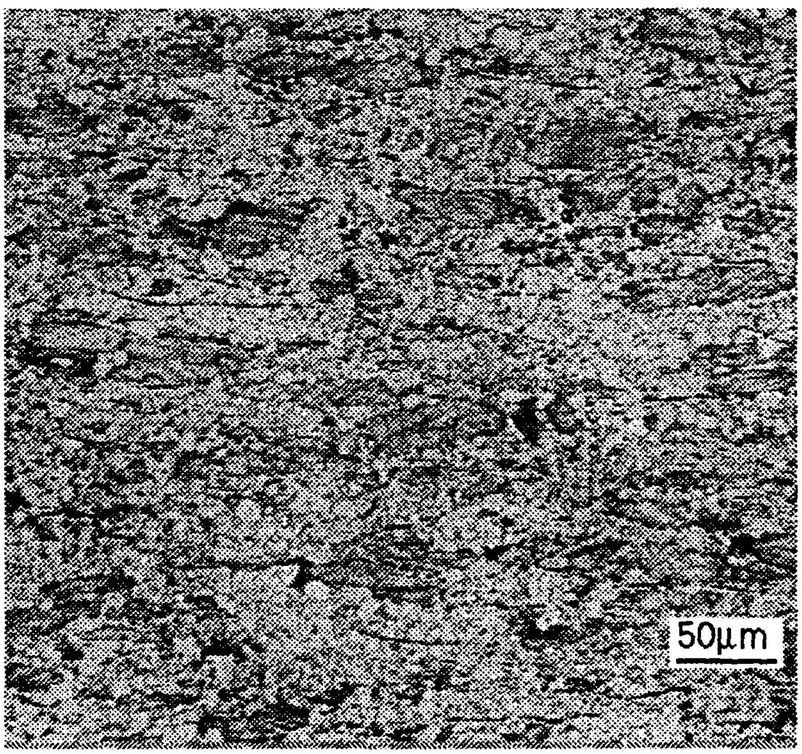

Figure 24. True stress-true strain curve and an optical micrograph from the center of the compressed sample cut through the compression axis, 950 C and 5 s^{-1}.

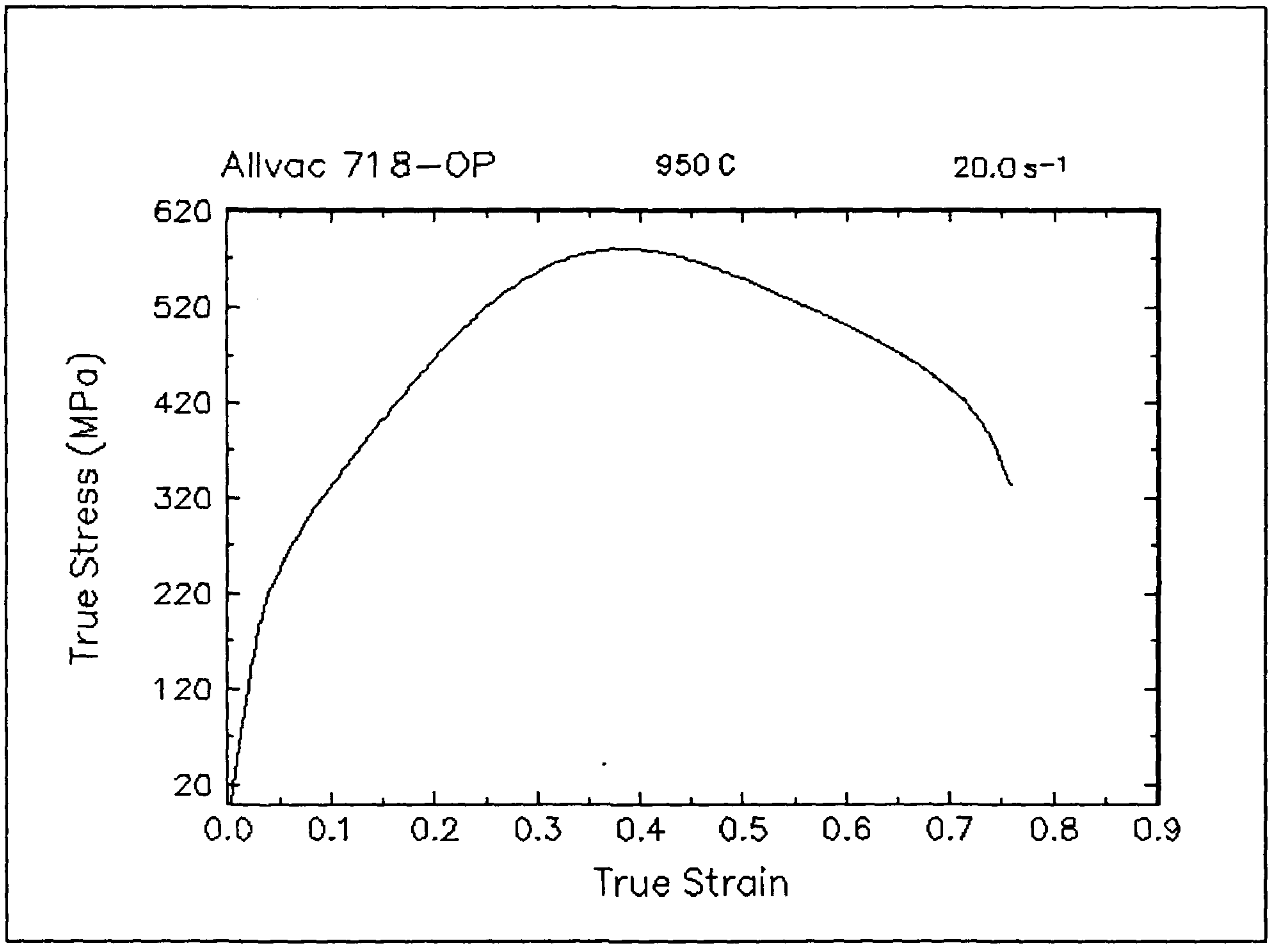

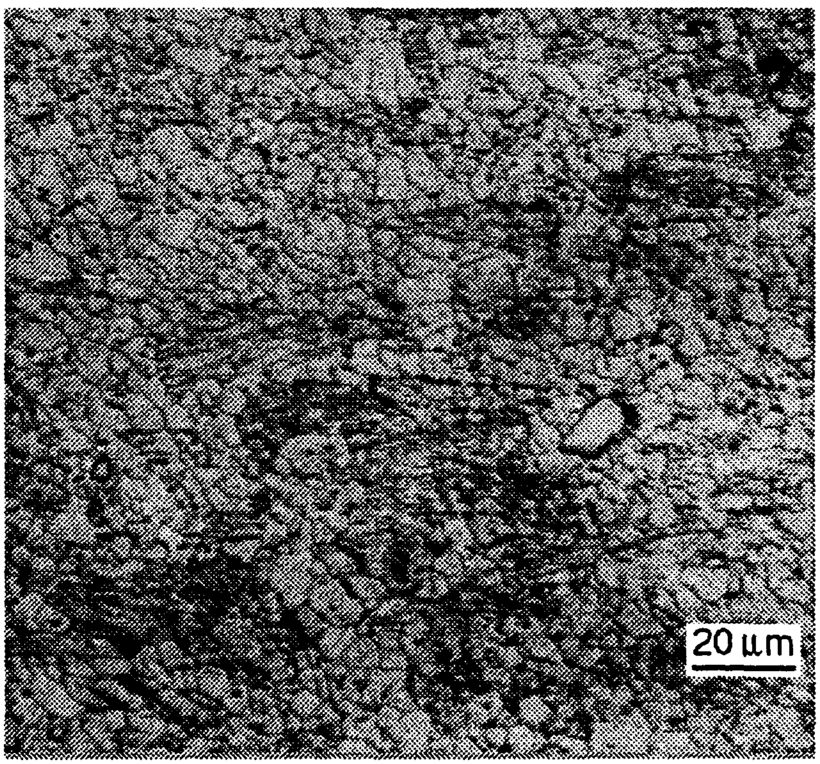

Figure 25. True stress-true strain curve and an optical micrograph from the center of the compressed sample cut through the compression axis, 950 C and 20 s^{-1}.

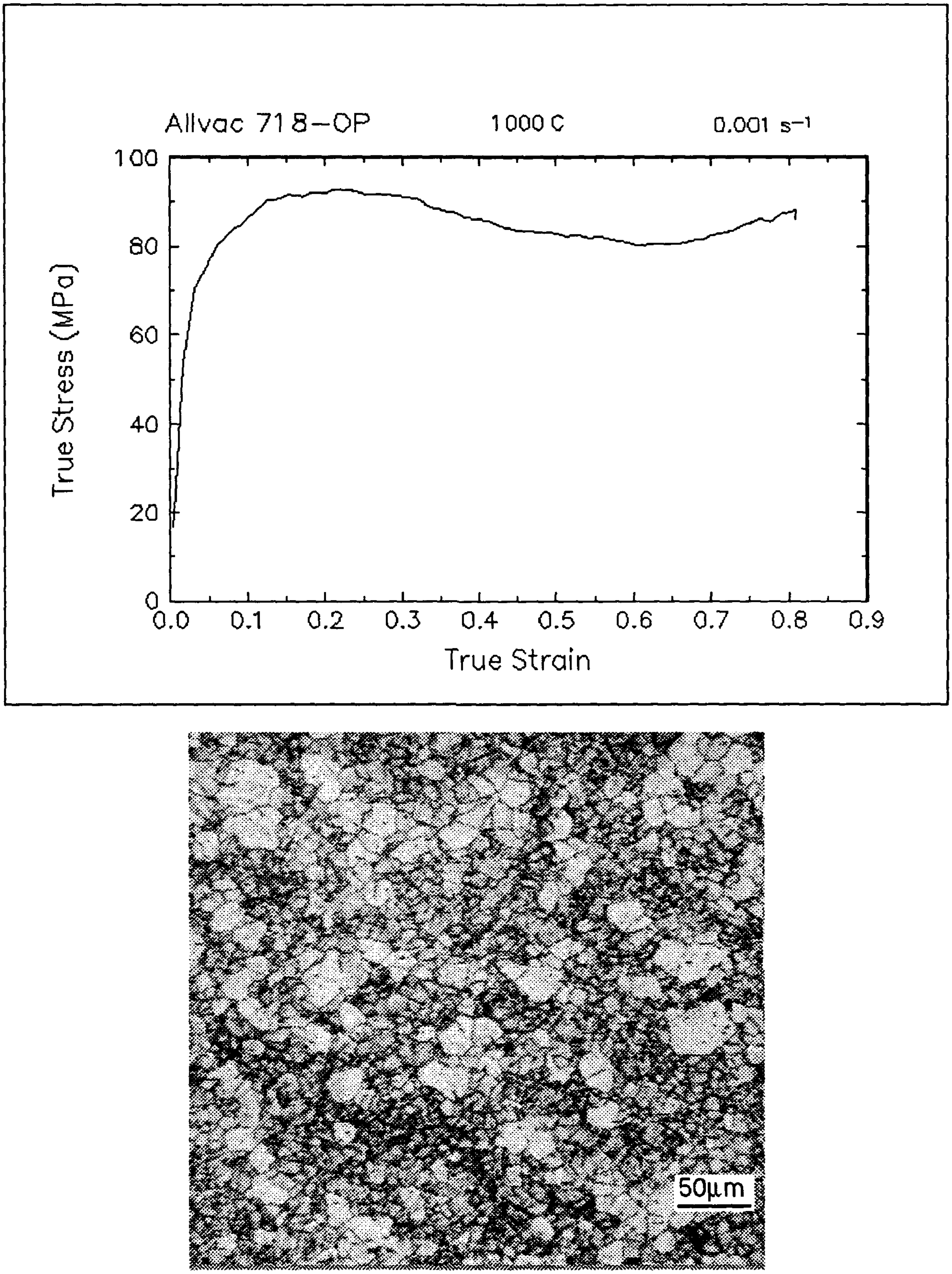

Figure 26. True stress-true strain curve and an optical micrograph from the center of the compressed sample cut through the compression axis, 1000 C and 0.001 s^{-1}.

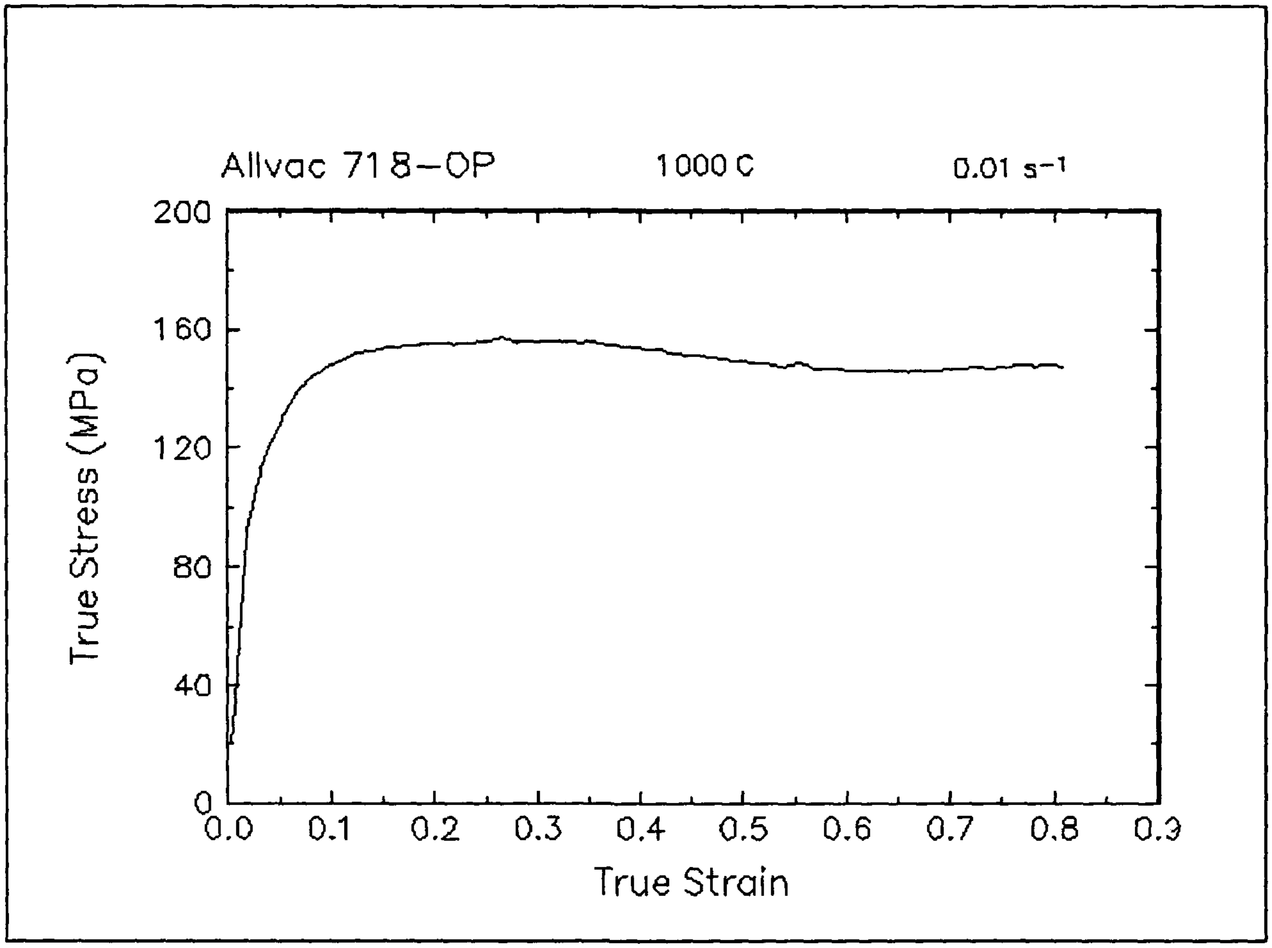

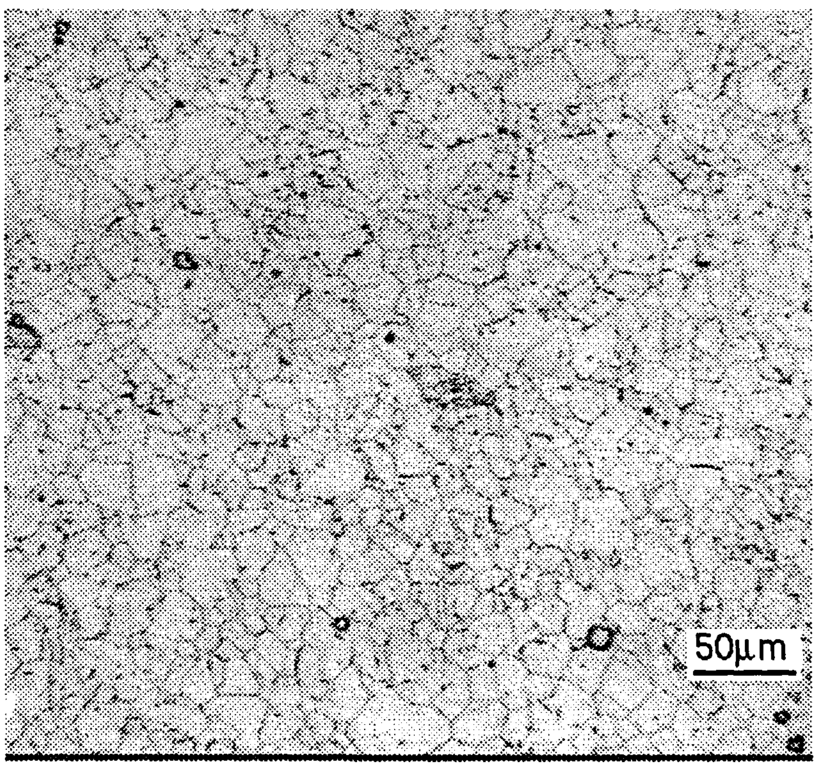

Figure 27. True stress-true strain curve and an optical micrograph from the center of the compressed sample cut through the compression axis, 1000 C and 0.01 s^{-1}.

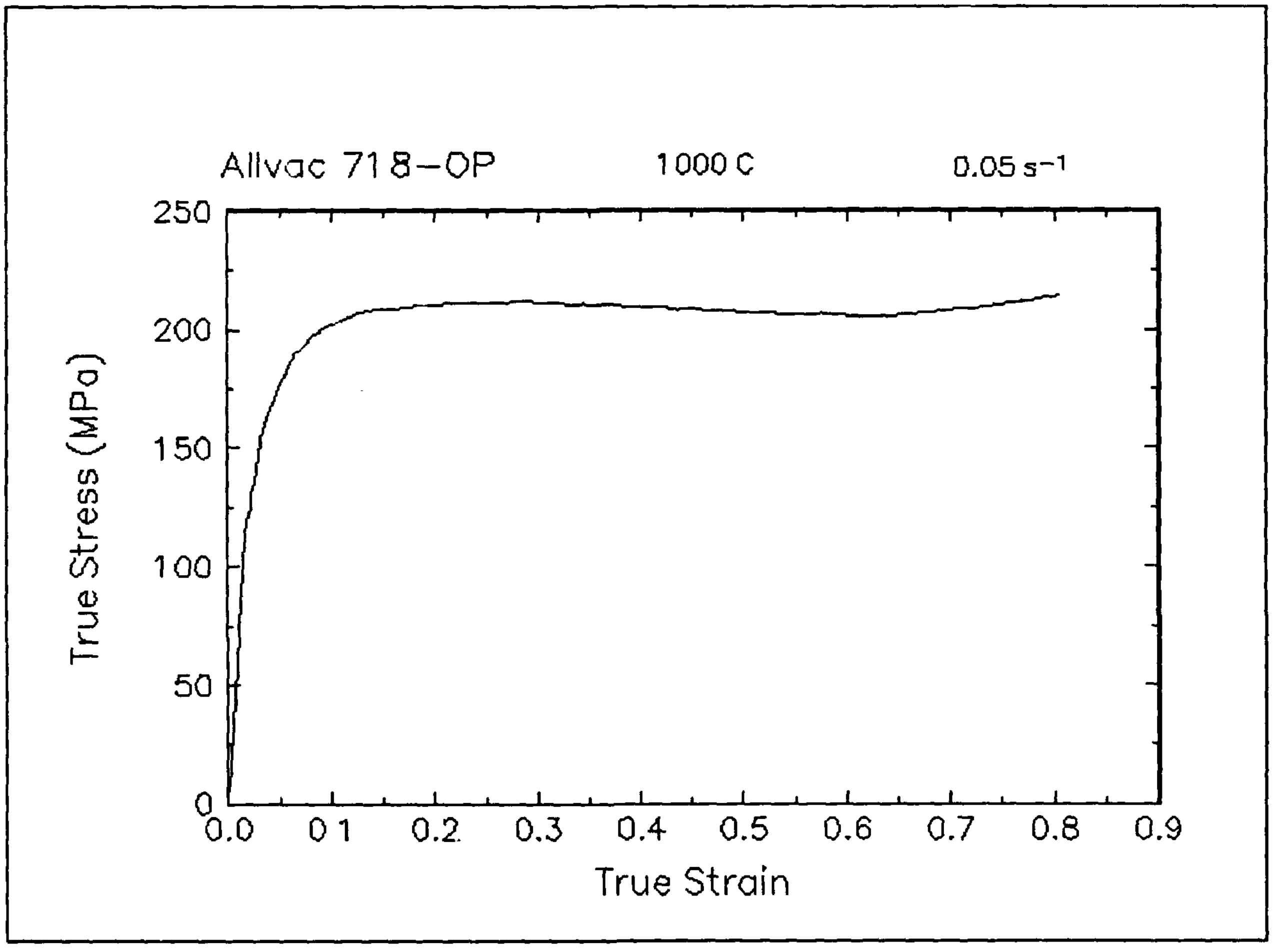

Figure 28. True stress-true strain curve, 1000 C and 0.05 s^{-1}.

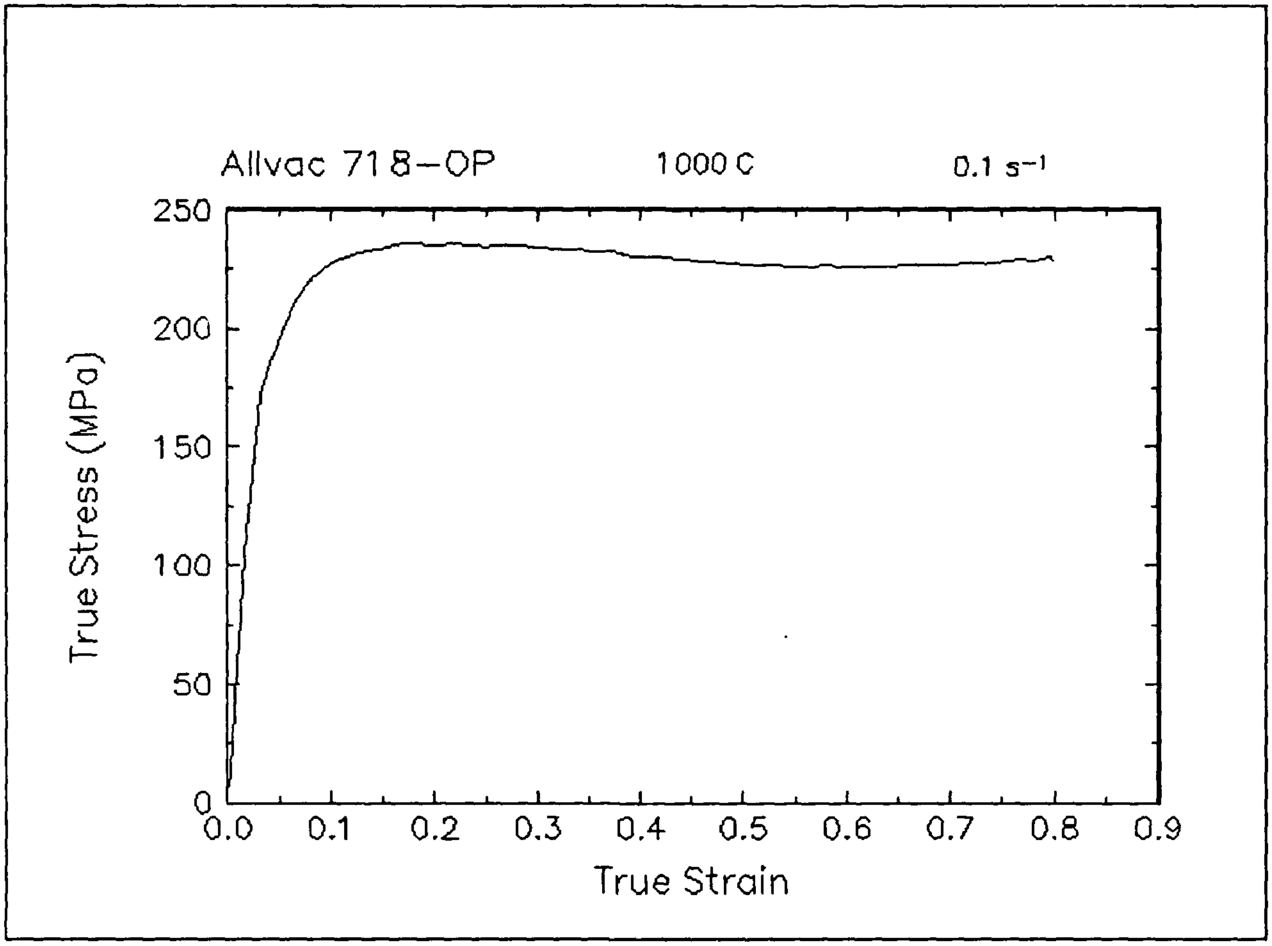

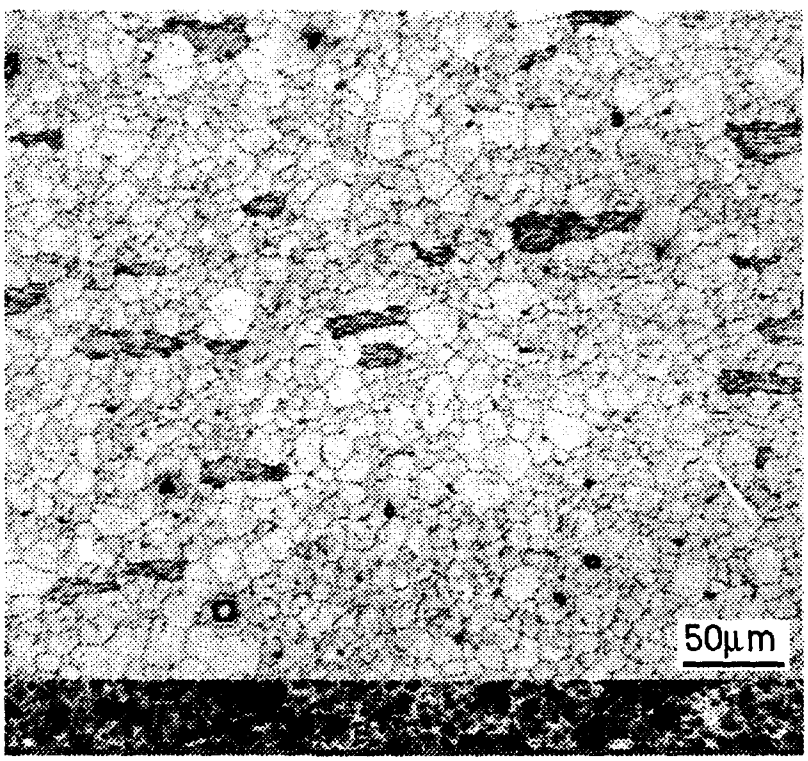

Figure 29. True stress-true strain curve and an optical micrograph from the center of the compressed sample cut through the compression axis, 1000 C and 0.1 s^{-1}.

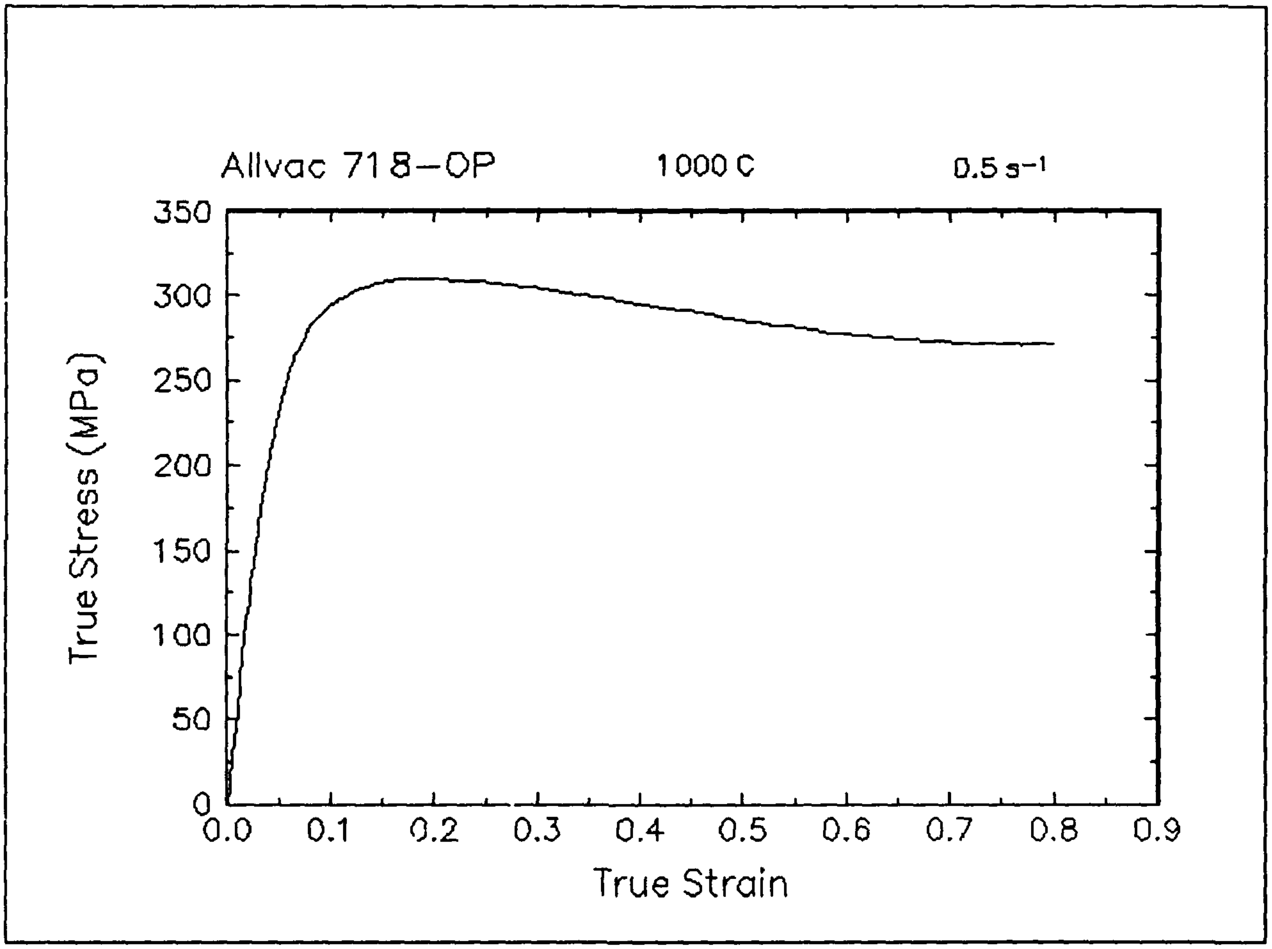

Figure 30. True stress-true strain curve, 1000 C and 0.5 s^{-1}.

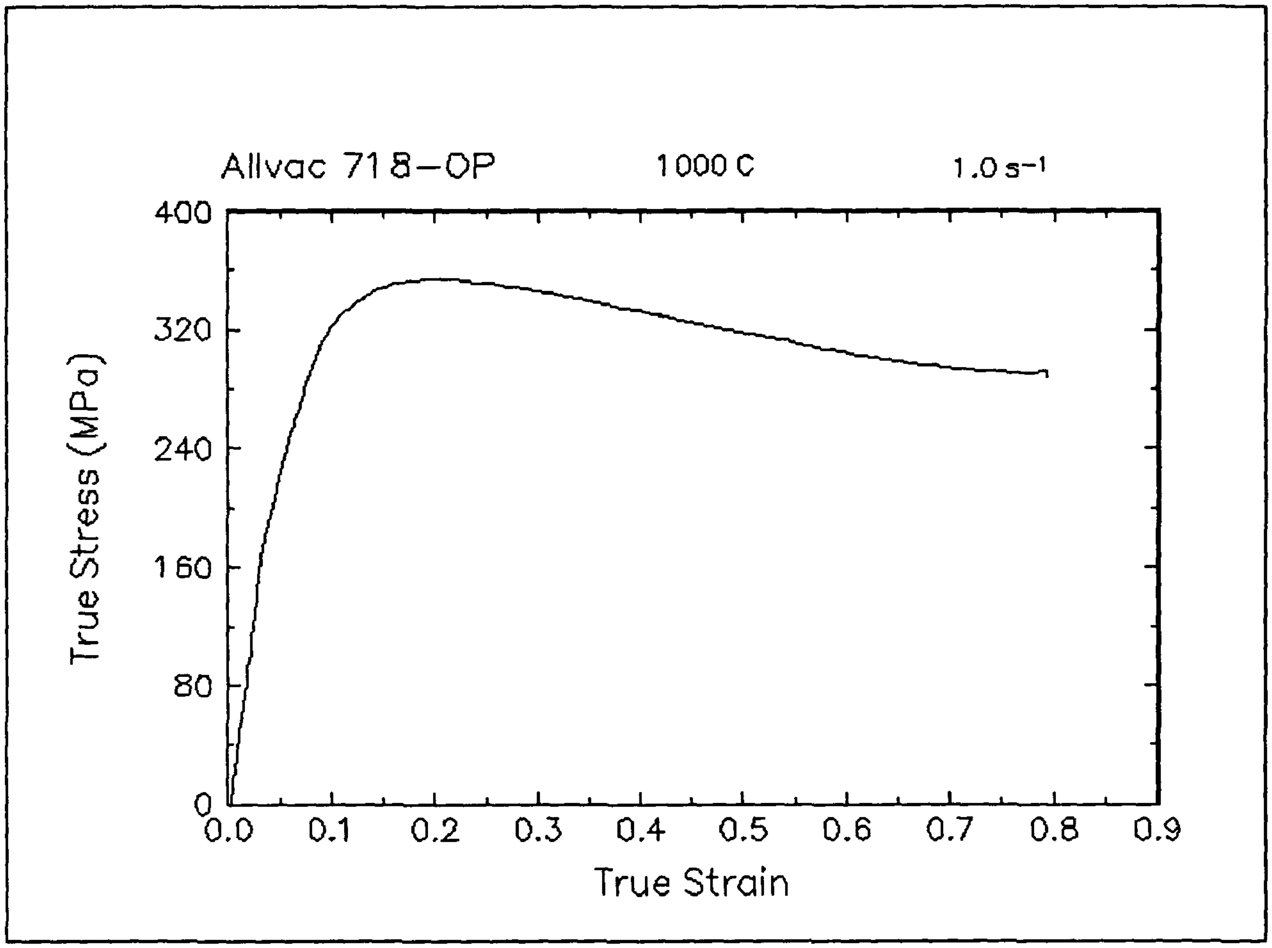

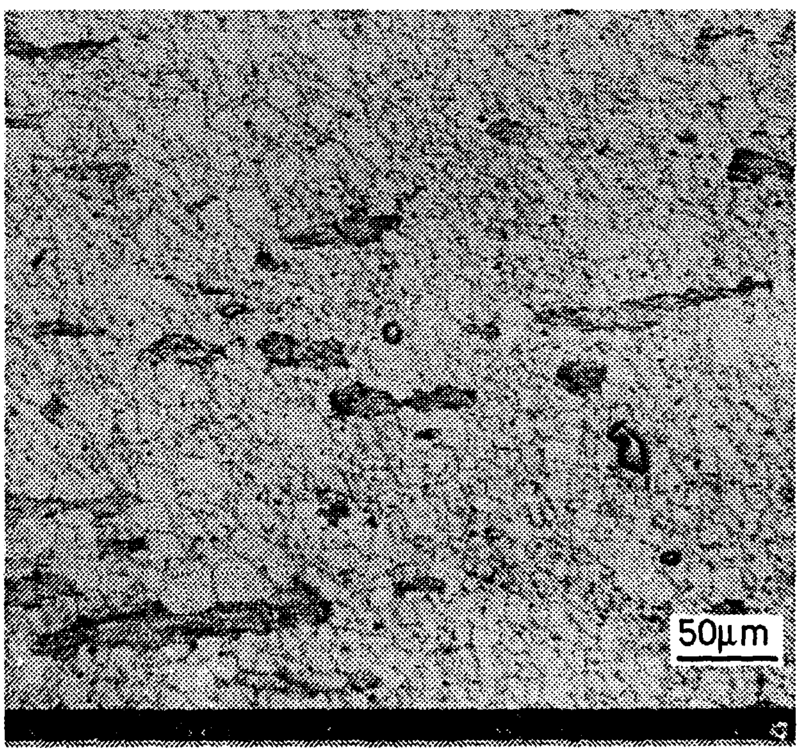

Figure 31. True stress-true strain curve and an optical micrograph from the center of the compressed sample cut through the compression axis, 1000 C and 1 s^{-1}.

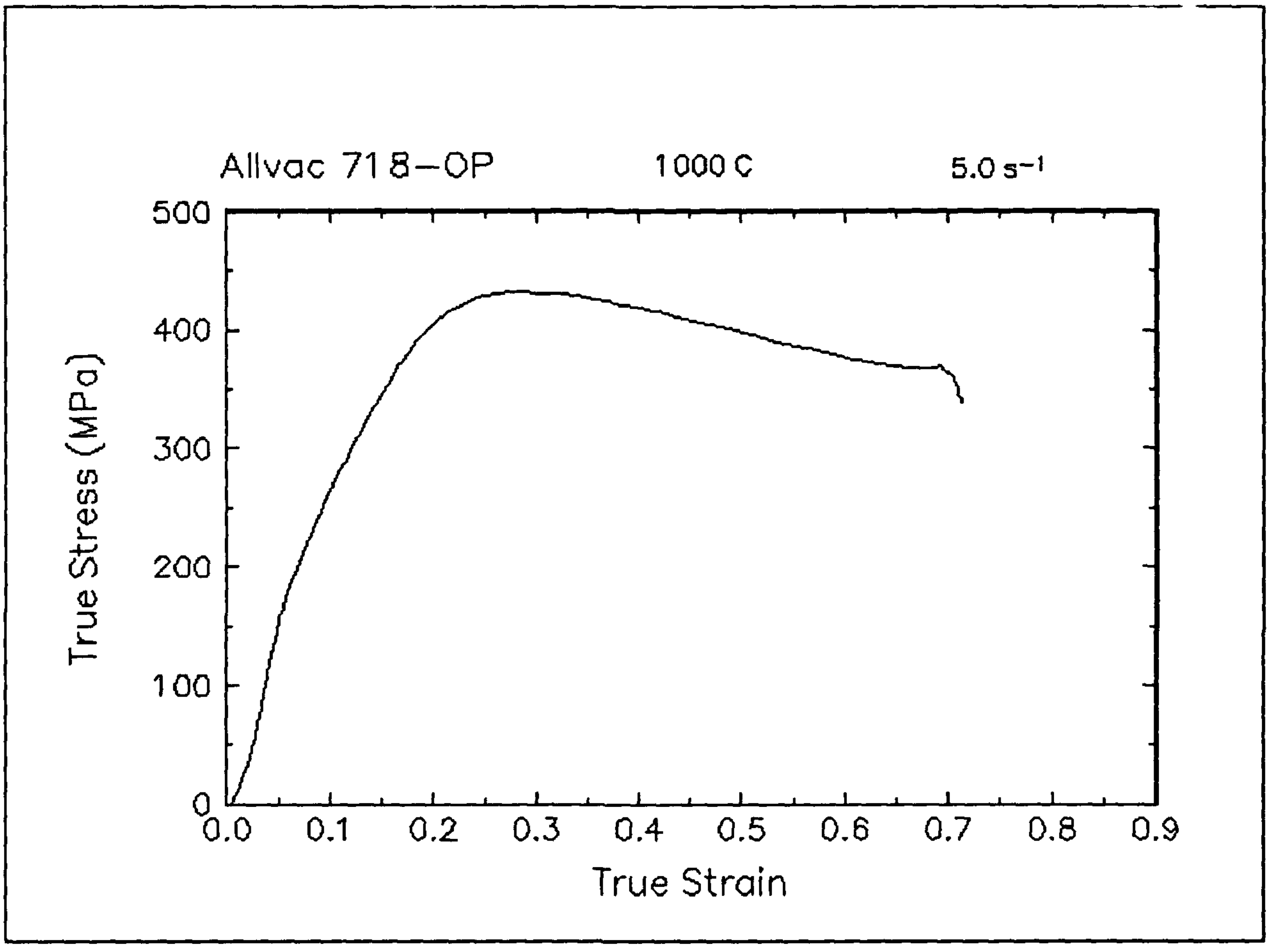

Figure 32. True stress-true strain curve, 1000 C and 5 s^{-1}.

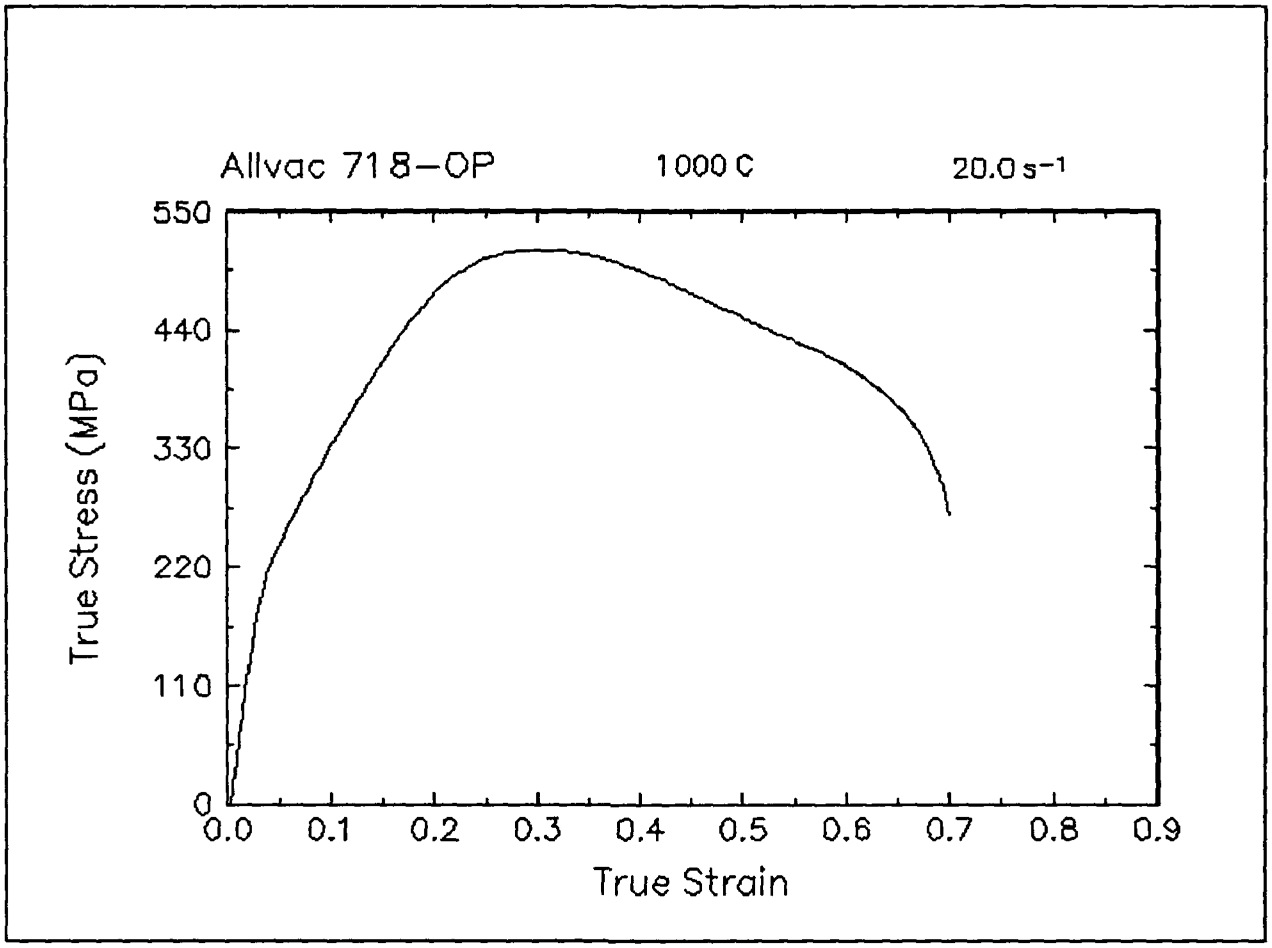

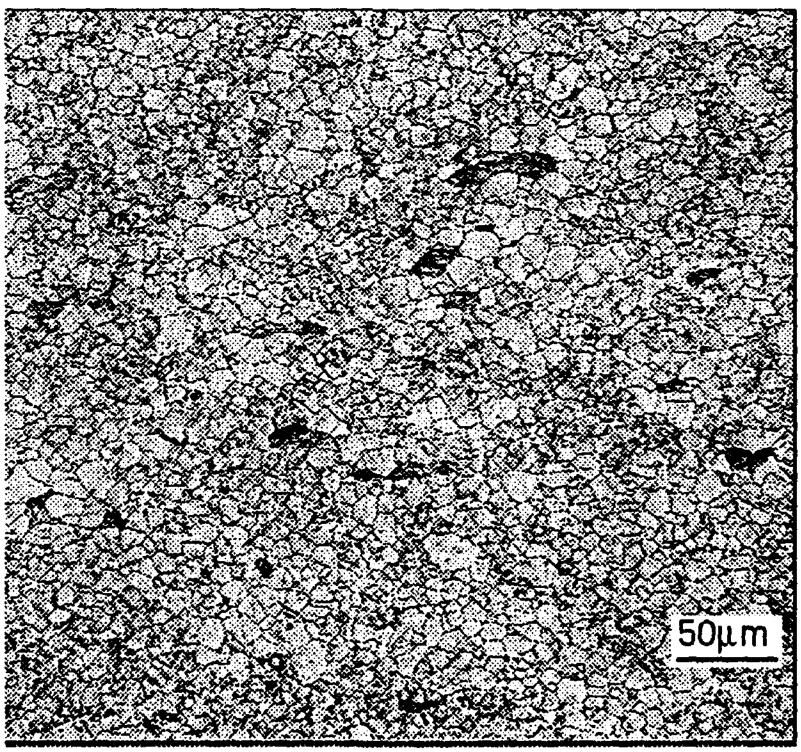

Figure 33. True stress-true strain curve and an optical micrograph from the center of the compressed sample cut through the compression axis, 1000 C and 20 s^{-1}.

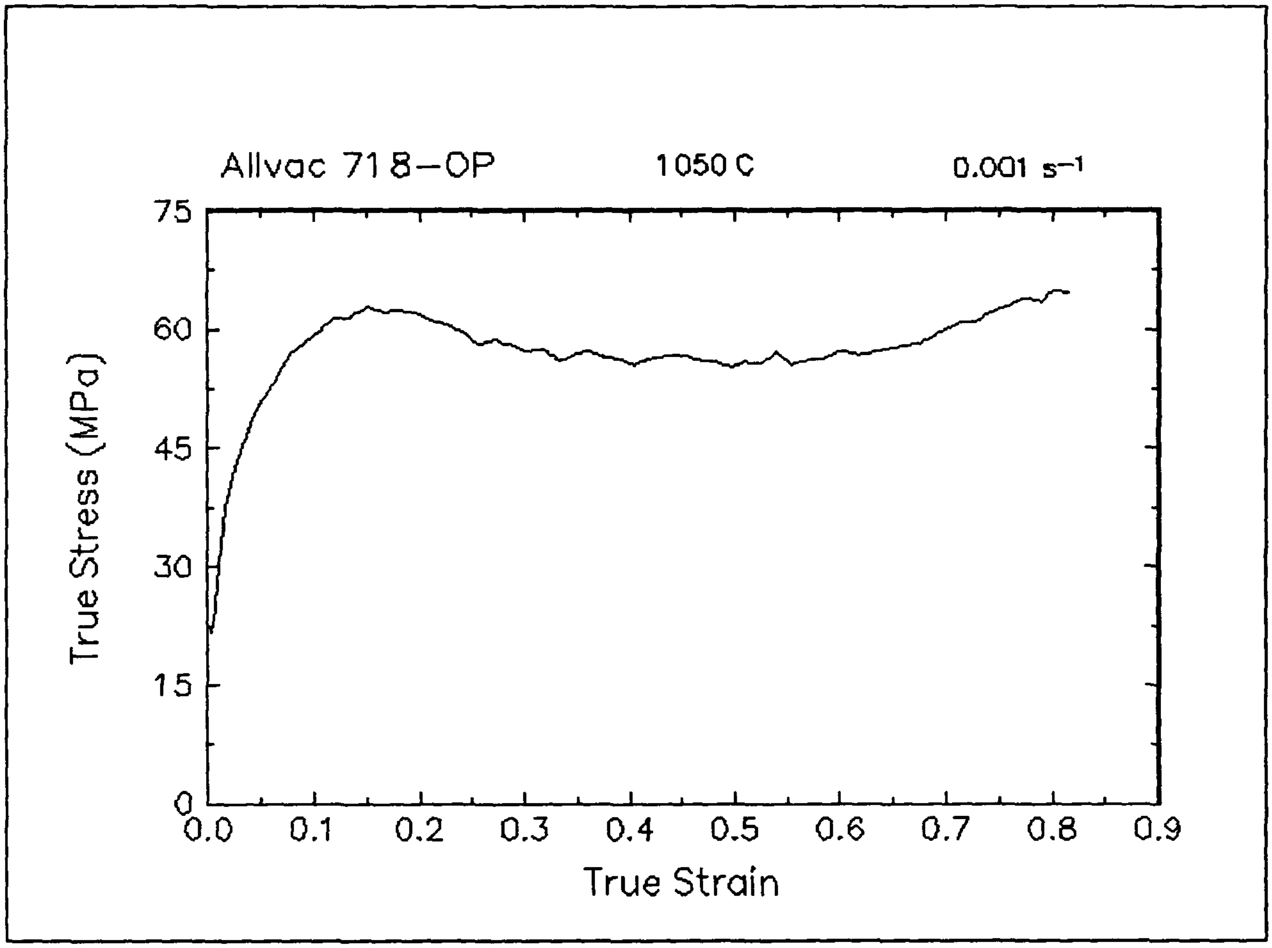

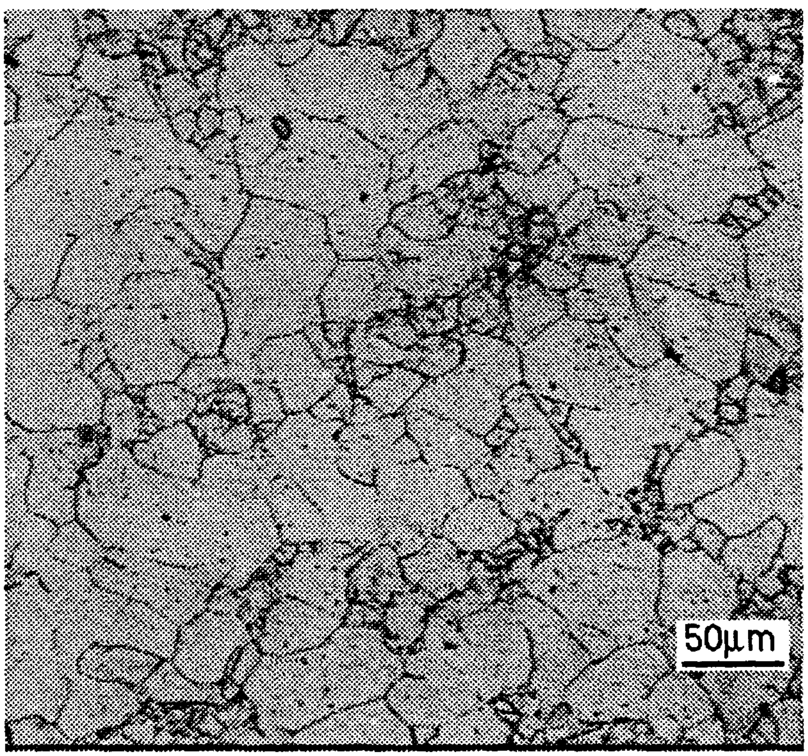

Figure 34. True stress-true strain curve and an optical micrograph from the center of the compressed sample cut through the compression axis, 1050 C and 0.001 s^{-1}.

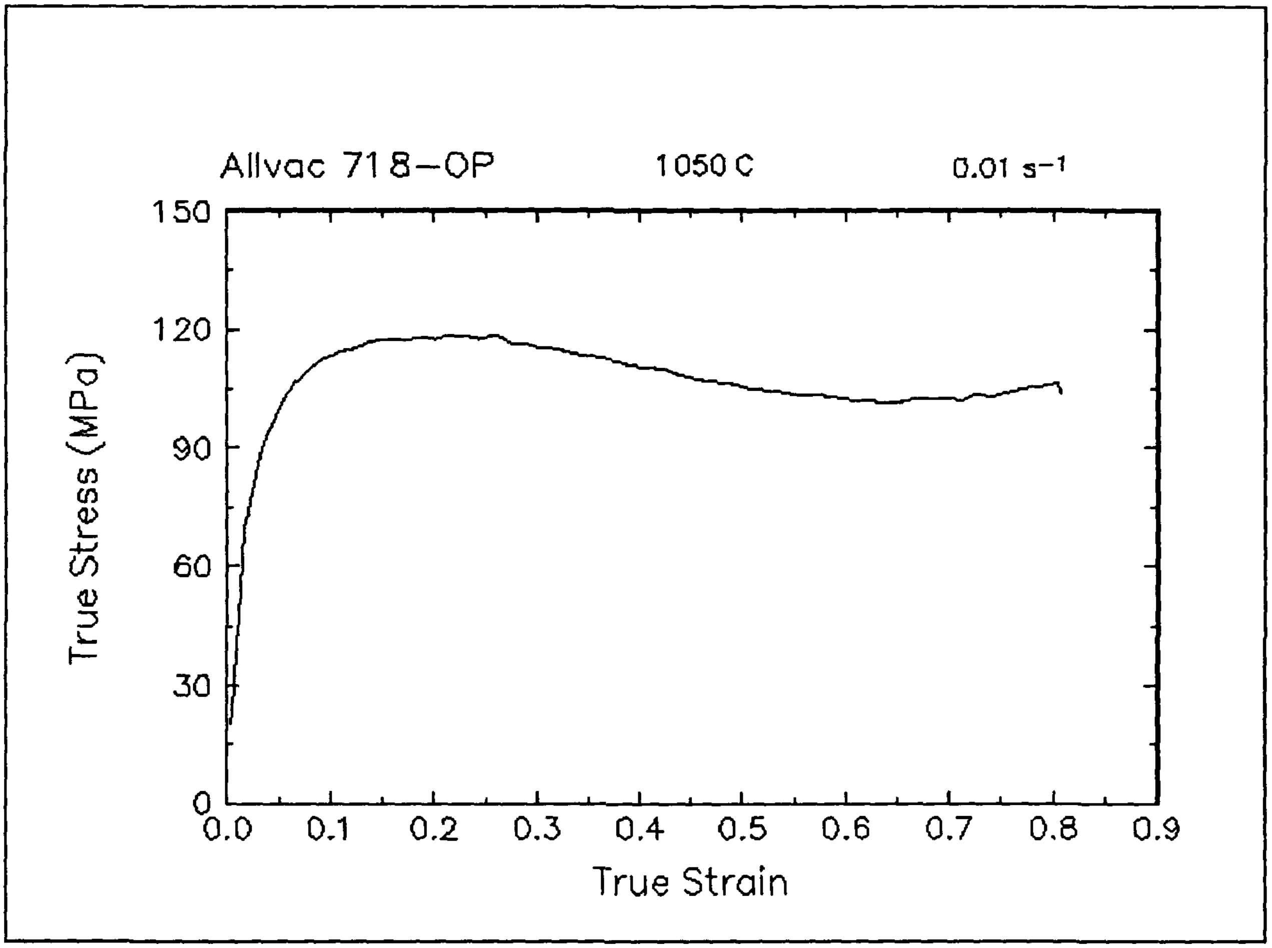

Figure 35. True stress-true strain curve, 1050 C and 0.01 s^{-1}.

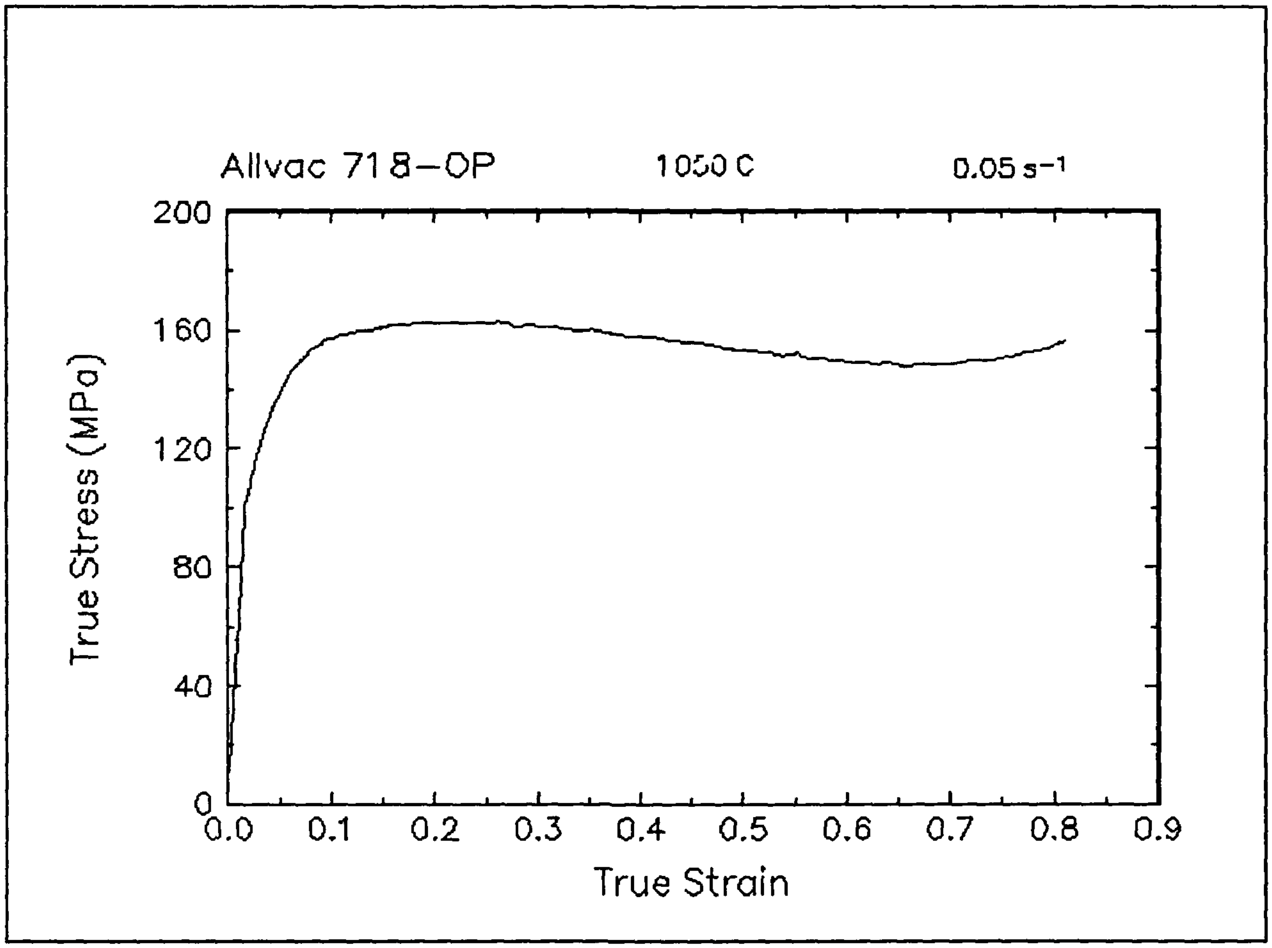

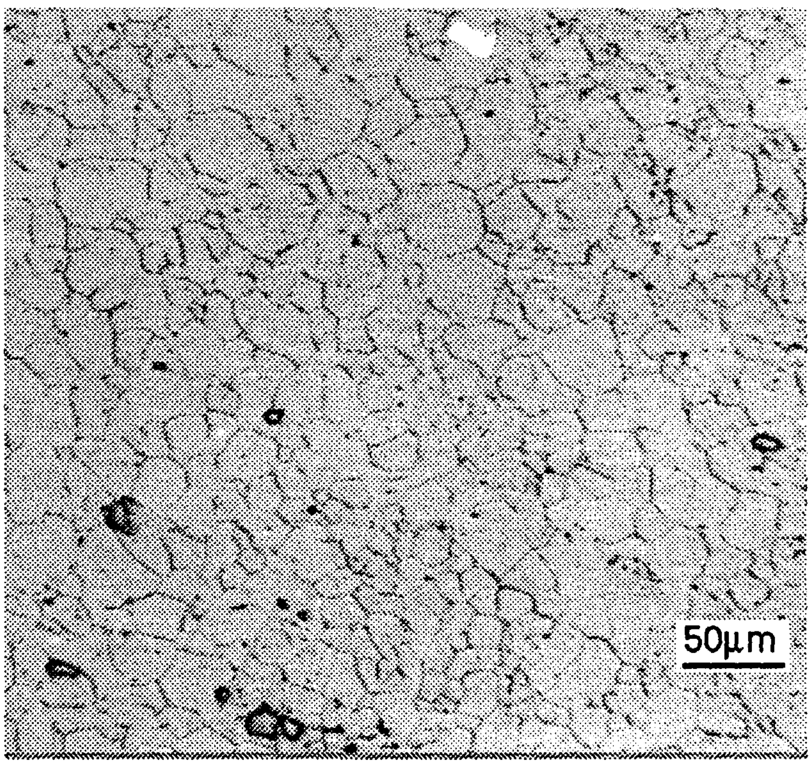

Figure 36. True stress-true strain curve and an optical micrograph from the center of the compressed sample cut through the compression axis, 1050 C and 0.05 s^{-1}.

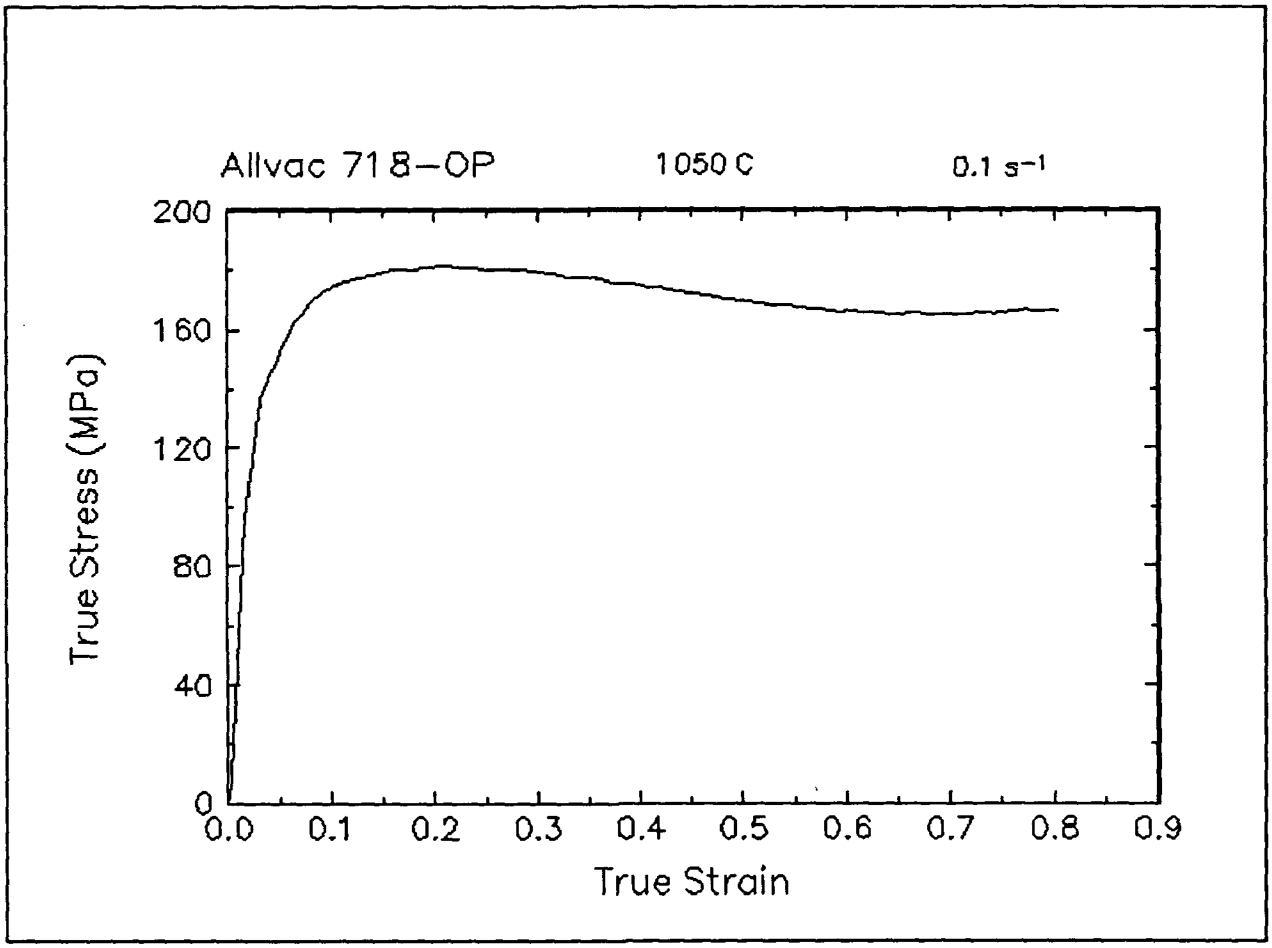

Figure 37. True stress-true strain curve, 1050 C and 0.1 s^{-1}.

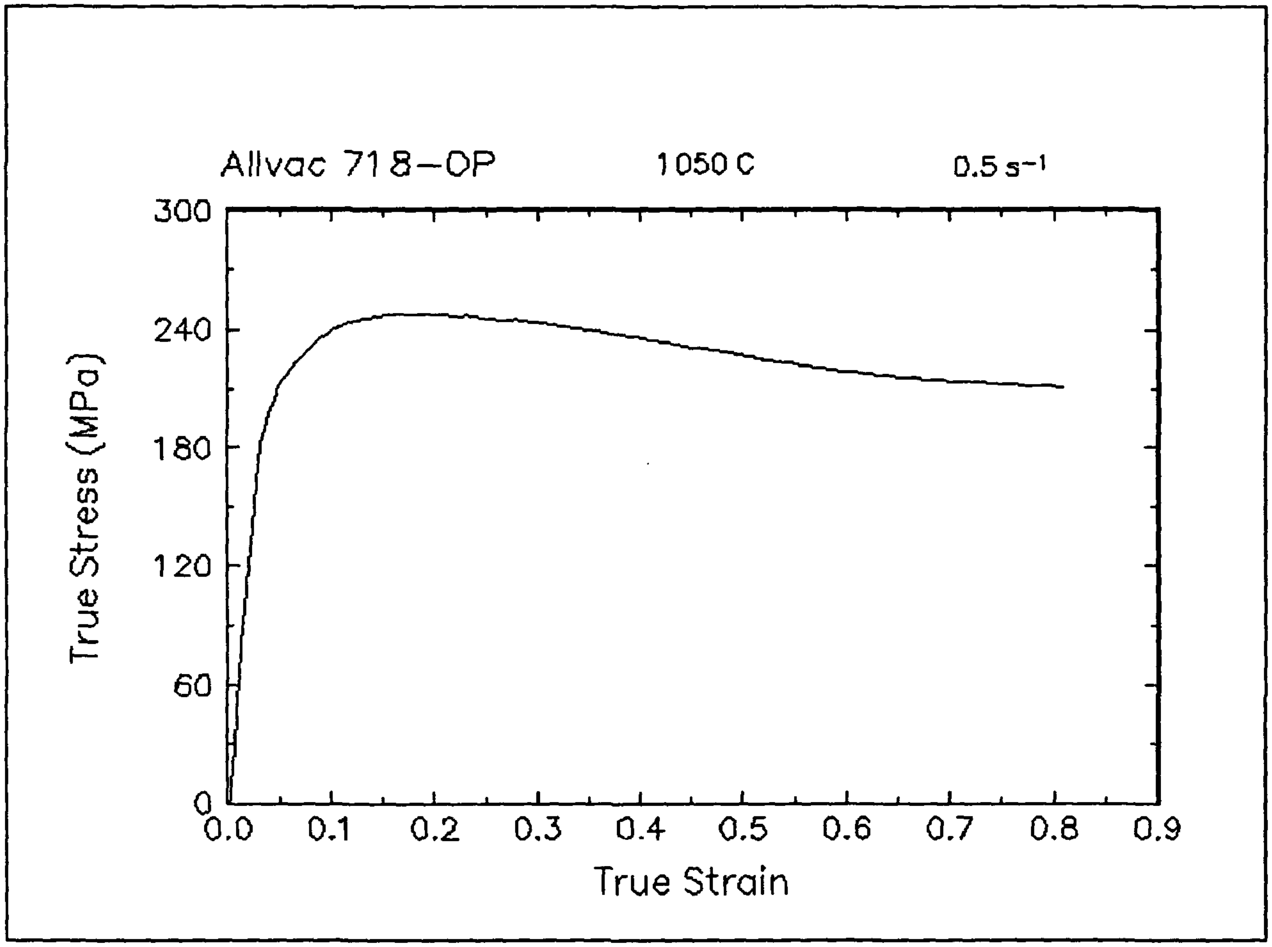

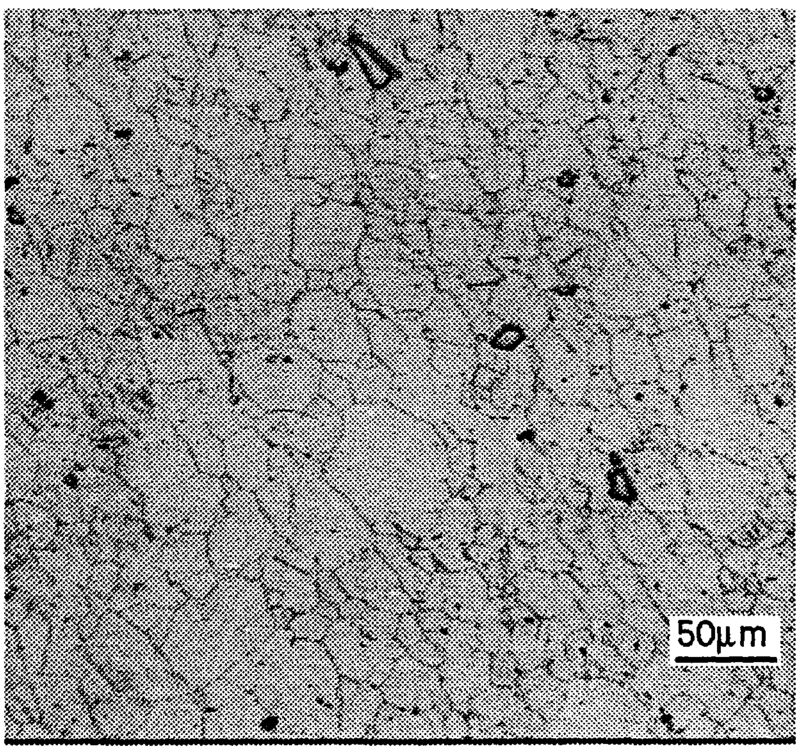

Figure 38. True stress-true strain curve and an optical micrograph from the center of the compressed sample cut through the compression axis, 1050 C and 0.5 s^{-1}.

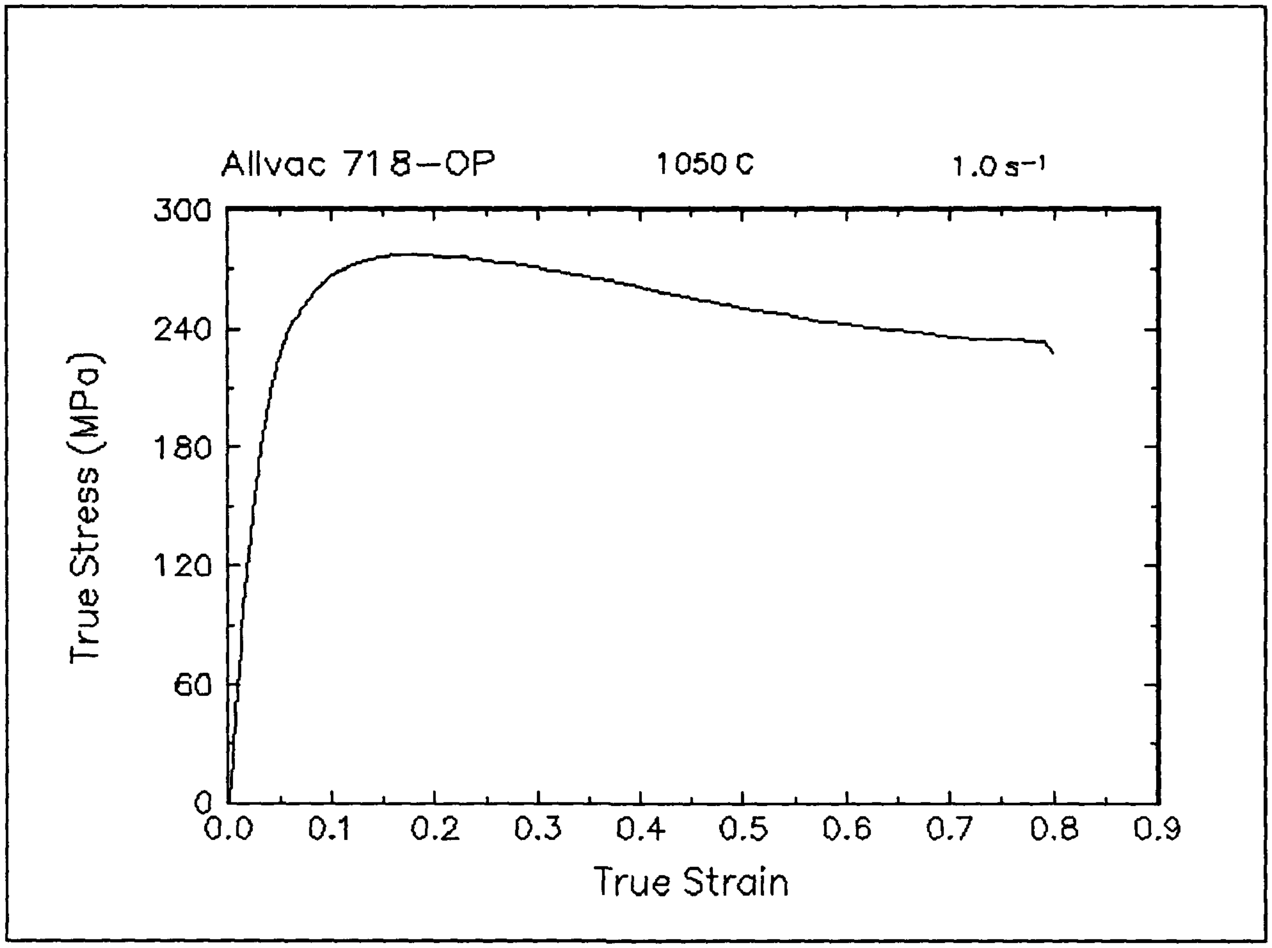

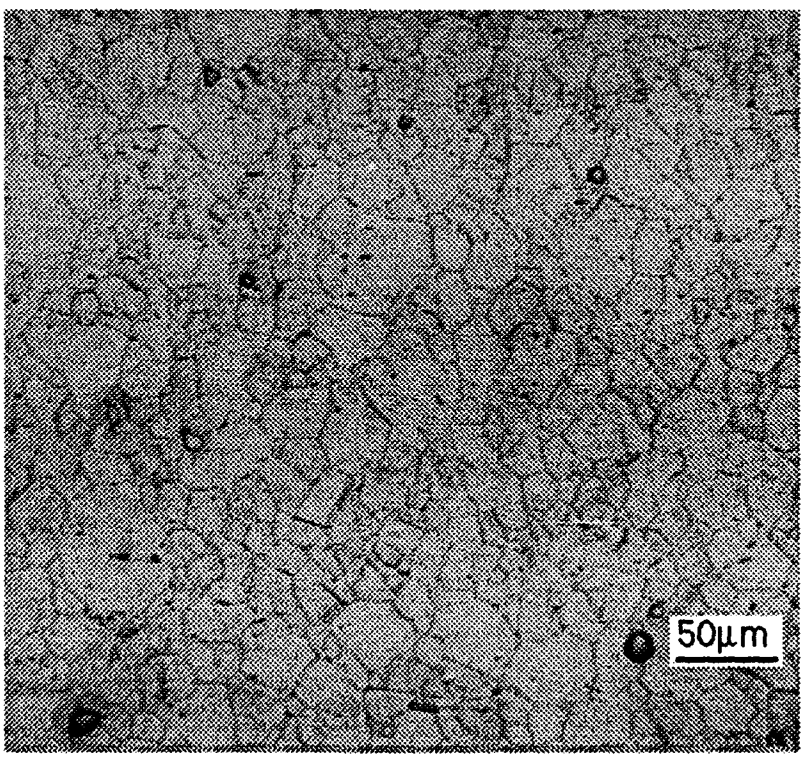

Figure 39. True stress-true strain curve and an optical micrograph from the center of the compressed sample cut through the compression axis, 1050 C and 1 s^{-1}.

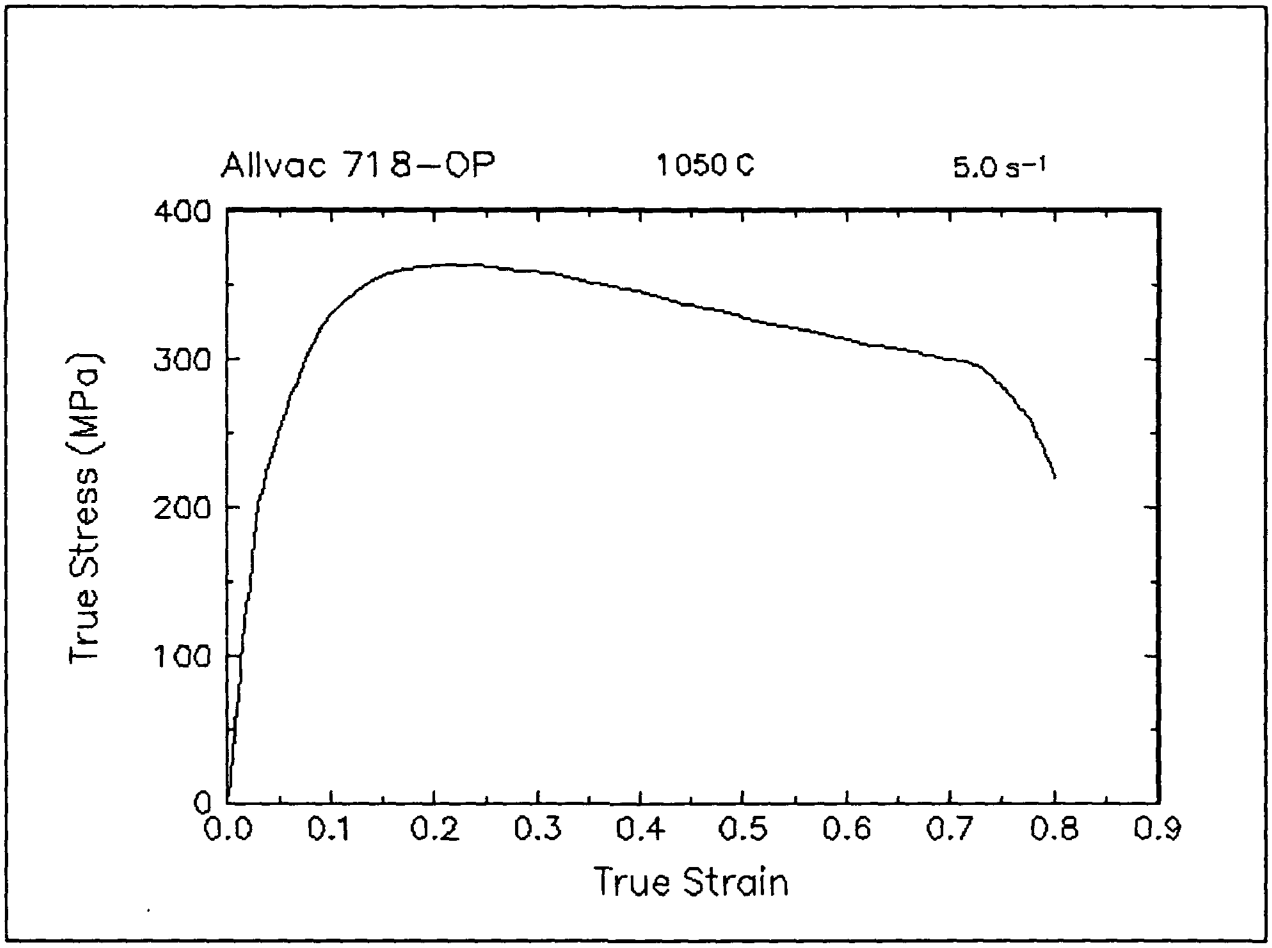

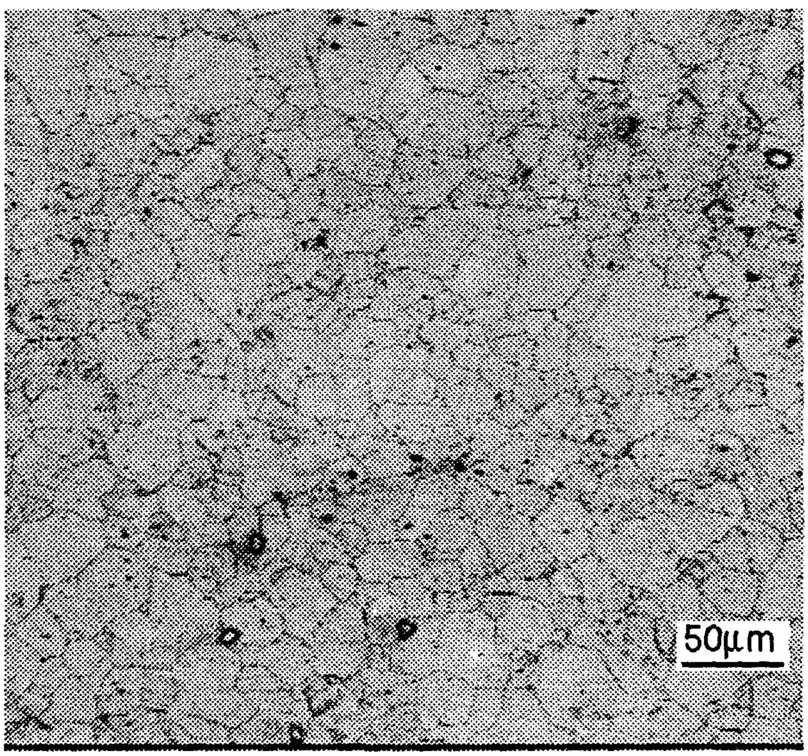

Figure 40. True stress-true strain curve and an optical micrograph from the center of the compressed sample cut through the compression axis, 1050 C and 5 s^{-1}.

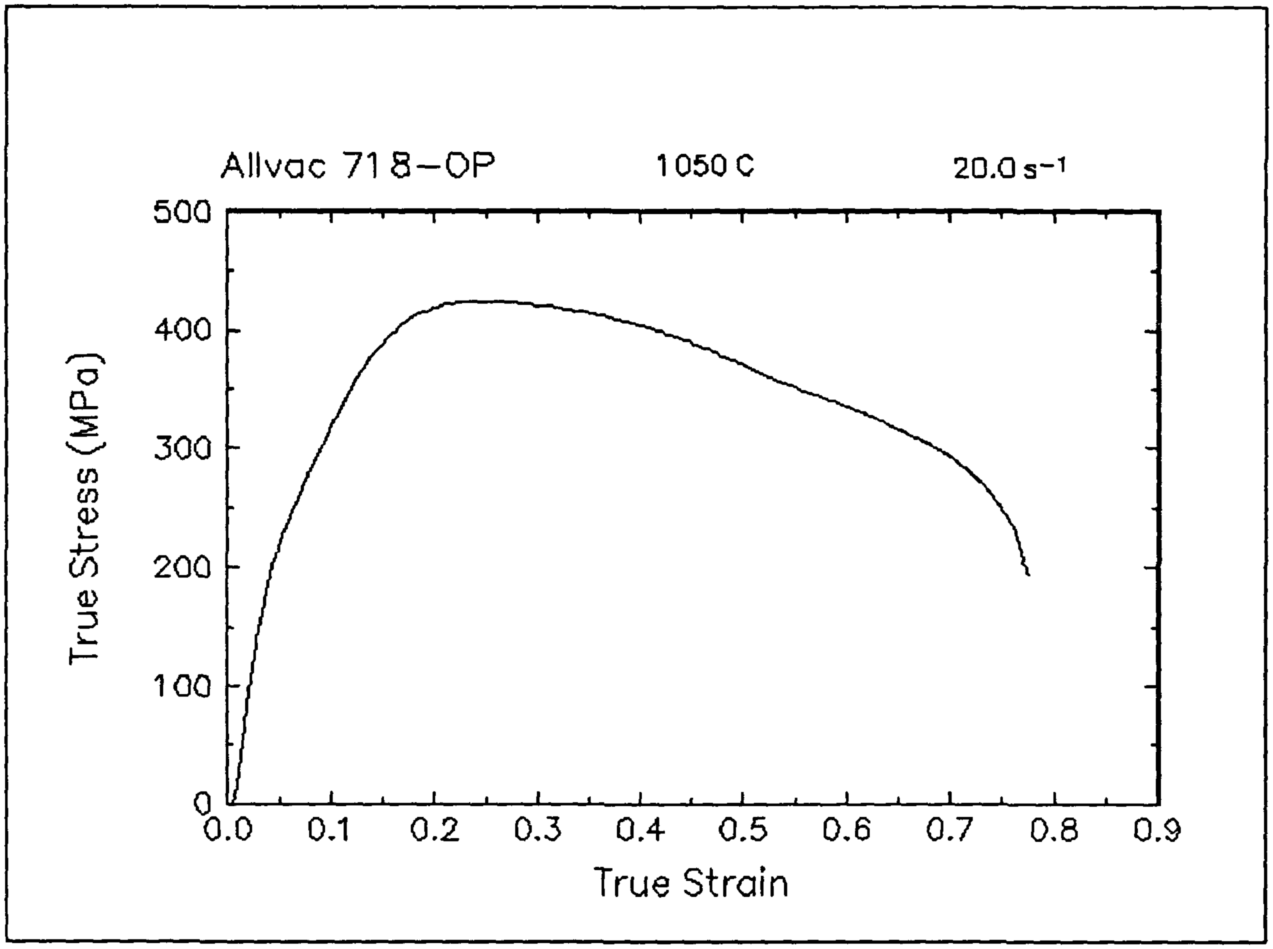

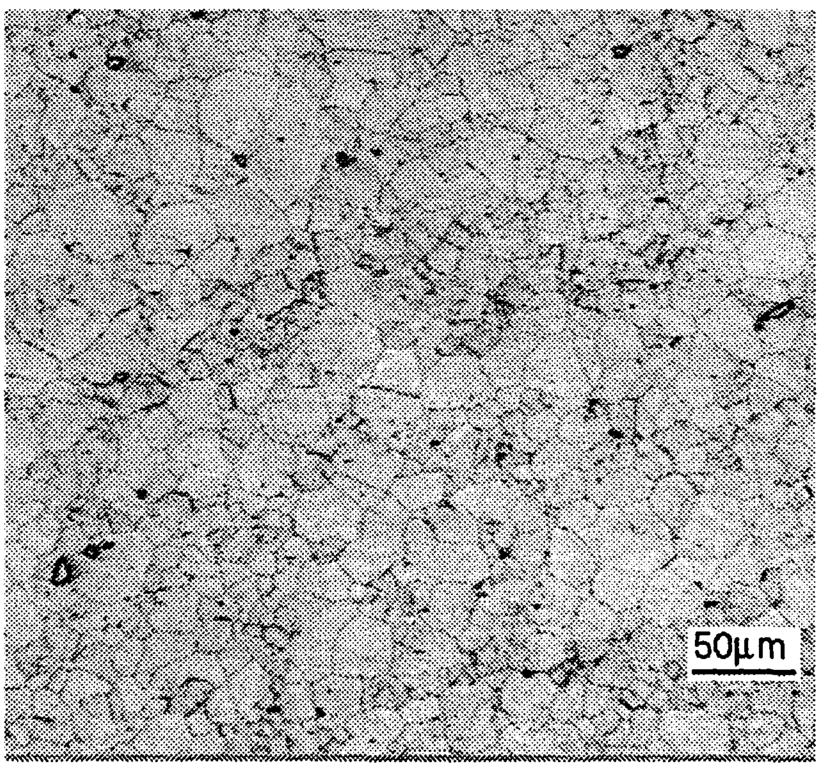

Figure 41. True stress-true strain curve and an optical micrograph from the center of the compressed sample cut through the compression axis, 1050 C and 20 s^{-1}.

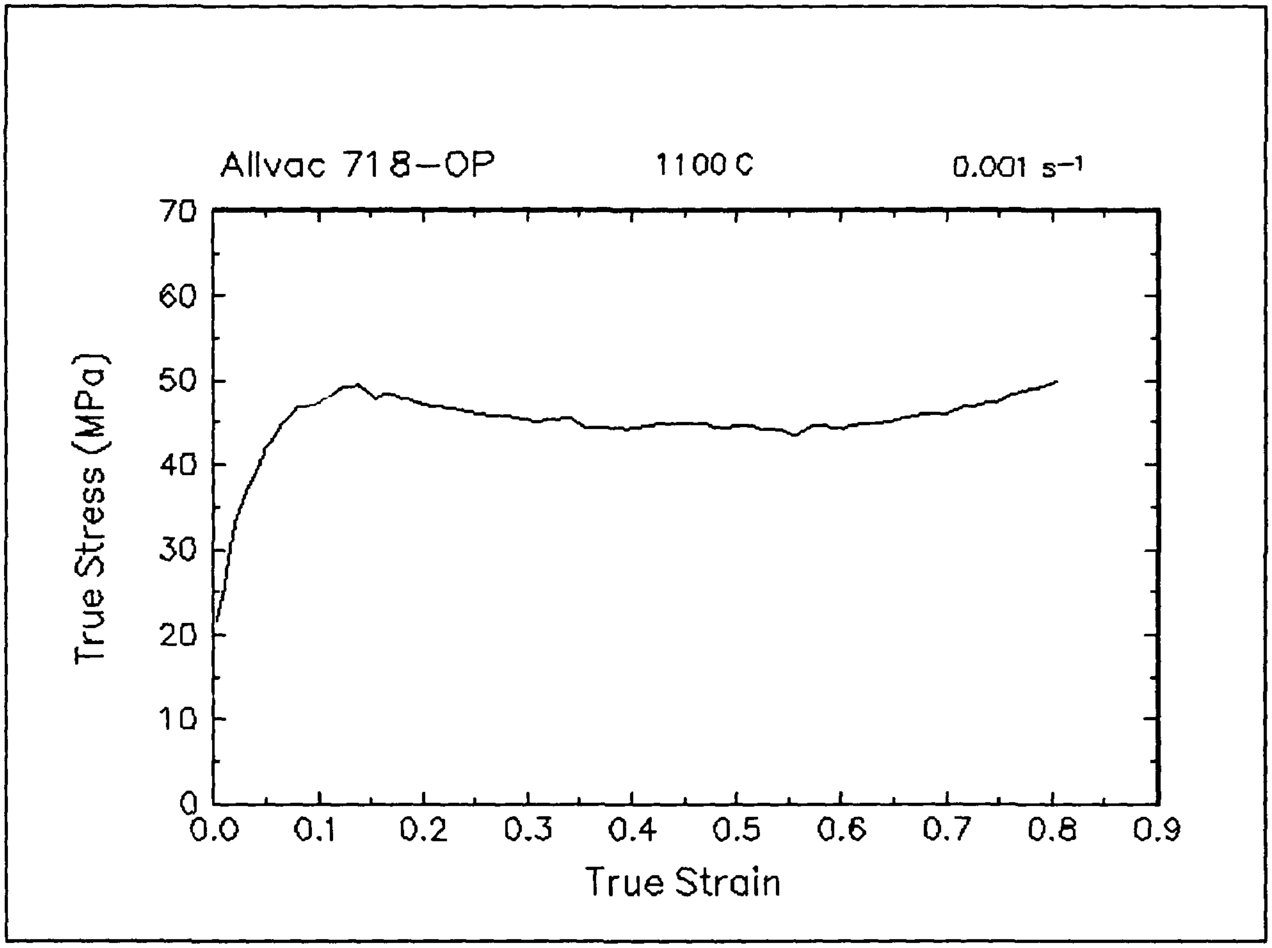

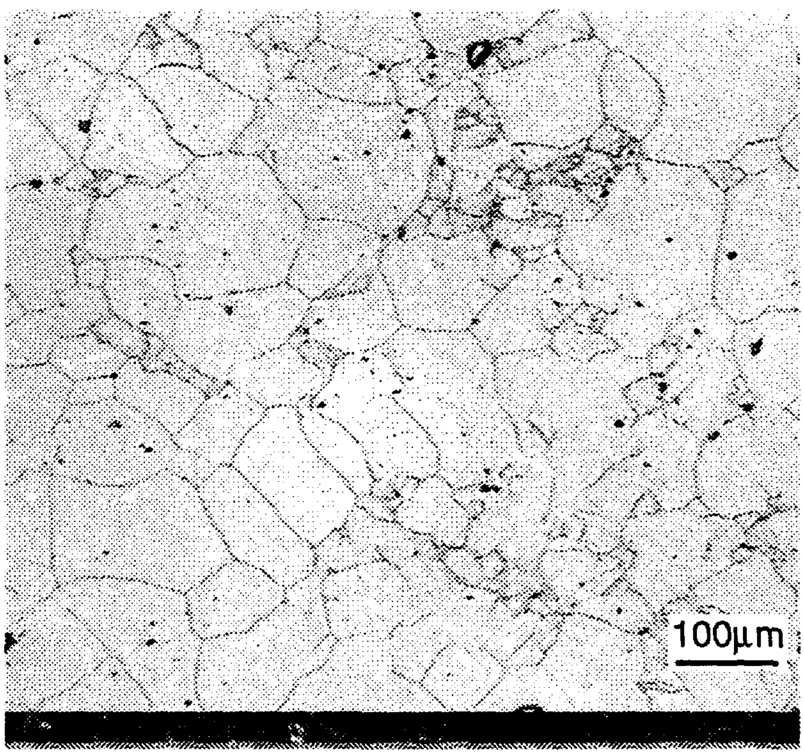

Figure 42. True stress-true strain curve and an optical micrograph from the center of the compressed sample cut through the compression axis, 1100 C and 0.001 s^{-1}.

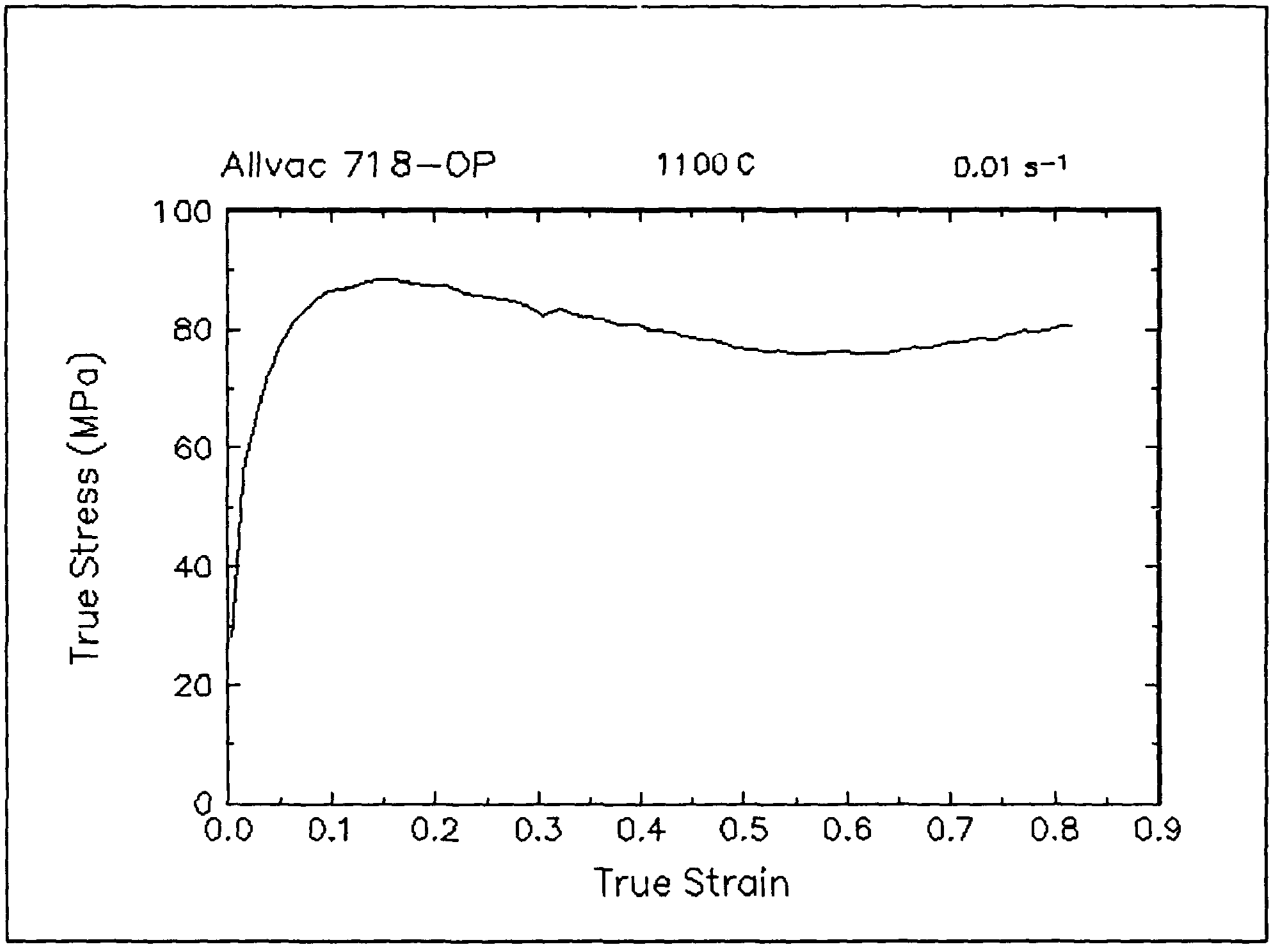

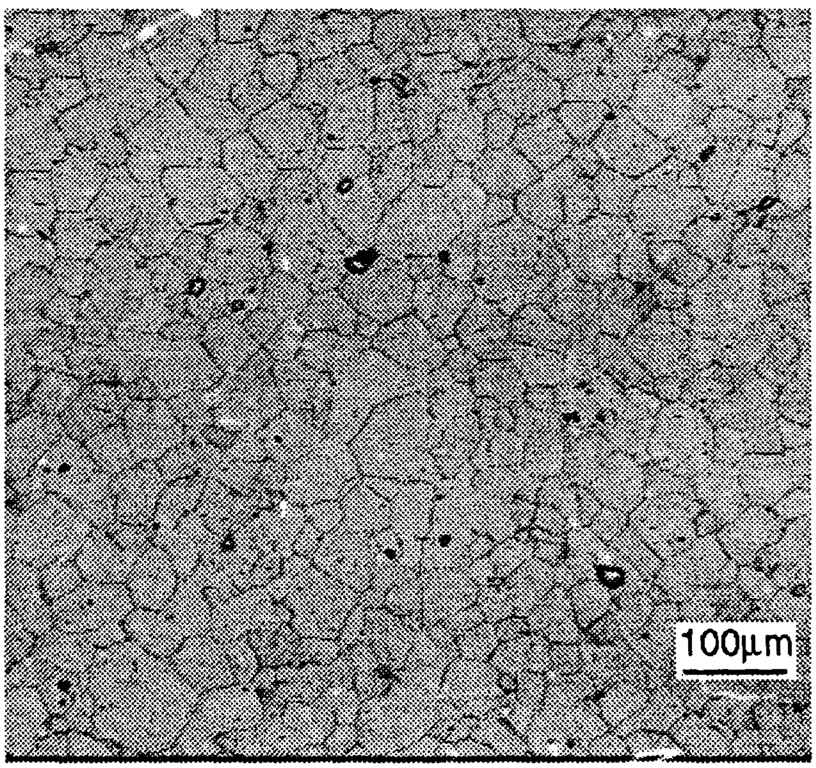

Figure 43. True stress-true strain curve and an optical micrograph from the center of the compressed sample cut through the compression axis, 1100 C and 0.01 s^{-1}.

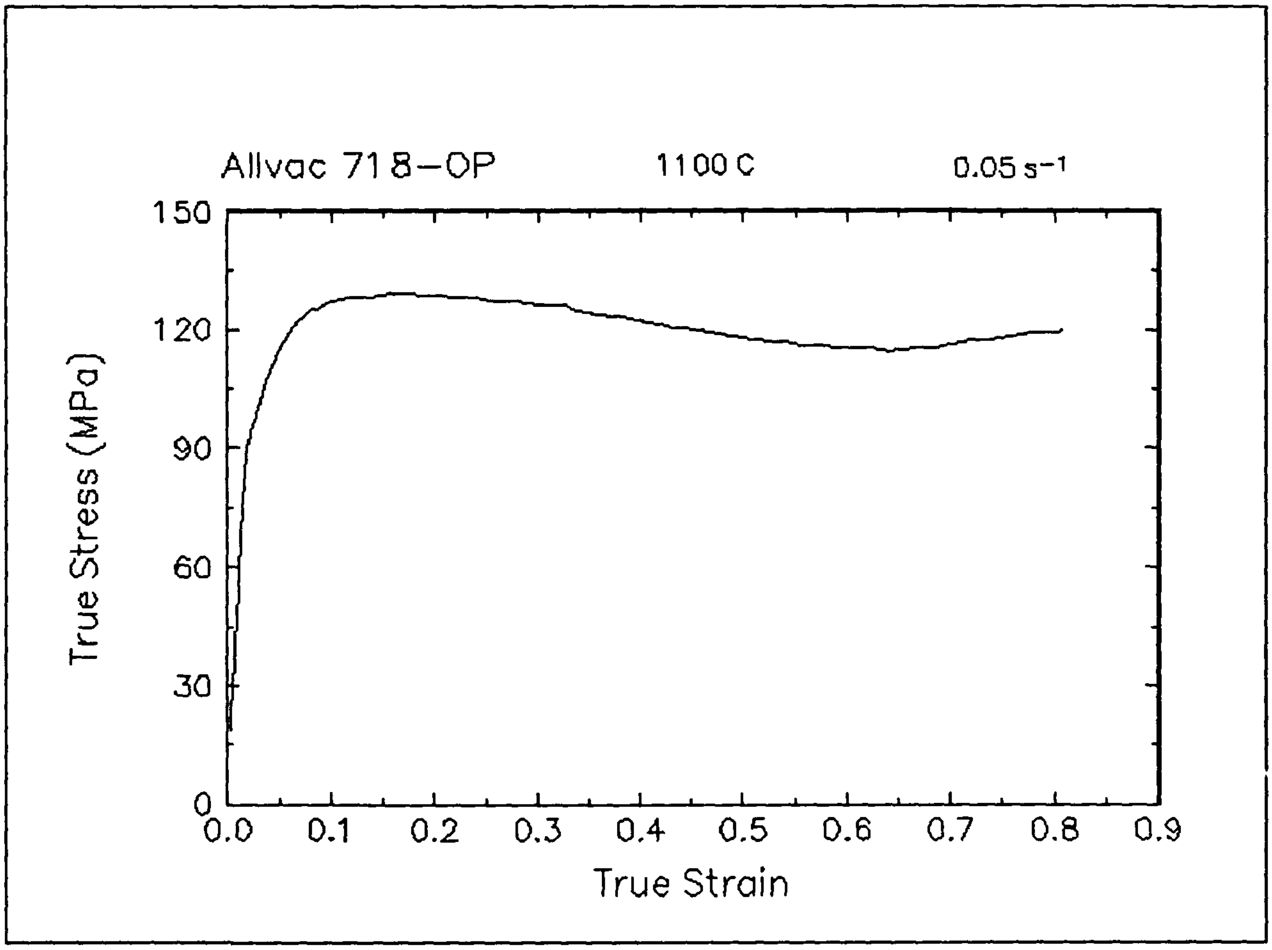

Figure 44. True stress-true strain curve, 1100 C and 0.05 s^{-1}.

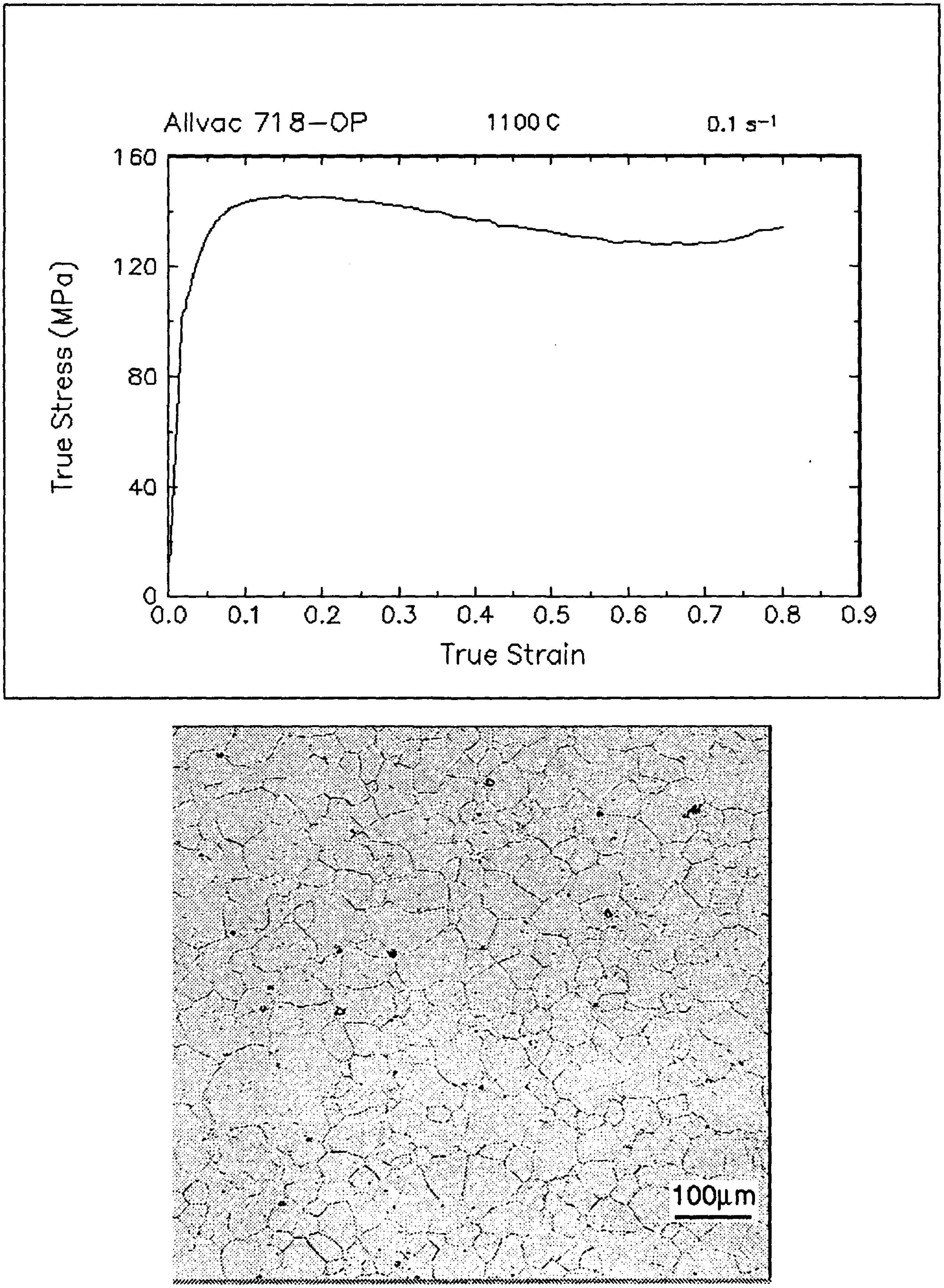

Figure 45. True stress-true strain curve and an optical micrograph from the center of the compressed sample cut through the compression axis, 1100 C and 0.1 s^{-1}.

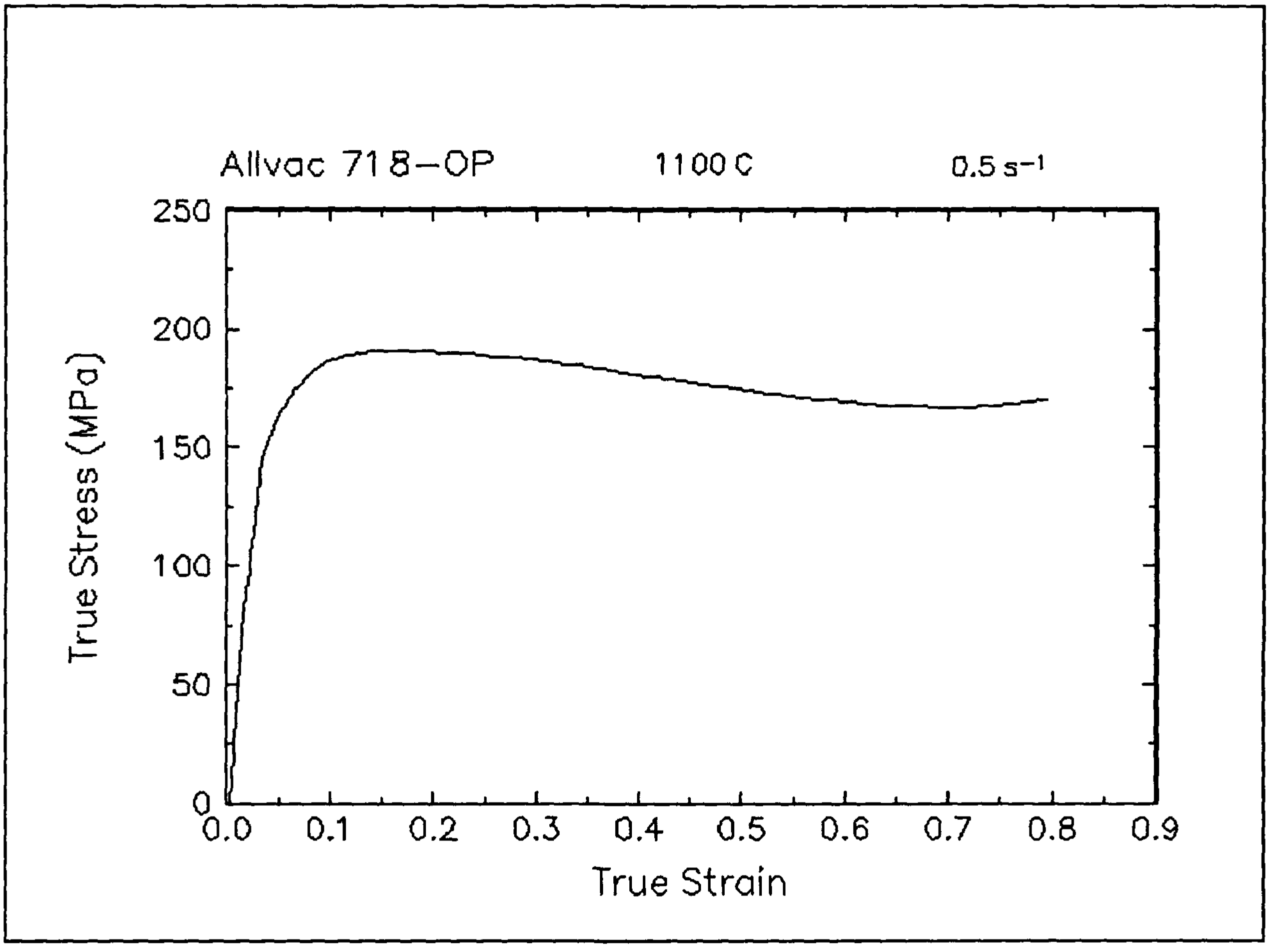

Figure 46. True stress-true strain curve, 1100 C and 0.5 s^{-1}.

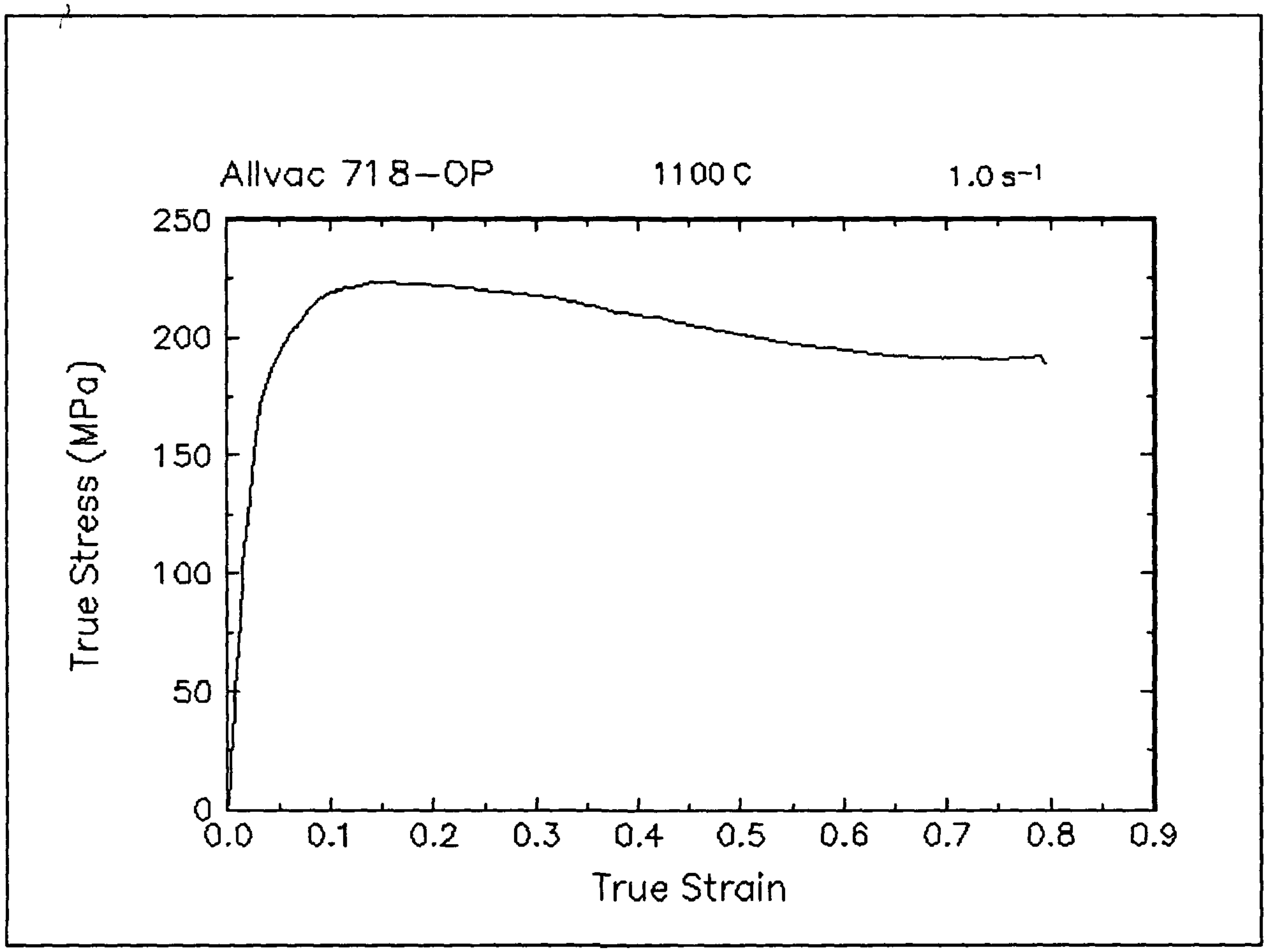

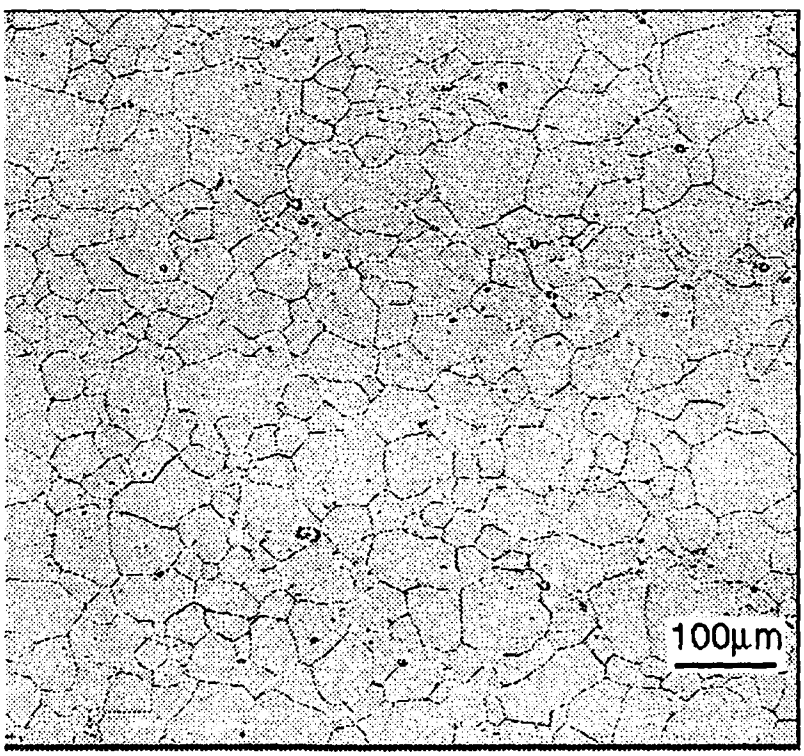

Figure 47. True stress-true strain curve and an optical micrograph from the center of the compressed sample cut through the compression axis, 1100 C and 1 s^{-1}.

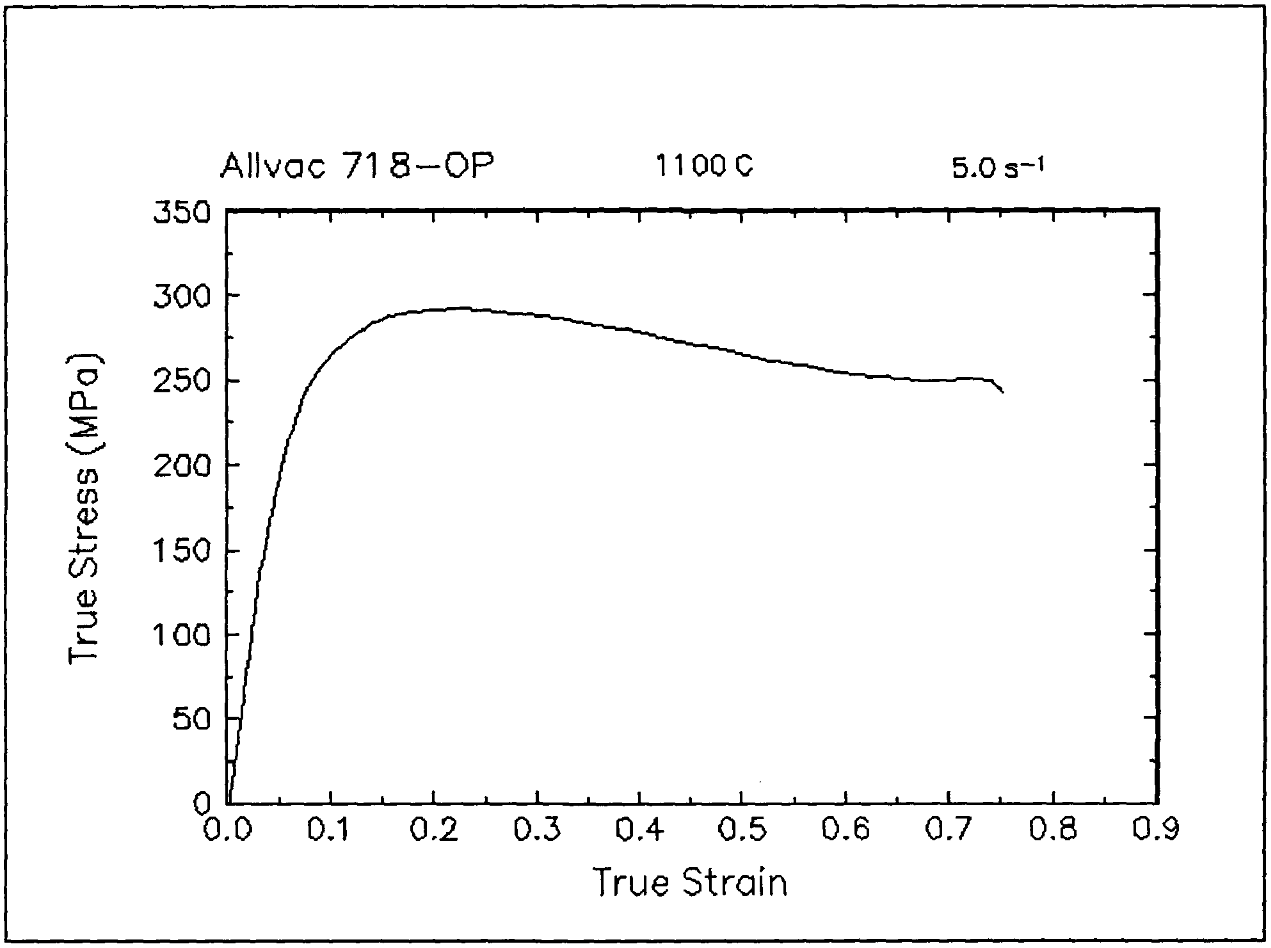

Figure 48. True stress-true strain curve, 1100 C and 5 s^{-1}.

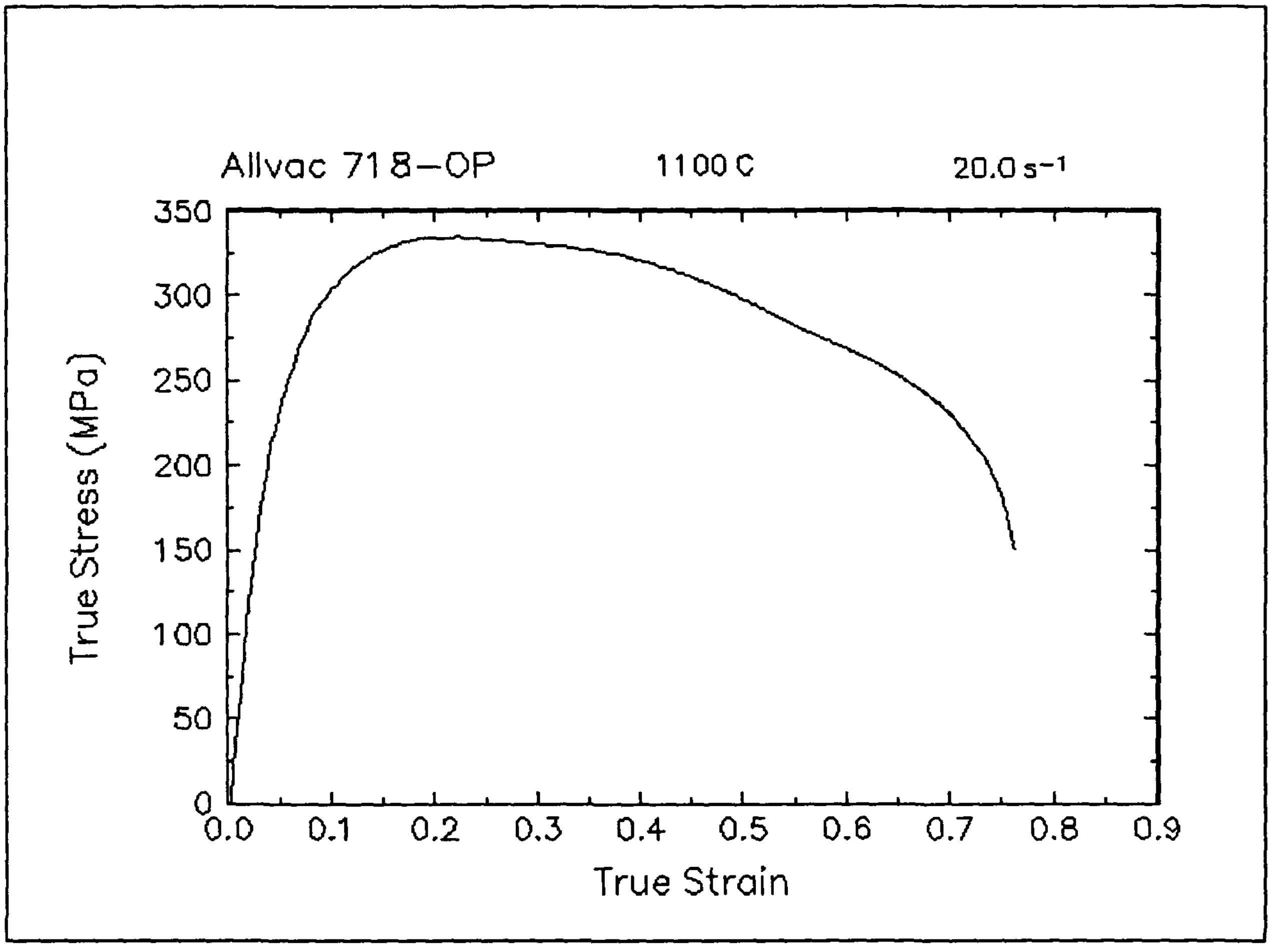

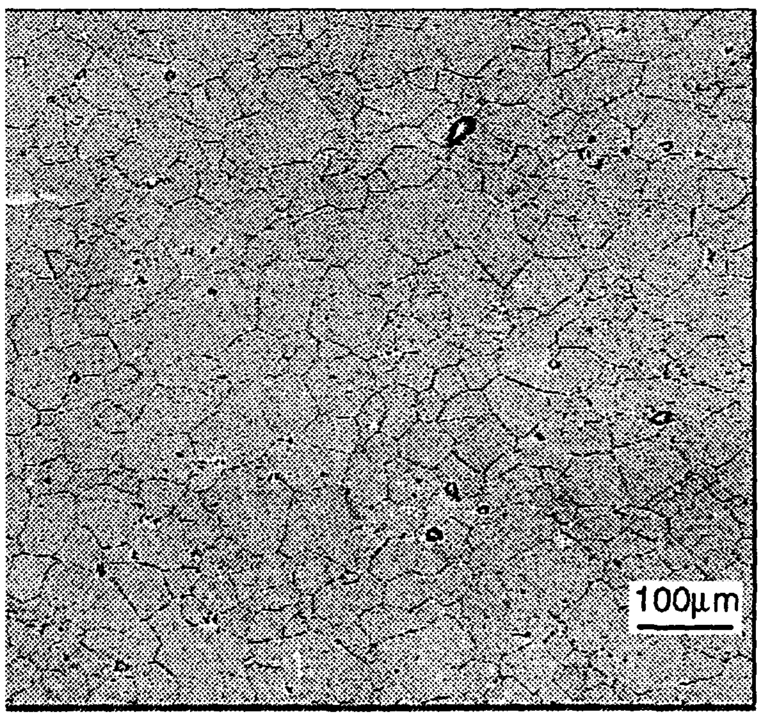

Figure 49. True stress-true strain curve and an optical micrograph from the center of the compressed sample cut through the compression axis, 1100 C and 20 s^{-1}.

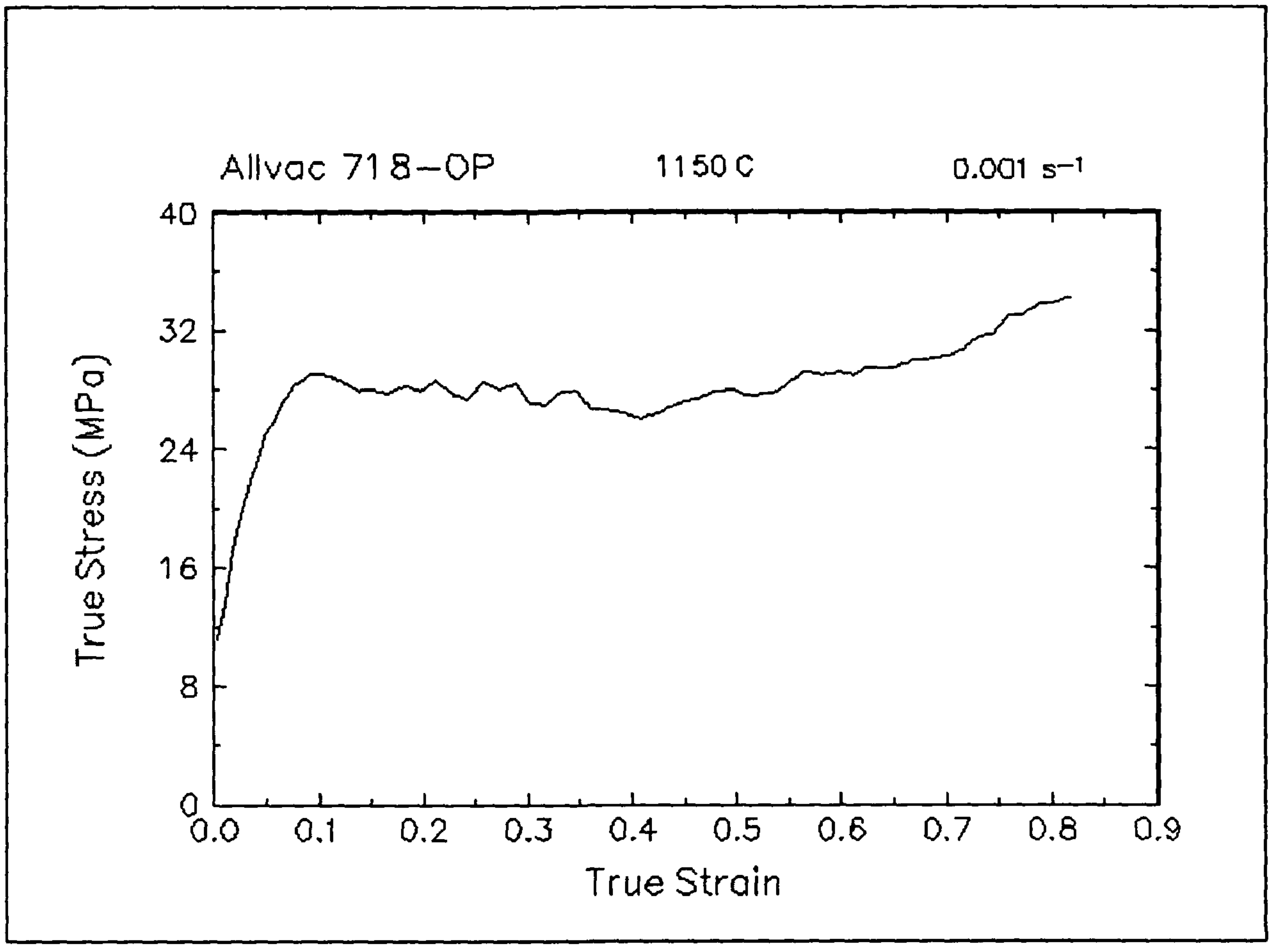

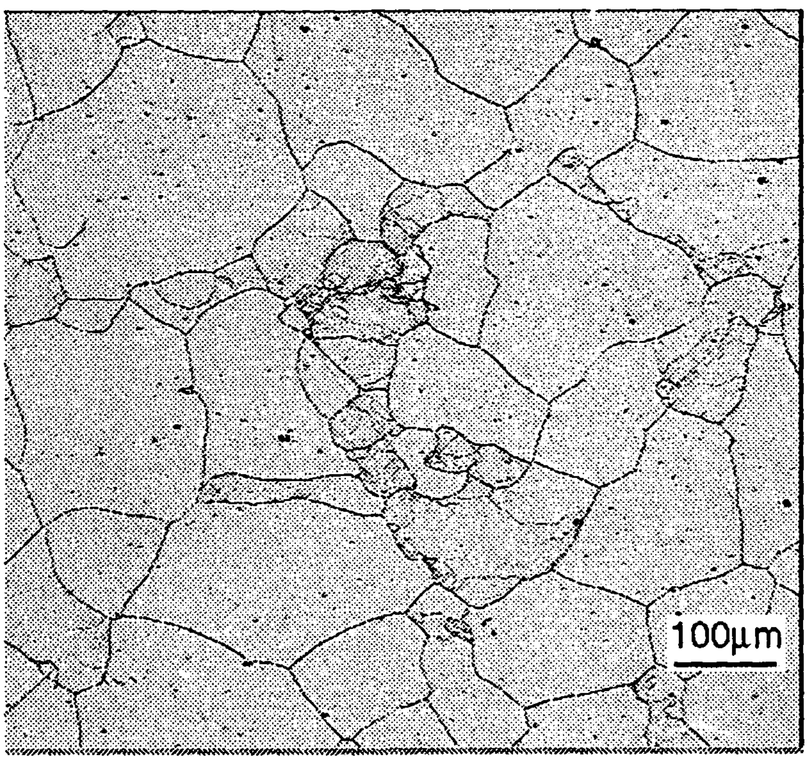

Figure 50. True stress-true strain curve and an optical micrograph from the center of the compressed sample cut through the compression axis, 1150 C and 0.001 s^{-1}.

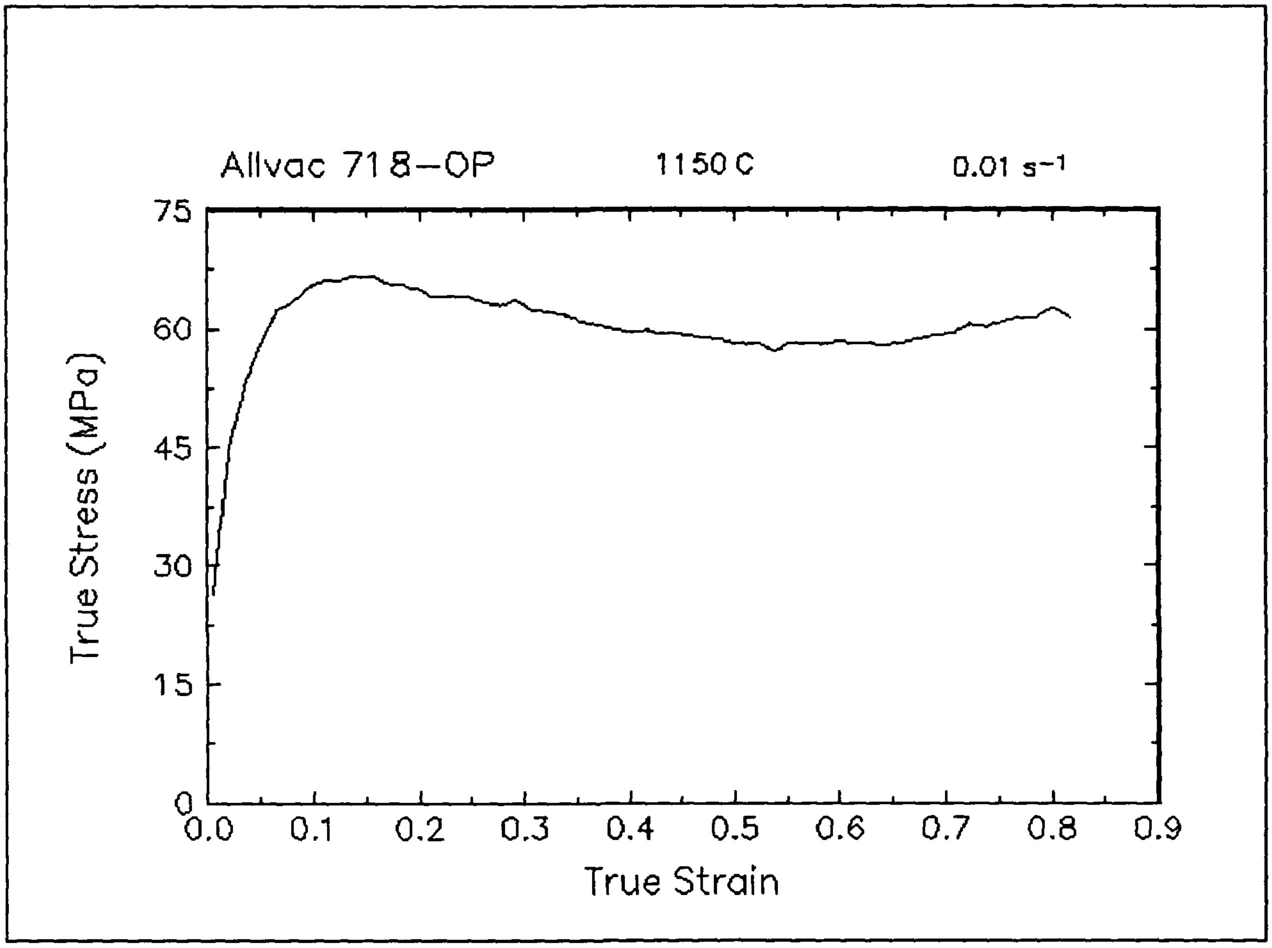

Figure 51. True stress-true strain curve, 1150 C and 0.01 s^{-1}.

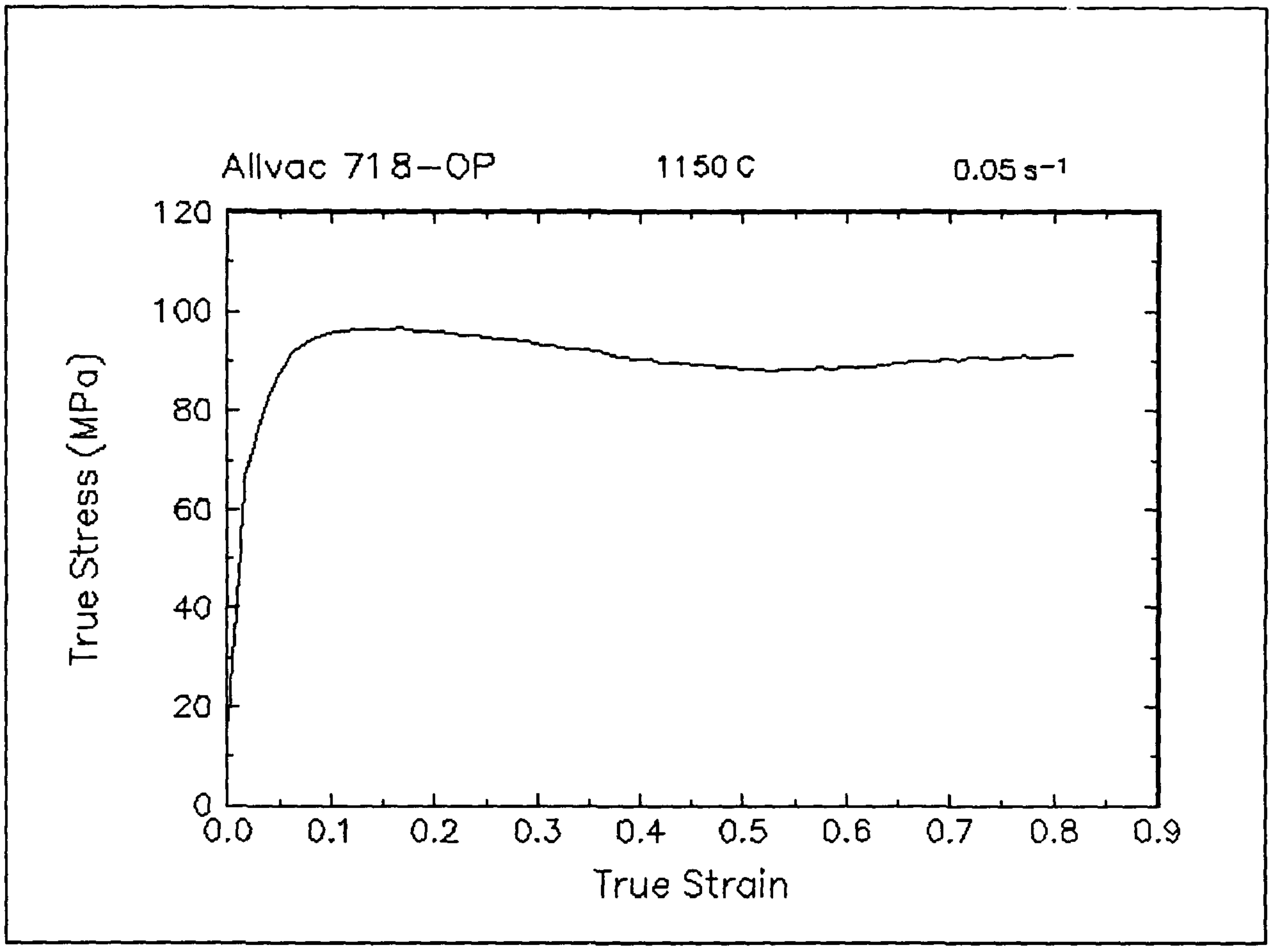

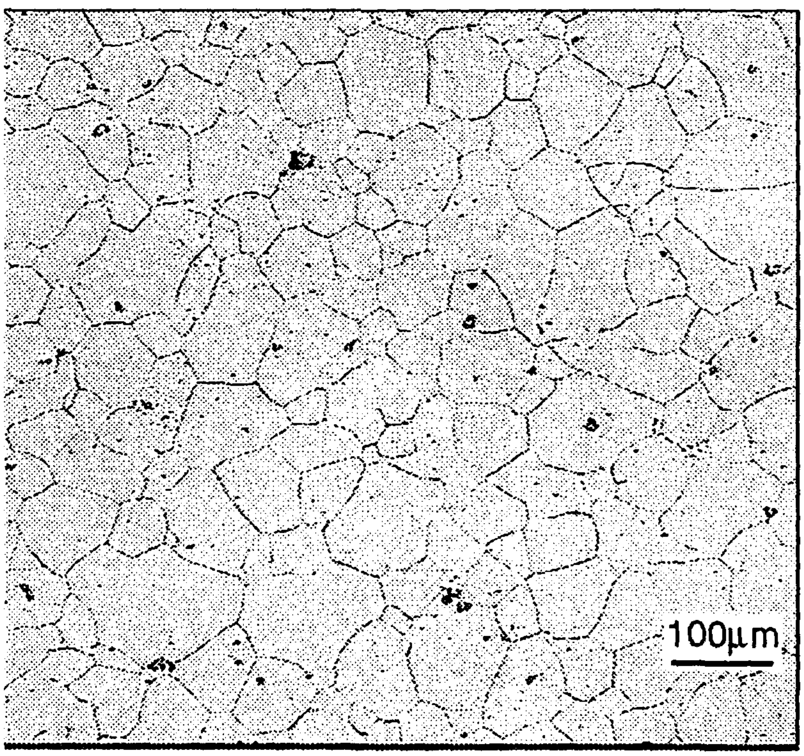

Figure 52. True stress-true strain curve and an optical micrograph from the center of the compressed sample cut through the compression axis, 1150 C and 0.05 s^{-1}.

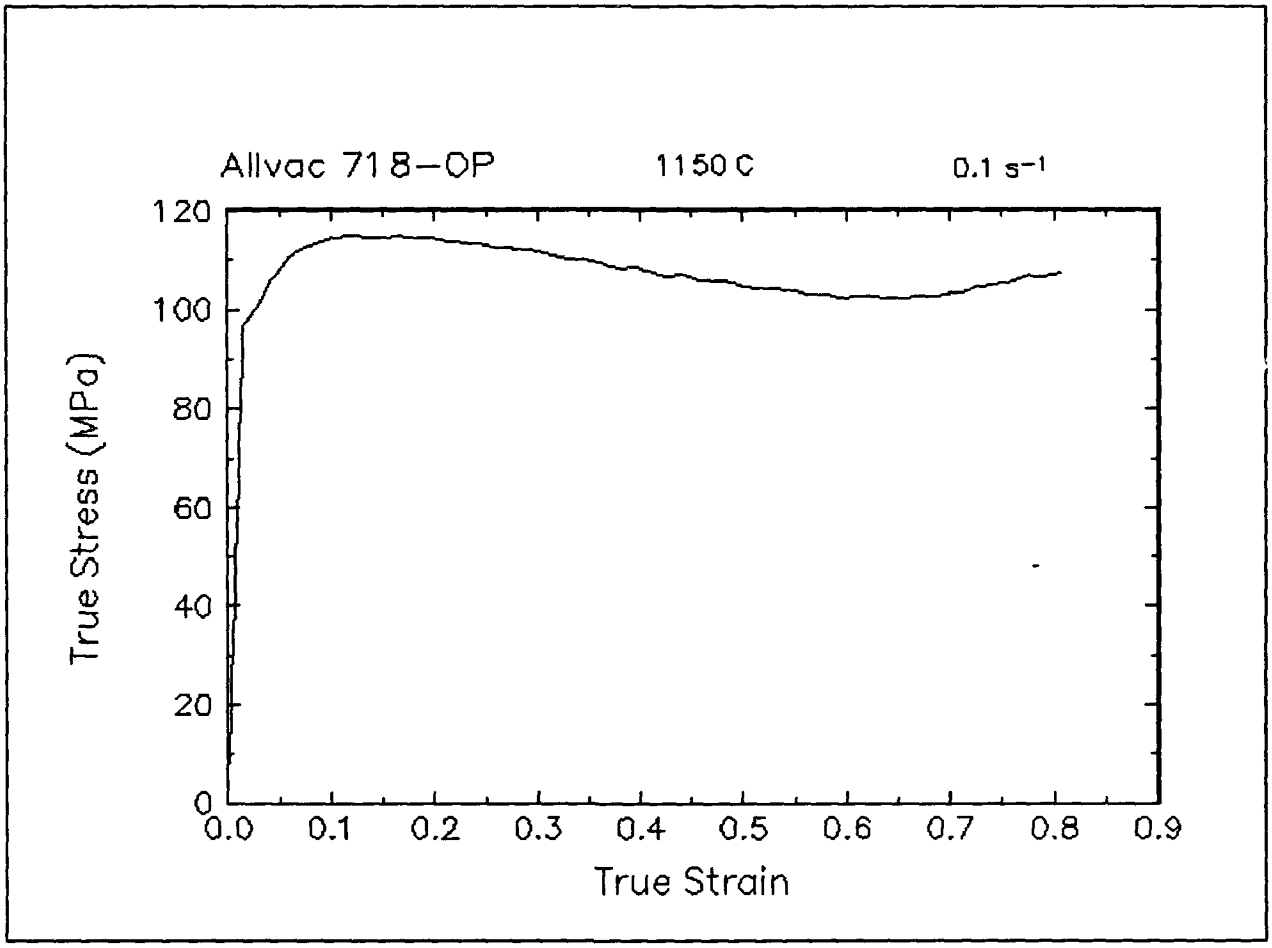

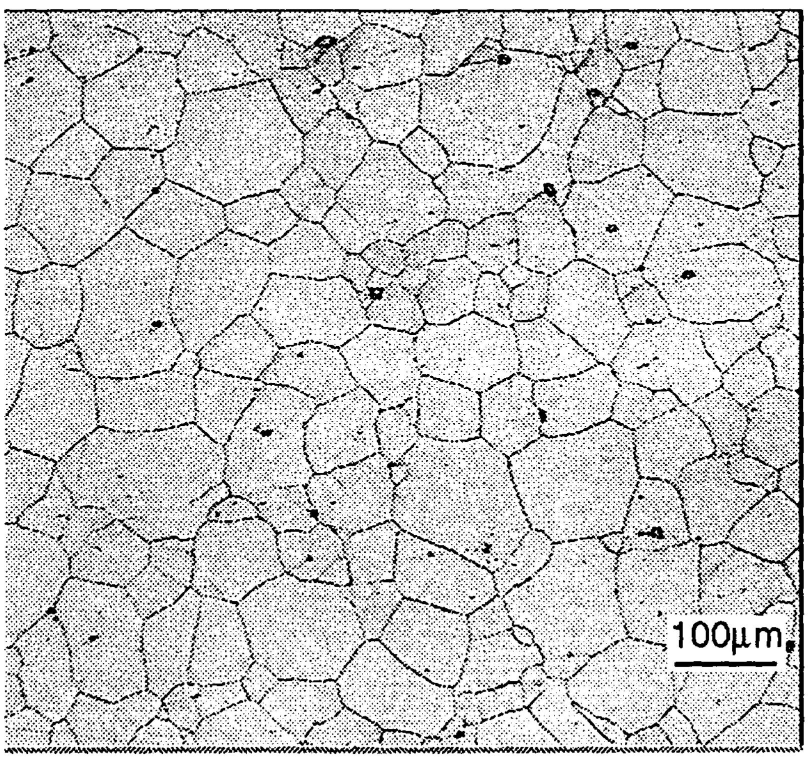

Figure 53. True stress-true strain curve and an optical micrograph from the center of the compressed sample cut through the compression axis, 1150 C and 0.1 s^{-1}.

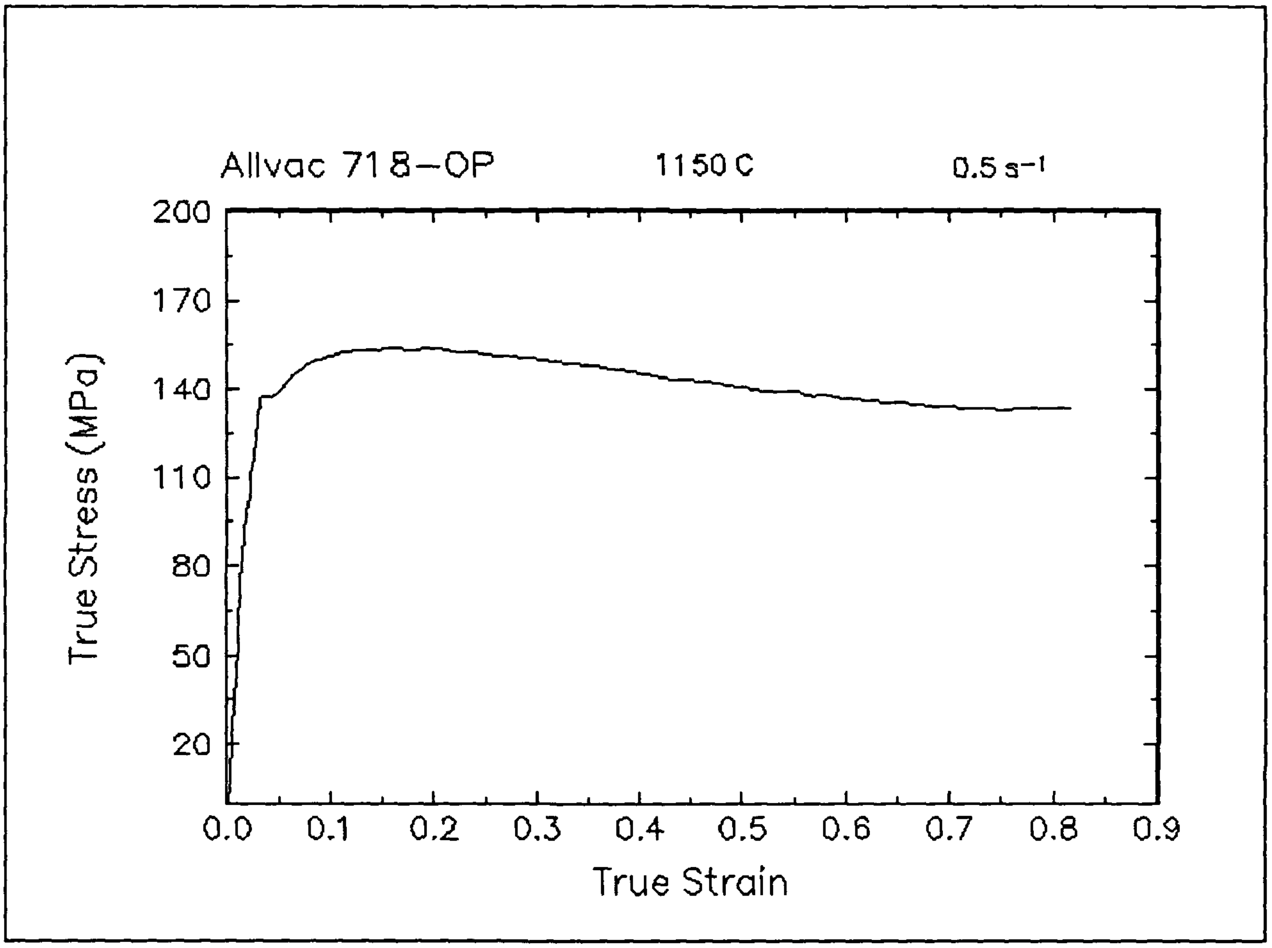

Figure 54. True stress-true strain curve, 1150 C and 0.5 s^{-1}.

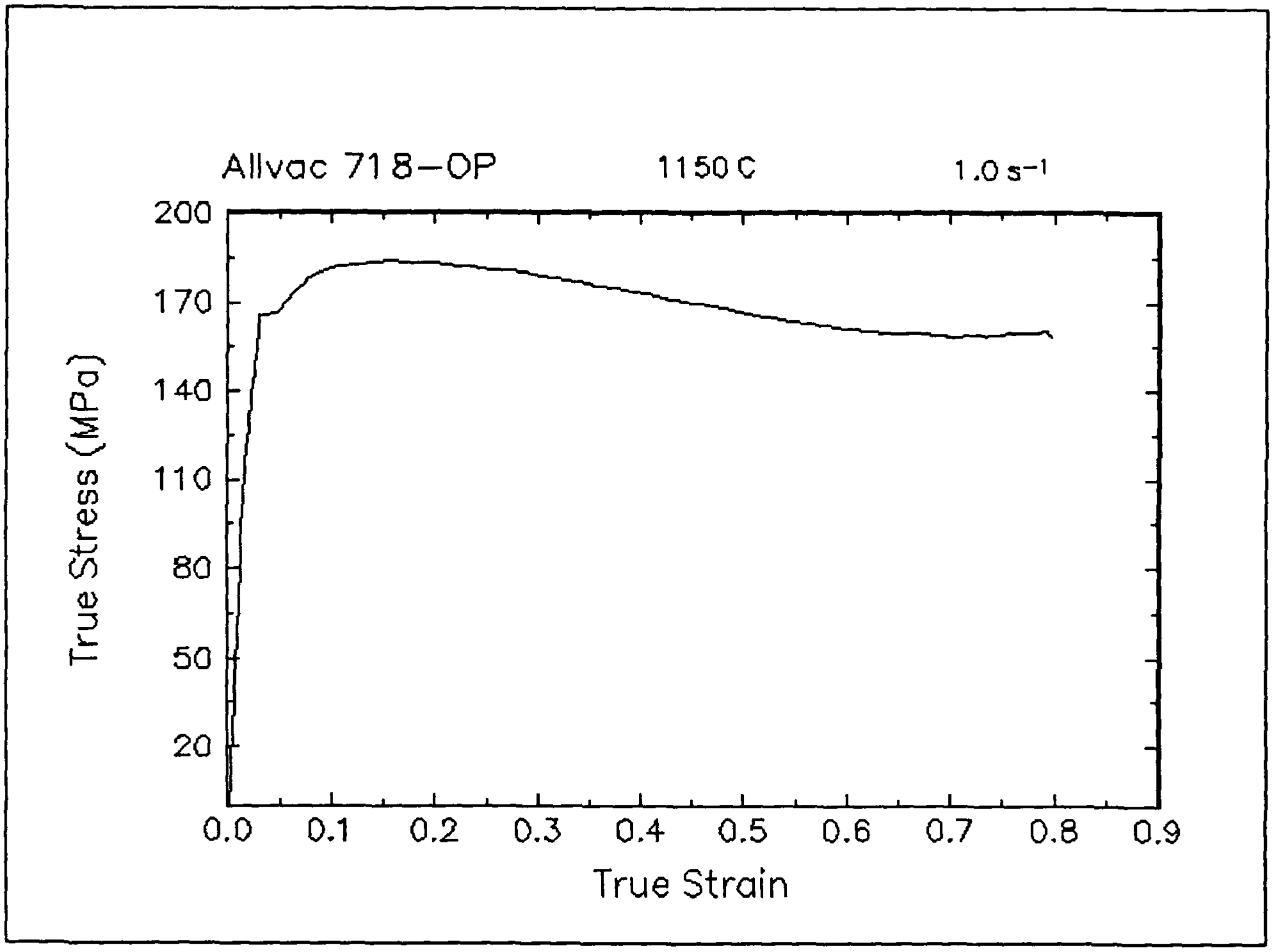

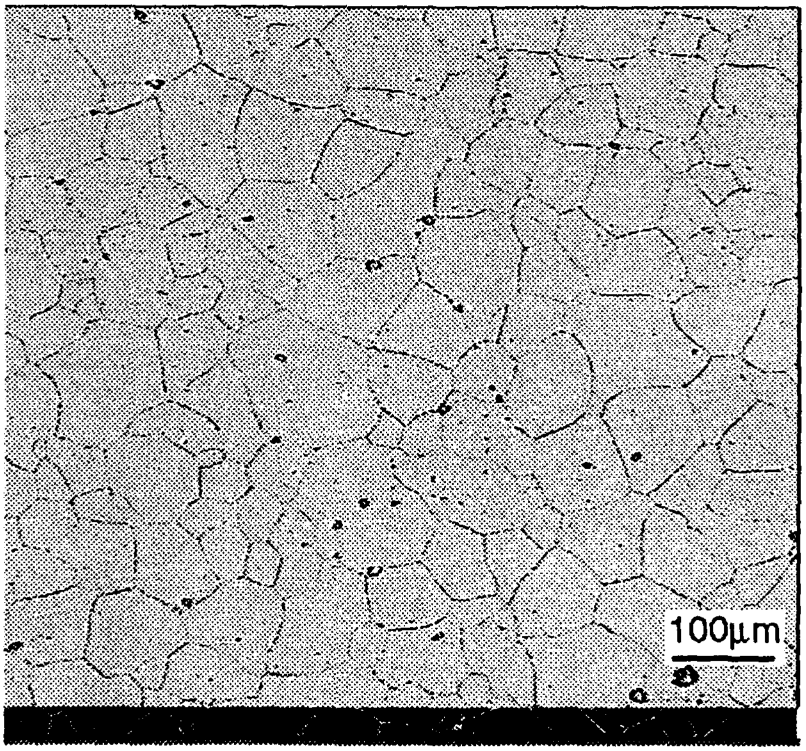

Figure 55. True stress-true strain curve and an optical micrograph from the center of the compressed sample cut through the compression axis, 1150 C and 1 s^{-1}.

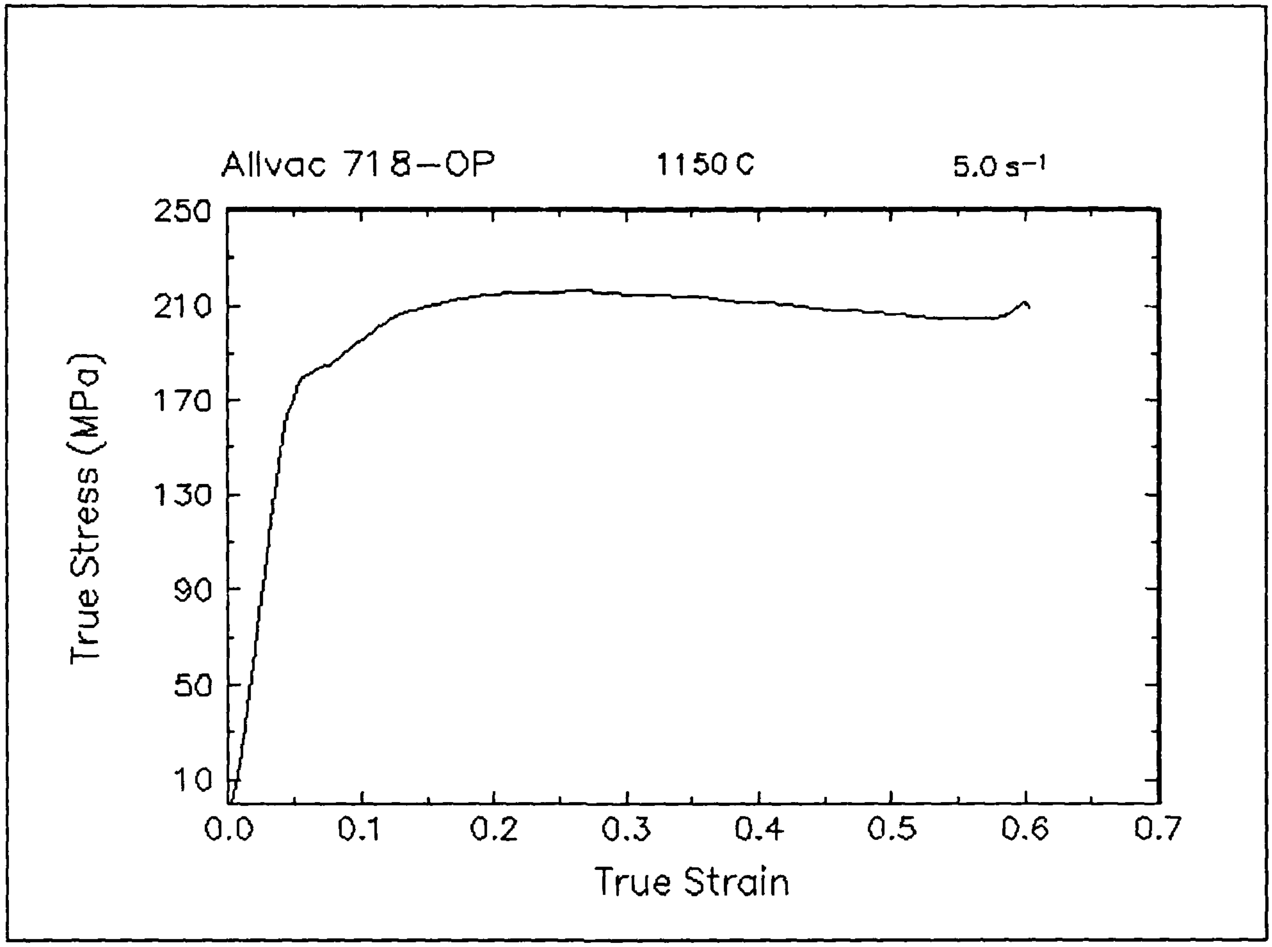

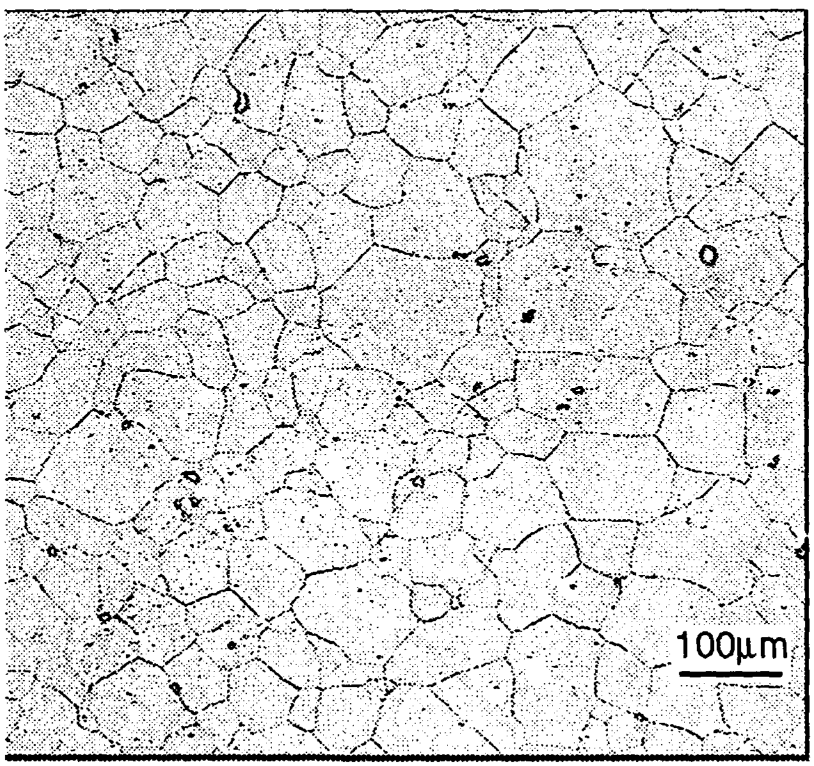

Figure 56. True stress-true strain curve and an optical micrograph from the center of the compressed sample cut through the compression axis, 1150 C and 5 s^{-1}.

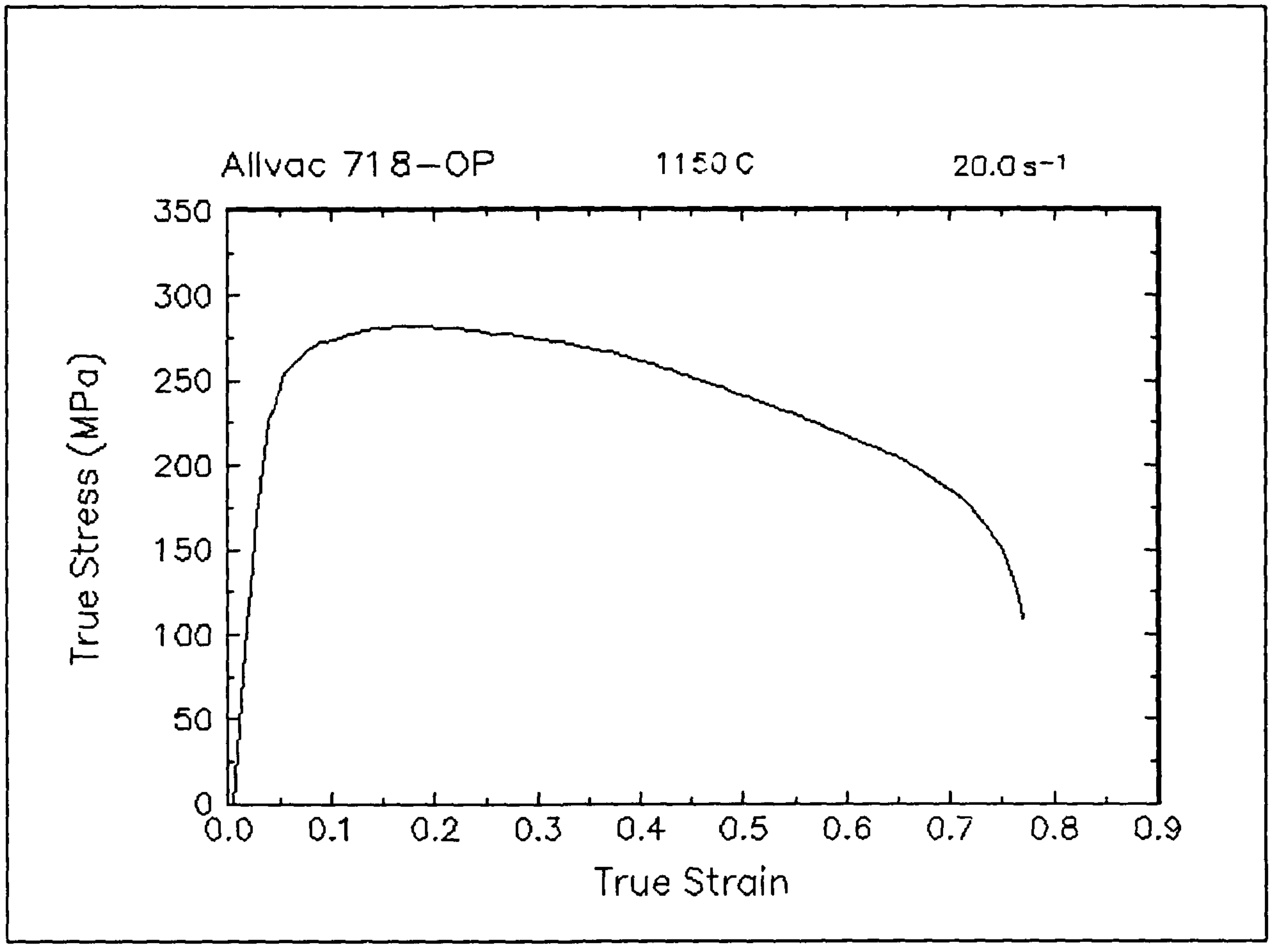

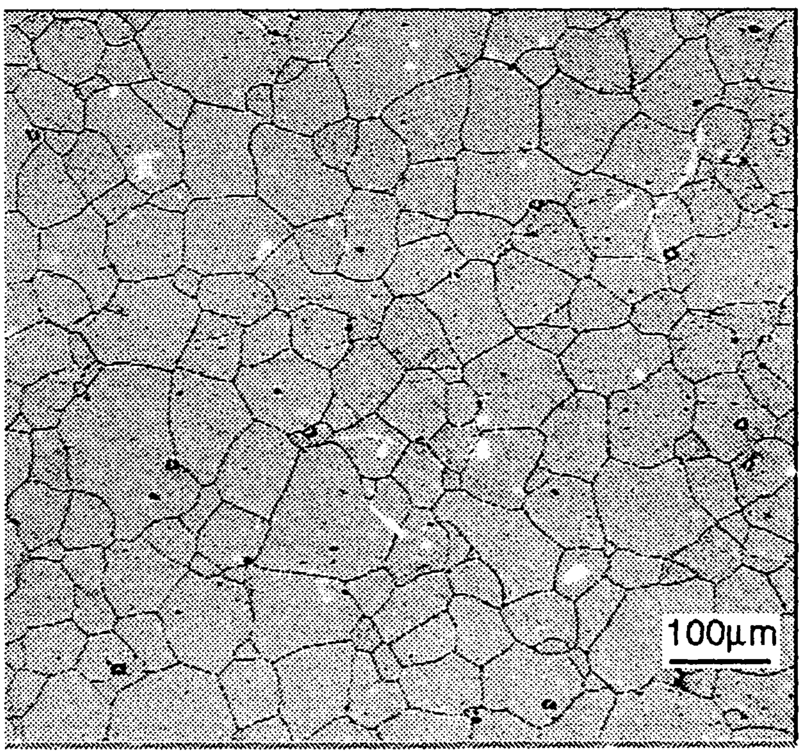

Figure 57. True stress-true strain curve and an optical micrograph from the center of the compressed sample cut through the compression axis, 1150 C and 20 s^{-1}.

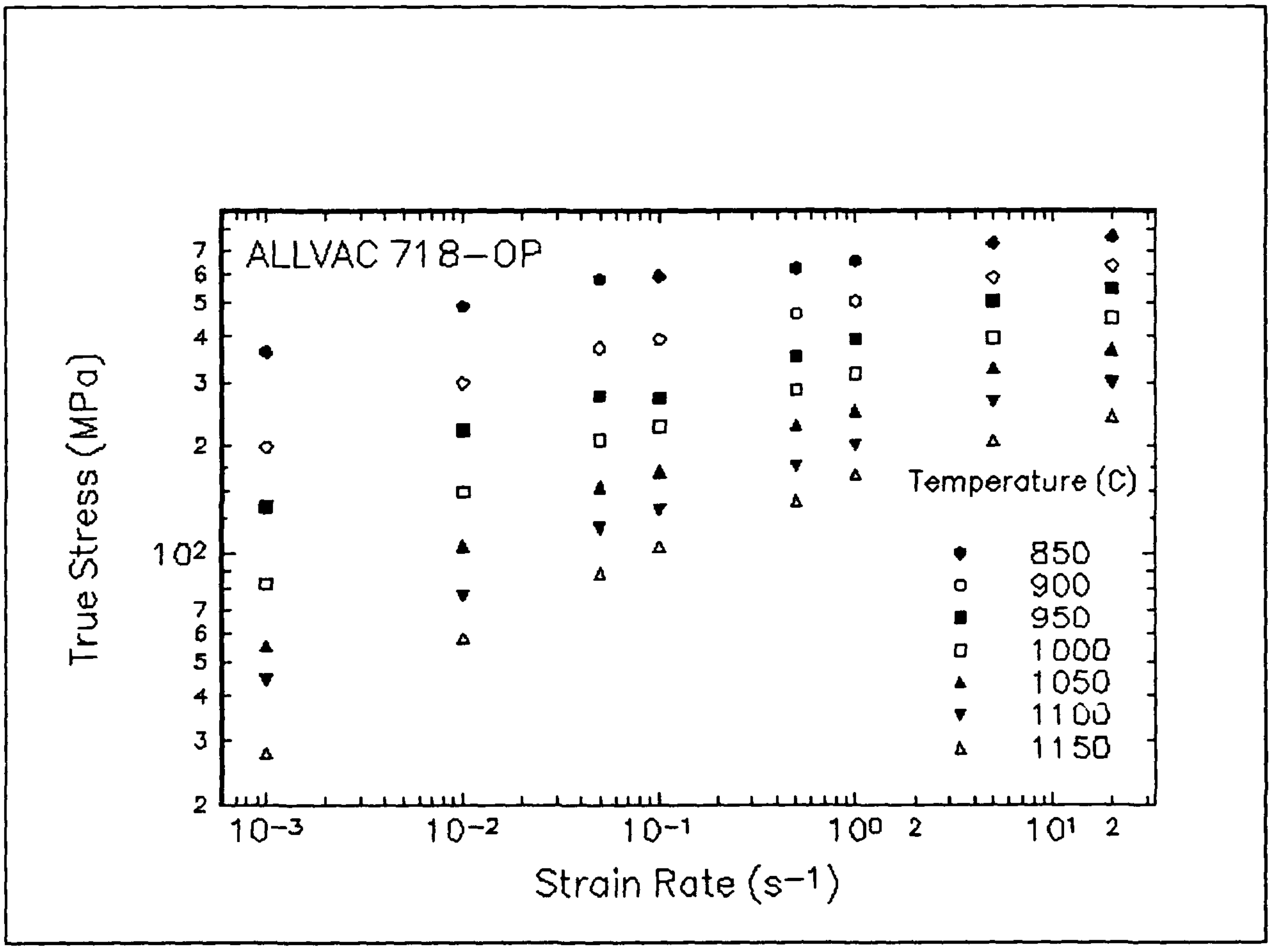

Figure 58. Effect of strain rate on stress in log-log scale at a true strain of 0.5 for Allvac 718-OP.

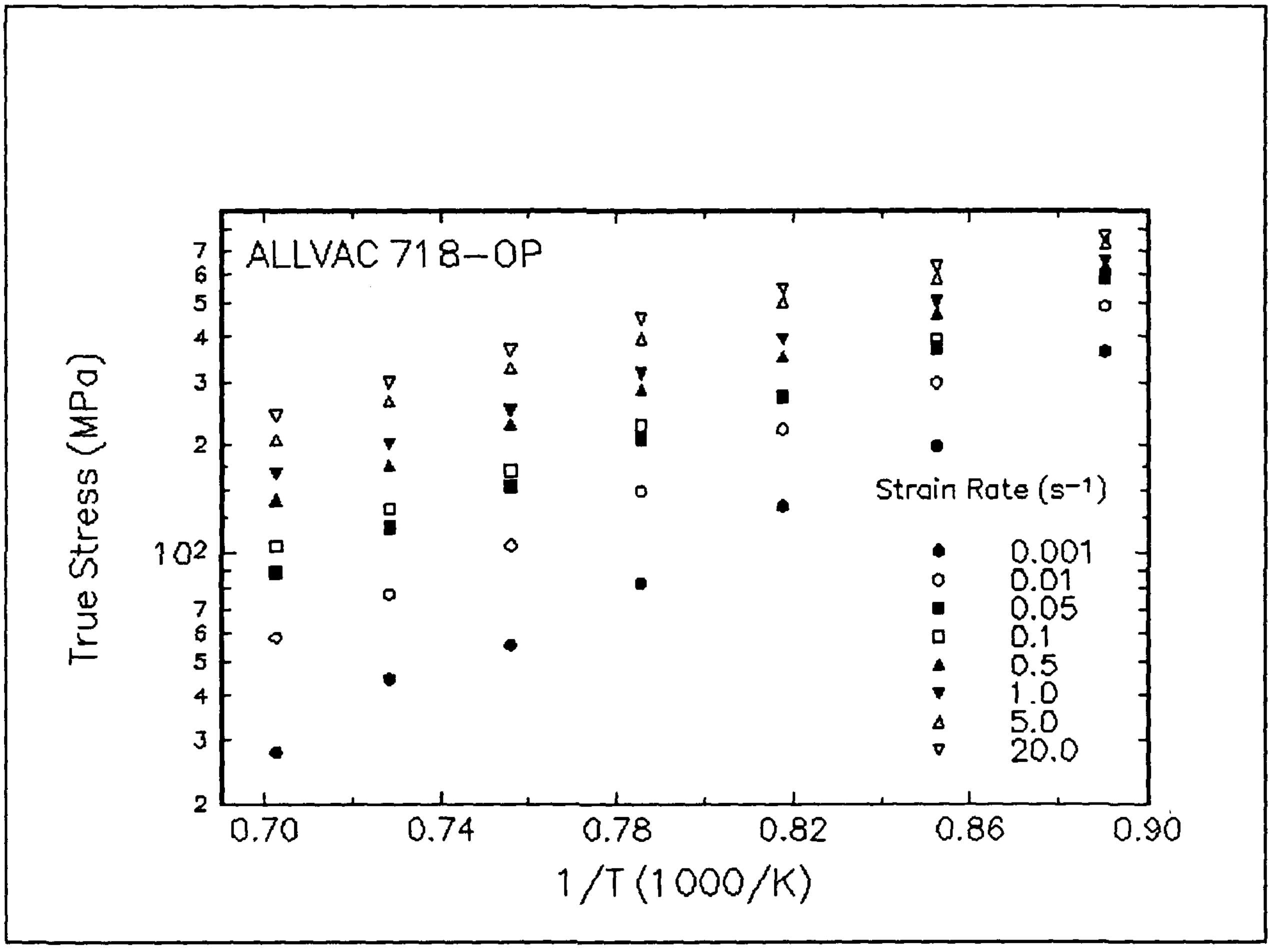

Figure 59. Effect of temperature on stress at a true strain of 0.5 for Allvac 718-OP.

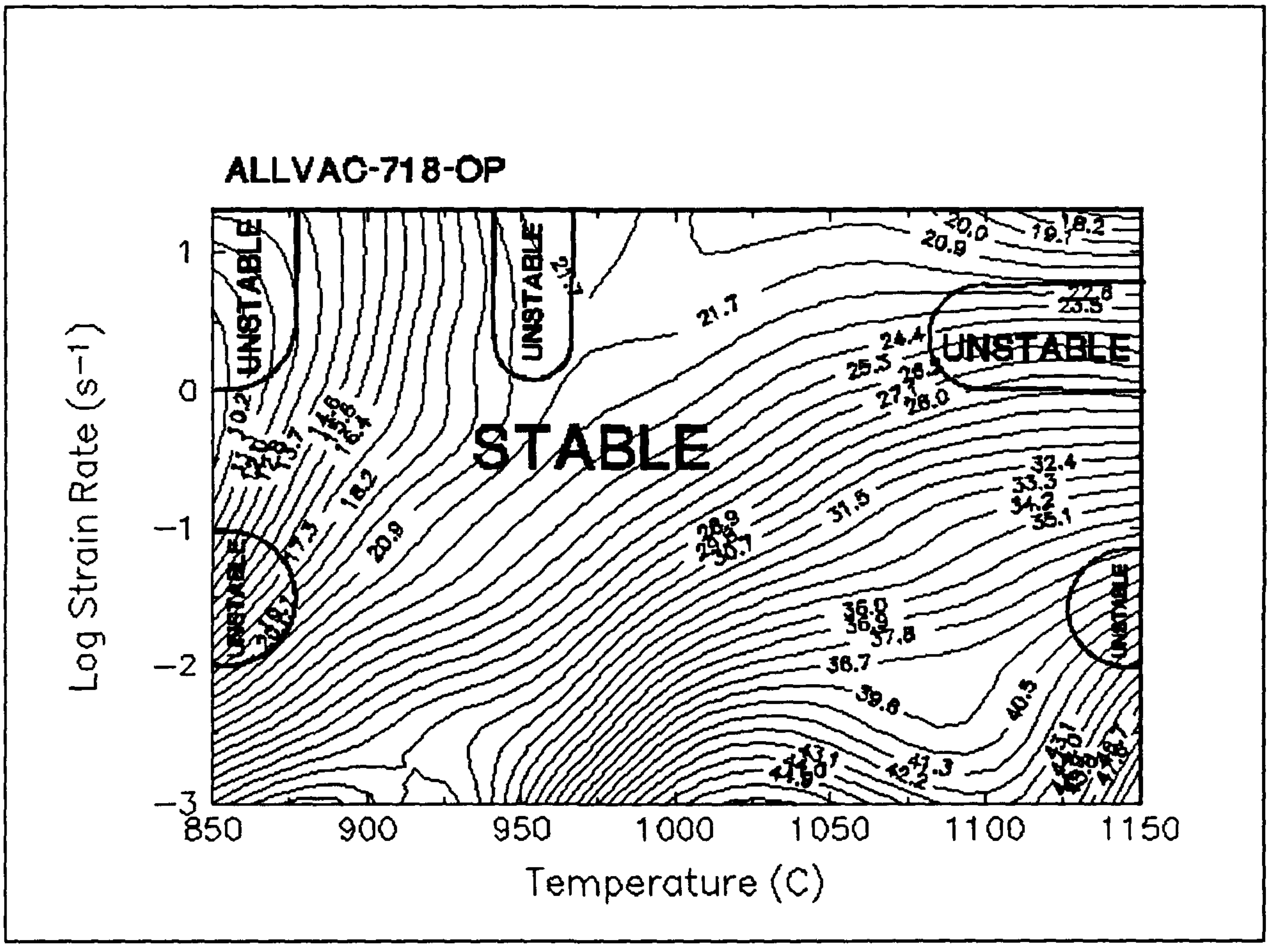

Figure 60. Processing map of Allvac 718-OP at a true strain of 0.5.

Summary

Compression tests have been performed on Allvac 718-OP over a wide range of temperatures and strain rates. The experimental conditions used in this work are representative of those used in metal forming practices. From the stress-strain curves, the flow behavior was characterized and a processing map indicating the optimum processing condition was generated. This condition is 1025 C and 10^{-3} s^{-1}.

The deformed microstructures were characterized from the quenched specimens by optical microscopy and are presented for selective testing conditions under the stress-strain curves..

Implementation of Data Provided by the Atlas of Formability

The Atlas of Formability program provides ample data on flow behavior of various important engineering materials in the temperature and strain rate regime commonly used in metalworking processes. The data are valuable in design and problem solving in metalworking processes of advanced materials. Microstructural changes with temperature and strain rates are also provided in the Bulletin, which helps the design engineer to select processing parameters leading to the desired microstructure.

The data can also be used to construct processing map using dynamic material modeling approach to determine stable and unstable regions in terms of temperature and strain rate. The temperature and strain rate combination at the highest efficiency in the stable region provides the optimum processing condition. This has been demonstrated in this Bulletin. In some metalworking processes such as forging, strain rate varies within the workpiece. An analysis of the process with finite element method (FEM) can ensure that the strain rates at the processing temperature in the whole workpiece fall into the stable regions in the processing map. Furthermore, FEM analysis with the data from the Atlas of Formability can be coupled with fracture criteria to predict defect formation in metalworking processes.

Using the data provided by the Atlas of Formability, design of metalworking processes, dynamic material modeling, FEM analysis of metalworking processes, and defect prediction are common practice in *Concurrent Technologies Corporation*. Needs in solving problems related to metalworking processes can be directed to Dr. Prabir K. Chaudhury, Manager of Forming Department, by calling (814) 269-2594.